UNIVERSITY OF CALIFORNIA,
IRVINE

Thermal Conductivity and Kapitza Resistance of Ceramic Composites

DISSERTATION

submitted in partial satisfaction of the requirements
for the degree of

DOCTOR OF PHILOSOPHY

in Chemical and Biochemical Engineering

by

Austin William Travis

Dissertation Committee:
Professor Martha L. Mecartney, Chair
Assistant Professor Mo Li
Andrew T. Nelson, Ph.D.

2018

DEDICATION

To my parents and sister,
For their endless support

To my wonderful EEM,
For always believing in me

TABLE OF CONTENTS

List of Figures……vii

List of Tables……x

Acknowledgments……..xi

Curriculum Vitae……..….xii

Abstract of the Dissertation……...xvi

Chapter 1: Introduction……1

1.1 Introduction to Ceramics and Thermal Conductivity……..1

1.2 Thermal Conductivity and Kapitza Resistance of Ceramic Composites for Inert Matrix Nuclear Fuel ……...……...5

1.3 3ω Method for Measuring Thermal Conductivity of Bulk Ceramic Samples……..5

1.4 Thermal Conductivity Modeling of UN/U_3Si_2 Composite Fuel Forms…….6

1.5 Continuum Scale Modeling of Hyperstoichiometric Uranium Dioxide……...7

Chapter 2: Experimental Methods……8

2.1 Ceramic Processing Techniques…….8

2.1.1 Electron Beam Evaporation…….9

2.2 Characterization Techniques……10

2.2.1 X-Ray Diffraction……..10

2.2.2 Scanning Electron Microscopy……..10

2.3 Computational Models…….11

2.3.1 Object-Oriented Finite Element Analysis (OOF2)……11

2.3.2 Multiphysics Object-Oriented Simulation Environment (MOOSE)……...11

Chapter 3: Thermal Conductivity and Kapitza Resistance of Three-Phase Ceramic Composites Through Experimental Measurements and Computations Models……....12

3.1 Abstract……12

3.2 Introduction……..13

3.3 Experimental Procedures……..16

3.4 Results and Discussion……18

3.4.1 Degradation of thermal conductivity as a function of grain size……...18

3.4.2 Comparison of experimental and modeled thermal conductivity……...21

3.4.3 Kapitza resistance of three-phase composites……25

3.4.4 Calculated thermal conductivity as a function of grain size at 25 °C and 800 °C……29

3.4.5 Investigation into Kapitza Resistance of Two-and Three Phase Composites by Extrapolation of Thermal Resistivity……32

3.5 Conclusions……..37

3.6 Acknowledgements……..38

Chapter 4: Comparison of Laser Flash Analysis and 3 Omega Method Thermal Measurement Techniques on 8YSZ and Al_2O_3 – $MgAl_2O_4$ – 8YSZ Composite……...39

4.1 Abstract……39

4.2 Introduction……..40

4.3 Experimental Procedures……..42

4.3.1 Sample Preparation and Characterization……..42

4.3.2. 3ω Method……42

4.3.3 Laser Flash Analysis……..44

4.4 Results and Discussion……45

4.4.1 Calculating thermal conductivity using laser flash analysis……...45

4.4.2 Calculating thermal conductivity using 3ω method……...49

4.4.3 Comparison of 3ω method and laser flash analysis for single-phase 8YSZ and $MgAl_2O_4$……....55

4.4.4 Comparison of 3ω method and laser flash analysis for three-phase composite……..57

4.4.5 Advantages and Disadvantages of 3ω Method and Laser Flash Analysis…..58

4.5 Conclusions……..60

4.6 Acknowledgements……..61

Chapter 5: Thermal Modeling of UN/U-Si Composite Fuel Forms……62

5.1 Abstract……62

5.2 Introduction……..63

5.3 Finite Element Analysis Modeling Procedures……65

5.3.1 OOF2 Microstructural Meshing……65

5.3.2 MOOSE Thermal Conductivity Modeling……67

5.4 Results and Discussion……68

5.4.1 Comparison of Experimental and Modeled Results……..68

5.4.2 Influence of Unknown U-N-Si Phase on Effective Thermal Conductivity…73

5.4.3 Estimation of Irradiation Effects on Composite Thermal Conductivity…….78

5.5 Conclusions……..80

5.6 Acknowledgements……..81

Chapter 6: Continuum Scale Modeling of Hyperstoichiometric UO_{2+x}……82

6.1 Abstract……82

6.2 Introduction……..83

6.3 Experimental Procedures……..86

6.3.1 Phase Field Modeling in MOOSE……..86

6.3.2 Implementing anisotropy in phase field models……89

6.3.3 Thermal Conductivity Simulations on Evolved Microstructures in MOOSE……91

6.4 Results and Discussion……93

6.4.1 Thermal Conductivity Results of UO_{2+x} as a Function of Hyperstoichiometry and Temperature……93

6.5 Conclusions……..96

6.6 Acknowledgements……..97

Chapter 7: Conclusions and Future Work……..……98

7.1 Summary and Conclusions……...98

7.2 Future Work……...101

References……102

Appendices……...113

Appendix A: Example MOOSE Code……113

Appendix B: Example OOF2 Code……117

LIST OF FIGURES

Figure 1.1 A cross-sectional image of a UO_2 fuel pellet showing cracking caused by high thermal stresses which limit the lifetime of the pellet in pile [3]……4

Figure 3.1 Thermal conductivity as a function of temperature for UO_2 compared to the components of the multiphase composite: Al_2O_3, $MgAl_2O_4$, and 8YSZ……14

Figure 3.2 Backscattered SEM of equal volume three-phase composite showing only 8YSZ (white), alumina (grey), and spinel (black) grains after sintering, polishing and thermal etching. (a) Large grain size, (b) Fine grain size……..19

Figure 3.3 Experimental measurements using laser flash analysis shows reduction of thermal conductivity as a function of grain size from 25°C to 800°C.……20

Figure 3.4 OOF2 meshing process and heat flux map. (a) Backscattered SEM image showing the three distinct phases. (b) Colors assigned to each phase for easier thresholding while applying material properties within OOF2. (c) Meshing with triangular elements with a high density of nodes at interfaces between phases. (d) A temperature gradient of 10 K is applied across the microstructure, so a heat flux map can be visualized within OOF2……21

Figure 3.5 Thermal conductivity as a function of temperature for the 1.2 μm grain size Al_2O_3-$MgAl_2O_4$-8YSZ composite measured experimentally modeled using finite element modeling via MOOSE, Geometric Mean, Bruggeman, and Rule of Mixtures calculations. ……23

Figure 3.6 Thermal conductivity as a function of temperature for the 450 nm grain size Al_2O_3-$MgAl_2O_4$-8YSZ composite measured experimentally modeled using finite element modeling via MOOSE, Geometric Mean, Bruggeman, and Rule of Mixtures calculations. ……24

Figure 3.7 Kapitza resistance as a function of temperature comparing three-phase material with two different grain sizes with prior results on 8YSZ using the temperature dependent method [28, 33]……...26

Figure 3.8 Predicted thermal conductivity incorporating Kapitza resistance in OOF2/MOOSE as a function of grain size for the three-phase Al_2O_3-$MgAl_2O_4$-8YSZ. This calculation assumes the microstructure will be self-similar at all grain sizes……30

Figure 3.9 Thermal resistivity as a function of temperature for the three-phase composite with large-grain size extrapolated to T = 0 K……33

Figure 3.10 OOF2 simulations of the thermal conductivity as a function of temperature for three binary-phase composites showing the composites containing Al_2O_3 have higher thermal conductivities……35

Figure 3.11 Inverse thermal conductivity as a function of temperature plots used to calculate the Kapitza resistance for the three binary-phase compositions……...36

Figure 4.1 Thermal diffusivity as a function of temperature for 8YSZ and an Al_2O_3 – $MgAl_2O_4$ – 8YSZ composite with two distinct grain sizes as measured by laser flash analysis.....47

Figure 4.2 Grain size independent specific heat capacity as a function of temperature for equal phase fraction Al_2O_3 – $MgAl_2O_4$ – 8YSZ as measured by differential scanning calorimetry……..47

Figure 4.3 Density change as a function of temperature for Al_2O_3 – $MgAl_2O_4$ – 8YSZ composites with 1.2 μm and 500 nm grain sizes as measured by dilatometry……48

Figure 4.4 TCR calibration results for voltage as a function of current for various temperatures for 8YSZ……..50

Figure 4.5 TCR calibration output for determining the resistance of the heater line at 0 °C and α, the coefficient of thermal contact resistance for 8YSZ……...51

Figure 4.6 Example 3ω data set showing the in-phase and out-of-phase regimes. The fit trendline indicates the ideal regions for calculating thermal conductivity [91]……..52

Figure 4.7 In-phase 3ω voltage as a function of ln(f). A highly linear regime was selected and the slope was calculated as a parameter for the thermal conductivity calculation…….53

Figure 4.8 Comparison of thermal conductivity values for laser flash analysis and 3ω method for 8YSZ……..55

Figure 4.9 Comparison of thermal conductivity values for laser flash analysis and 3ω method for $MgAl_2O_4$ [67]…….56

Figure 4.10 Comparison of thermal conductivity values for 1.2 μm and 500 nm grain size Al_2O_3 – $MgAl_2O_4$ – 8YSZ composites measured by laser flash analysis and 3ω method……57

Figure 5.1 The thermal conductivity as a function of temperature for the constituent phases of the UN/U_3Si_2 composite compared to the thermal conductivity values for UO_2 [48, 49, 64]……..64

Figure 5.2 (a) An optical micrograph showing the two distinct phases of the composite. The light phase indicating the U_3Si_2 phase, the dark grey phase showing the UN phase, and the darkest region indicating porosity or grain pull out. (b) The colorized microstructure shows the composition without the porosity allowing for a simpler mesh to applied. (c) The mesh showing the presence of many nodes at the interfaces between phases to capture the change in thermal conductivity. (d) A 10 K temperature gradient was applied from top to bottom on the mesh. The thermal map shows regions of high thermal flux (indicated by the lighter color) allowing for a visualization of pathways of higher thermal transport……....66

Figure 5.3 Micrographs showing the variations in compositions between samples (a) 10 vol% U_3Si_2 (b) 20 vol% U_3Si_2 (c) 30 vol% U_3Si_2 (d) 40 vol% U_3Si_2……..69

Figure 5.4 (a) Discrepancies between experimental values and modeled values for the 10 vol% U_3Si_2 specimens. (b) Discrepancies between experimental values and modeled values for the 20 vol% U_3Si_2 specimens. (c) Discrepancies between experimental values and modeled values for the 300 vol% U_3Si_2 specimens. (d) Discrepancies between experimental values and modeled values for the 40 vol% U_3Si_2 specimens……70

Figure 5.5 XRD pattern for the various compositions showing the peak positions of the UN and U_3Si_2 phases……...72

Figure 5.6 Comparison of experimental measurements and modeled data for the 40 vol% U_3Si_2 composites……..73

Figure 5.7 The thermal conductivity of the unknown U-Si-N phase was calculated using the rule of mixtures and is shown in orange squares. ……75

Figure 5.8 An overview of the OOF2 meshing process for the now three-phase composite. (a) The SEM micrograph shows a third phase. (b) This third phase is easier to see once the micrograph has been colorized and meshed. Again, there is a high density of nodes at the boundaries between phases. (c) The thermal map shows the regions of high thermal transport through the microstructure……76

Figure 5.9 Modeled thermal conductivity results have high agreement with the experimental results (within the error of experimental measurements). Except the 10 vol % samples which for an unknown reason has much higher deviation than the 20, 30, and 40 vol% samples……77

Figure 5.10 Modeled thermal conductivity values showing the potential degradation of the thermal conductivity in the silicide phase under irradiation……79

Figure 6.1 Uranium – oxygen phase field diagram showing the various oxides that can form as a function of temperature and oxygen stoichiometry [120]……...84

Figure 6.2 Thermal conductivity as a function of increasing oxygen hyperstoichiometry from Watanabe *et al.* [87]……84

Figure 6.3 SEM micrograph showing UO_2 (dark) and U_4O_9 light [121]……90

Fig 6.4 Phase field model for a UO_2 – U_4O_9 microstructure evolved at 400 K and an initial concentration of oxygen of 0.20. (b) Meshed microstructures showing refinement of the quadrature points on the mesh with a high concentration of points capturing the interface between the two phases……93

Figure 6.5 Thermal conductivity as a function of temperature and oxygen concentration……94

Figure 6.6 Simulated and experimental Thermal conductivity as a function of temperature in a binary phase UO_{2+x} and U_4O_9 composition when x = 0.143……95

LIST OF TABLES

Table 1.1 : A survey of the Kapitza resistances of various grain boundaries and interfaces for metals and ceramics reported in literature……3

Table 3.1 Kapitza resistance values from the temperature dependent method for the three-phase composite and single-phase YSZ……...27

Table 3.2 Kapitza resistance values calculated with the y-intercepts from Fig. 3.9 using the Smith method for three-phase composite materials……..34

Table 3.3 Kapitza resistance values calculated with the y-intercepts from Fig. 3.11 using the Smith method for two-phase composite materials……36

Table 5.1 Percentages of phases as determined by EDS for the various compositions fabricated in this study……....74

Table 6.1 Free energy functions for the dual phase field. These functions are derived from the uranium-oxygen phase diagram and are expressed as oxygen concentration as a function of temperature……88

Table 6.2 Parameters for solving the thermal conductivity of UO_{2+x}……..91

ACKNOWLEDGMENTS

First, thank you to my advisor, Professor Martha Mecartney, for her guidance, encouragement, and for sharing her passion of science with me. Special thanks to Dr. Andrew Nelson for the years of mentorship and for the opportunity to research at Los Alamos National Laboratory.

Also, special thanks to my committee members Professor Mo Li, Professor Micke Nilsson, and Professor Yoonjin Won for the insightful feedback and suggestions throughout the course of my research. Special thanks to Dr. David Andersson for instilling in me the science and art of good modeling.

Thank you to my current and past colleagues in the Mecartney group: Kenta Ohtaki, David Kok, Yingjie Yang, Somanth Mandal, Komal Syed, Zonghan Yang, Michael Lu, Tom Kaufman, Jie Shen, and Dr. Jesse Angle.

Thank you to my research collaborators: Dr. Josh White of Los Alamos National Laboratory and Dr. Chris Dames of UC Berkeley for showing me the importance of scientific collaboration.

Finally, thank you to the funding provided throughout the course of my dissertation by the Nuclear Regulatory Commission, Department of Energy, and National Science Foundation.

CURRICULUM VITAE

Austin William Travis

Irvine, CA 92697
travisa@uci.edu / 802.338.0525

EDUCATION

University of California, Irvine
Ph.D. Chemical Engineering 2018

M.S. Chemical Engineering 2014

Syracuse University
B.S. Chemical Engineering 2013

AWARDS AND FELLOWSHIPS

UCI ChEMS Nuclear Fellowship funded by the NRC 2015-2018
ACerS Nuclear and Environmental Technology Division
Travel Grant for MS&T16 2016
UCI ChEMS Department Fellowship 2013-2014
Syracuse University Academic Scholarship 2009-2013
Syracuse University Deans Honor List 2009-2013

RESEARCH EXPERIENCE

University of California, Irvine, Irvine, CA 2014 – 2018
Graduate Student Researcher
Research Advisor: Professor Martha L. Mecartney

- Modeled the temperature dependence of binary and ternary oxide composites with application toward inert matrix nuclear fuel using OOF2 (Object Oriented Finite Element Analysis v2)
- Synthesized binary and ternary oxide composites for experimental determination of the temperature dependent thermal conductivity.
- Characterized composite materials using x-ray diffraction (XRD), scanning electron microscopy (SEM), and Energy-dispersive X-ray Spectroscopy (EDS).

Los Alamos National Laboratory 2015 – 2016
Graduate Student Researcher
Mentors: Dr. Andrew Nelson and Dr. David Andersson

- Modeled the temperature dependent thermal conductivity of binary phase systems of hyperstoichiometric uranium dioxide using MOOSE (Multiphysics Object Oriented Simulation Environment).

- Utilized phase field modeling to develop a binary phase field of UO_2 and U_4O_9 at equilibrium for various concentrations of oxygen within the microstructure.

Irvine Materials, Irvine, Irvine, CA 2014 - 2018
Lab Assistant
Mentor: Dr. Qiyin Lin
- Performed training sessions and provided assistance to users on two X-Ray Diffractometers in a user facility on University of California, Irvine Campus
- Analyzed samples using a combination of Small Angle X-Ray Scattering and Rietveld Refinement for phase identification of samples from contracts.

Syracuse University, Syracuse, NY 2012 – 2013
Undergraduate Student Researcher
Advisor: Professor Radhakrishna "Suresh" Sureshkumar
- Synthesized colloidal nanogels and characterized their optical properties under shear stress at various flow rates
- Included a summer position as part of NSF's REU program

PEER-REVIEWED PUBLICATIONS

4) **Travis, A.W.**, Nelson, A.T., Mecartney, M.L., "Thermal conductivity and Kapitza resistance of an alumina, spinel, and yttria-stabilized zirconia composite," *Journal of the American Ceramics Society* (In review).

3) White, J.T., **Travis, A.W.**, Dunwoody, J., Nelson, A.T., "Fabrication and thermophysical property characterization of UN/U_3Si_2 composite fuel forms", *Journal of Nuclear Materials* **495** (2017) 463-474.

2) **Travis, A.W.,** Nelson A.T., and Mecartney M.L., "Computational Studies of Thermal Conductivity of Multiphase Ceramics for Inert Matrix Fuel", *Transactions of the American Nuclear Society*, **115** (2016) 110-111.

1) **Travis, A.W.**, Andersson D.A., and Nelson A.T., "Continuum Scale Modeling of the Thermal Conductivity of Hyperstoichiometric UO_2," *Transactions of the American Nuclear Society NSFM 2016*, **114** (2016) 1185-1186.

PRESENTATIONS

Podium Presentations

Travis, A.W., White, J.T., and Nelson, A.T., "Modeling the Thermal Conductivity of UN/U_3Si_2 Composites" International Conference on Advanced Ceramics and Composites, Daytona Beach, Florida, January 2018.

Travis A.W. and Mecartney, M.L., "Thermal Conductivity Measurements of Ceramic Composites with the 3 Omega Technique" Conference on Electronic and Advanced Materials, Orlando, Florida, January 2018.

Travis, A.W., Nelson, A.T., and Mecartney, M.L., "Computational Studies of Thermal Conductivity of Multiphase Ceramics for Inert Matrix Fuel" American Nuclear Society National Meeting, Las Vegas, Nevada, November 2016.

Travis, A.W., Karandikar, K., Nelson, A.T., Graeve, O., and Mecartney, M.L., "Thermal Conductivity of Multiphase Ceramics for an Inert Matrix Fuel", Materials Science and Technology 2016, Salt Lake City, Utah, October 2016.

Travis, A.W., Phillips, K.J., Nelson, A.T., and Mecartney, M.L., "Computational Simulations of Thermal Conductivity of Multiphase Ceramics for an Inert Matrix Nuclear Fuel", Materials Science and Technology 2015, Columbus, Ohio, October 2015.

Poster Presentations

Travis, A.W., Andersson, D.A., and Nelson, A.T., "Continuum Scale Modeling of the Thermal Conductivity of Hyperstoichiometric UO_2", American Nuclear Society (ANS) National Meeting, New Orleans, Louisiana, June 2016.

Travis A.W., Angle J.P., Morgan, P.E.D., and Mecartney, M.L., "XRD Analysis of Novel Magnetoplumbite Structures", Denver X-Ray Conference (DXC), Big Sky, Montana, July 2014.

PROFESSIONAL AFFILIATIONS

American Nuclear Society (ANS)
American Ceramic Society (ACerS)
American Chemical Society (ACS)
Materials Research Society (MRS)
American Institute of Chemical Engineers (AIChE)
ASM International

ACADEMIC SERVICE AND OUTREACH

Representative, Environmental Health and Safety – Safety on Site, 2014 – 2018
President, Materials Research Society at UCI, 2014 – 2015
President, AIChE at Syracuse University, 2012 – 2013
Tutor, Chemical Engineering Department at Syracuse University, 2012 - 2013

TEACHING AND MENTORING EXPERIENCE

University of California, Irvine, Irvine, CA
Teaching Assistant, Department of Chemical Engineering and Materials Science

- Chemical Engineering Laboratory II — Winter 2015, Winter 2016

Graduate Student Mentor — 2014 – 2018

- 2 graduate student researchers (2 Ph.D., 2 M.S., and 2 B.S.)

Breakthrough Program — Summer 2014

- Mentored two high school students

INDUSTRY EXPERIENCE

Green Mountain Coffee Roasters, Waterbury, VT — June 2010 – August 2010
Process Engineer Intern

TECHNICAL SKILLS

Characterization:	Optical Microscopy, Scanning electron microscopy (SEM), Focused ion beam (FIB) X-ray diffraction (XRD), High temperature X-ray diffraction (HTXRD), Grazing incidence X-ray diffraction (GIXRD), Scanning transmission electron microscopy (STEM), Energy-dispersive X-ray Spectroscopy (EDS).
Computers:	Windows OS, Max OS, Microsoft Office, Adobe Creative Studios, MATLAB, ImageJ, CrystalMaker, OOF2, MOOSE.
Ceramic Processing:	Ball milling, Attrition milling, Cold isostatic Press (CIP), High temperature furnaces, Mass flow systems, Slow speed saws, SEM sample preparation, Ion beam Sputtering, So-gel process, Rotary Evaporation.

ABSTRACT OF THE DISSERTATION

Thermal Conductivity and Kapitza Resistance of Ceramic Composites

By

Austin William Travis

Doctor of Philosophy in Chemical and Biochemical Engineering

University of California, Irvine, 2018

Professor Martha L. Mecartney, Chair

Advanced ceramic composites are actively investigated for use in various fields of the technology sector including nuclear fuel. Conventional uranium dioxide (UO_2) nuclear fuel has low thermal conductivity resulting in a limited lifetime within a nuclear reactor. Novel ceramic composites with higher thermal conductivity can be engineered for use as nuclear fuel to increase efficiency and accident tolerance. In this study, the role of microstructure and composition on thermal conductivity of several ceramic composites will be investigated. First, the thermal conductivity of three-phase ceramic composites consisting of aluminum oxide (Al_2O_3), magnesium aluminum spinel ($MgAl_2O_4$), and cubic 8 mol% yttria stabilized zirconia (8YSZ) is measured experimentally and modeled via OOF2 and MOOSE finite element analyses for two distinct grain sizes. A difference between experimental and calculated results is observed at low temperatures and is attributed to the Kapitza resistance of interfaces and grain boundaries within the material. It is hypothesized that the presence of heterointerfaces, or grain boundaries between different materials, increases the overall Kapitza resistance of composite materials. Next, the same three-phase composite system is shown to validate the 3ω method for thermal conductivity measurements of bulk ceramic samples at low temperatures when compared to values obtained via

laser flash analysis. Then, several uranium containing composites are explored. The effect of microstructure on thermal conductivity is investigated for unique accident tolerant fuel forms containing various compositions of UN and U_3Si_2. Finally, phase field modeling of hyperstoichiometric UO_{2+x} simulates the influence of oxygen nonstoichiometry on the degradation of thermal conductivity in UO_{2+x} and U_4O_9 binary-phase composites.

Chapter 1: Introduction

1.1 Introduction to Ceramics and Thermal Conductivity

Ceramics are broadly defined as "a crystalline solid with predominantly ionic and covalent bonding" [1]. Ceramic composites, the focus of this dissertation, are materials with multiple ceramic phases composing the bulk material. Ceramics have unique properties including high melting points, high fracture toughness, and low electrical conductivity [1]. By combining multiple ceramic phases into one bulk material, some of the drawbacks of using traditional single-phase materials can be bypassed as well as tailoring a material to fit a specific application. Ceramic composites are widely used in a number of applications ranging from nuclear fuel forms [2-7], thermal barrier coatings [8-10], energy production [11-17], machining [18,19], biomaterials [20-23], aerospace applications [24,25], and various other applications.

The ceramic composites under investigation in this study were chosen for their unique thermal properties, specifically, the thermal conductivity. The thermal conductivity of a material can be tailored by the selection of certain phases to engineer a material to behave with high thermal conductivity or low thermal conductivity [8]. Thermal conductivity is the material property that governs how well thermal energy, or heat, is transferred through a material. Fourier's Law defines the relationship between heat flux, thermal conductivity, and a temperature gradient by the following equation:

$$\vec{q} = -k\Delta T \tag{1-1}$$

The magnitude of the heat flux is governed by the thermal gradient and the thermal conductivity of the material [26].

Thermal conductivity can be calculated by the product of the thermal diffusivity, density, and specific heat capacity by the following equation:

$$k(T) = \alpha(T) * \rho(T) * c_p(T) \quad (1\text{-}2)$$

Ceramics are generally insulating materials and follow the trend of decreasing thermal conductivity with increasing temperature above the Debye temperature. The Debye temperature is defined as the temperature of a crystal's highest mode of vibration, or the highest temperature that can be achieved by a single normal vibration. To understand this concept, the theory of phonon transport must be introduced. There are two modes by which thermal energy can be transferred through a solid crystalline material, by phonons or by electrons. Phonons are lattice vibrations that propagate through a crystal structure from regions of high to low temperature. Phonons are the driving force of thermal transport in most ceramic materials [27,28]. Heat transfer via the movement of free electrons is seen in metals. The primary focus of this research will be on phonon transport in ceramics.

An interesting phenomenon in thermal transport is the temperature mismatch seen across an interface between two materials, phases, or grains [28]. First seen by Kapitza in 1941 during studies on heat flowing from a solid to liquid helium [29], the aptly named Kapitza resistance, or interfacial thermal resistance, is the resistance to thermal transport at an interface. Since its discovery, the Kapitza resistance has been observed in ceramic materials with nanocrystalline grain sizes [28, 29:35]. This resistance can lower the effective thermal conductivity of the bulk by scattering phonons at the interface between grains in a material.

Table 1.1 collects the Kapitza resistance values for single-phase and composite materials that the author could find within the literature. The key takeaway in terms of ceramics for this information is the dirge of oxide materials on the list. Currently, values for cubic and tetragonal yttria-stabilized zirconia, UO_2, and $SrTiO_3$ are the only Kapitza resistance values reported for oxide materials [30, 33, 36, 37]. While the phenomenon of Kapitza resistance has been known

since the initial research by Kapitza in 1941, the physics and phenomenon has only recently been applied to ceramic materials in the last few decades. Continuing to calculate and ultimately develop a method to directly measure the Kapitza resistance is of paramount importance for future materials for high and low temperature applications.

Table 1.1 A survey of the Kapitza resistances of various grain boundaries and interfaces for metals and ceramics reported in literature. There is a lack of information related to Kapitza resistances in oxide materials. Also, the magnitude of the Kapitza resistance varies by many orders of magnitude depending on the phases on either side of the boundary.

Grain Boundary / Interface	**Kapitza Resistance (m^2K/W)**
3 mol% Y2O3 (3YTZP) [33]	4.5×10^{-9}
8 mol% Y2O3 (8YSZ) [39]	4.5×10^{-9}
UO_2 [37]	1×10^{-8}
$SrTiO_3$ [30]	$3.41 - 4.98 \times 10^{-9}$
SiC [39]	4.88×10^{-10}
SiC/Al [36]	6.85×10^{-9}
Diamond/ZnS [36]	6×10^{-8}
Diamond/Cordierite [40]	7×10^{-8}
Si	1.3×10^{-9}
$Si_{0.8}Ge_{0.2}$	1.0×10^{-7}
Bi_2Te_3 / Sb_2Te_3	1.4×10^{-5}
$FeSb_2$ [41]	2.17×10^{-7}

Nuclear energy is a globally growing source of clean energy. Currently, 435 reactors are operating in 31 different countries and about 60 plants are currently being constructed in 13 countries. Recent reports show nuclear reactors generated about 13% of the world's electricity. Conventional nuclear fuel, UO_2, suffers from low thermal conductivity and a high central temperature which can result in melting or cracking [2,3]. A severe case of cracking within a nuclear fuel pellet is shown in Figure 1.1.

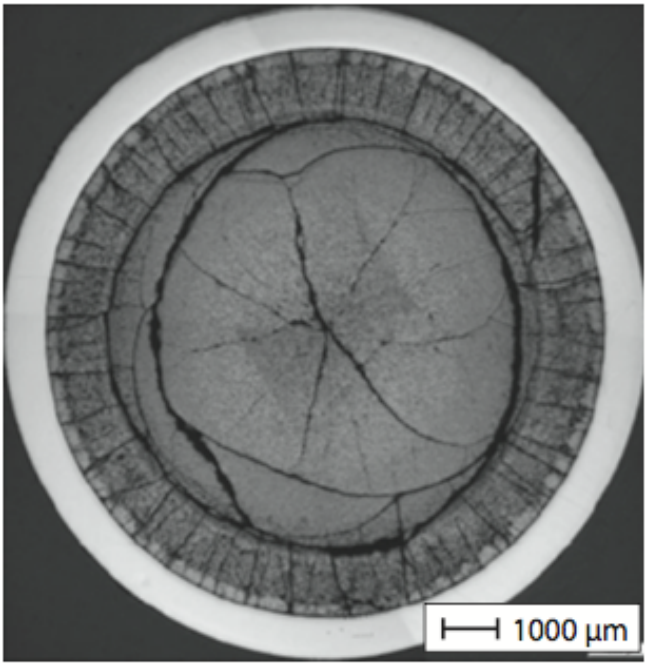

Figure 1.1 A cross-sectional image of a UO_2 fuel pellet showing cracking caused by high thermal stresses which limit the lifetime of the pellet in pile [3].

1.2 Thermal Conductivity and Kapitza Resistance of Ceramic Composites for Inert Matrix Nuclear Fuel

The thermal conductivity of a three-phase ceramic containing aluminum oxide (Al_2O_3), magnesium aluminum spinel ($MgAl_2O_4$), and 8 mol% yttria stabilized zirconia is experimentally measured and modeled. The thermal conductivity determined via finite element modeling is higher than the experimentally measured samples at temperatures below 673 K. This difference is attributed to the Kapitza resistance. While methods have been developed for calculating the Kapitza resistance of single phase and binary phase materials; these methods have not been extended for use with composites containing three or more elements. Two methods have been used to calculate the Kapitza resistance for this three-phase composite, a linear extraction method and a temperature dependent method. Both methods show higher Kapitza resistance values compared to literature values for the single phases present in agreement. It is hypothesized that the heterointerfaces in composites have higher Kapitza resistances than grain boundaries in single phase materials due to the mismatch between different phases with different densities and crystal structures. Estimates on the thermal conductivity as a function of grain size are also calculated.

1.3 3ω Method for Measuring Thermal Conductivity of Bulk Ceramic Samples

Laser flash analysis has widespread use in the ceramics community for measuring thermal conductivity of bulk materials [42]. Here, results from laser flash analysis and 3ω (omega) are compared for bulk single-phase materials and composites. Results show good agreement between the two methods at temperatures between 25 and 150 °C thus validating the 3ω Method for bulk ceramic materials with varying thermal properties and microstructures. The 3ω methodology presented within allows for low temperature measurements to be made with high accuracy for either thermoelectrics [43:45] or as a screening tool for high temperature measurements with laser flash analysis.

1.4 Thermal Conductivity Modeling of UN/U_3Si_2 Composite Fuel Form

There is also research underway to use new fuel forms as drop-in replacements for UO_2 [4]. Prompted by the recent accident at Fukushima in Japan, accident tolerant fuels are being investigated for their enhanced intrinsic safety and higher thermal thresholds allowing for more efficient electricity production and longer fuel lifetimes [46,47]. One proposed accident tolerant fuel is uranium nitride (UN). UN has been investigated due to its high uranium density (when compared to UO_2), high melt point, high thermal conductivity, and favorable irradiation behavior [48]. However, a significant drawback to UN is the potential onset of oxidation once exposed to air, steam, or water which could occur in an accident scenario within a light water reactor (LWR). To mitigate this potential hazard, a secondary oxidation resistant phase is introduced to encapsulate the UN phase. While an inert phase could be incorporated while still maintaining higher uranium density than UO_2, uranium silicide (U_3Si_2) has been proposed [49]. U_3Si_2 has the same benefits of UN, but has the additional benefit of greater resistance to oxidation and subsequent pulverization at temperatures where UN pulverizes catastrophically [50,51]. Composites containing UN and U_3Si_2 have been investigated. The thermal conductivity of composites containing various phase fractions of UN and U_3Si_2 have been modeled and compared to experimental data. The thermal conductivity of all composites is higher when compared against UO_2. Irradiated thermal conductivities are also estimated using finite element modeling. An unknown third phase is also present in the composites. The thermal conductivity of the unknown third phase can be estimated from a combination of experimental data, modeled results, and a simple rule of mixtures calculation. While thermal results are promising, in-pile testing would need to be conducted before UN/U-Si composite fuel types could be implemented in current generation light water reactors.

1.4 Continuum Scale Modeling of Hyperstoichiometric Uranium Dioxide

Currently, nuclear power plants rely on the fission of uranium dioxide (UO_2) fuel pellets to generate electricity in both pressurized water reactors and boiling water reactors. While UO_2 has been used for decades in commercial nuclear reactors, there are still areas of active research underway in order to optimize efficiency and safety [52]. In an accident scenario when UO_2 is exposed to air, steam, or water it oxidizes and incorporates additional oxygen into its fluorite crystal structure [53,54]. This can form a binary phase system of hyperstoichiometric UO_{2+x} and the defect structure U_4O_9 depending on the temperature. Binary composites are difficult to study due to their ever-changing nature in the presence of oxygen so continuum scale phase field modeling has been employed to study the oxygen diffusion and resulting effective thermal conductivity. Inputs from experimental data and molecular dynamics simulations are used to investigate the effect of oxygen concentration on thermal conductivity. Phase field modeling is employed within the MOOSE framework to model various microstructures at different temperatures and oxygen concentrations [55]. Models show that increasing oxygen concentration leads to decreasing thermal conductivity in agreement with previous experimental studies.

Chapter 2: Experimental Methods

2.1 Ceramic Processing Techniques

Traditional ceramic processing techniques were utilized for several of the composites under investigation [56]. The materials selected for each composite were chosen based on their unique thermal properties. More detail about the inert matrix fuel and composite fuel forms will be discussed in the relevant chapters. Initial single-phase ceramic powders were massed according to the ratios prescribed by the desired phase composition. Powders were attrition milled in a Union Process mill with yttria-stabilized zirconia milling media and isopropyl alcohol as a milling dispersant to form a slurry. The initial mass of the powders was kept constant at 40 grams per batch. Typically, milling was performed overnight for approximately 12 hours. The resulting slurry was then dried using a rotary evaporator and the dried powder was ground using an agate mortar and pestle. Next, powders were sieved to a standard particle size of < 80 μm.

Then, the fine powders were pressed into green bodies by a cold isostatic press (CIP). Within the CIP, powders were held at 55kpsi for 5 minutes in a cylindrical mold. The post-CIP geometric density was measured for comparison to post-sintering density. The green bodies were then sintered in air to high density using a high temperature furnace (CM Furnaces). Green bodies were packed in alumina crucibles with a sintering bed of the material being sintered (i.e. Al_2O_3 sintering bed for Al_2O_3 samples, Al_2O_3 – $MgAl_2O_4$ – 8YSZ composite sintering bed for Al_2O_3 – $MgAl_2O_4$ – 8YSZ composite samples, etc.). Specific sintering profiles will be outlined in the corresponding sections to achieve different microstructures. Samples were sintered to a final density of 90 – 99% theoretical density measured via geometric and Archimedes density measurements. Dense samples were then cut into specific geometries using a diamond bladed saw

and polished for characterization. More detailed processing relevant to the research will be discussed in the following chapters.

2.1.1 Electron Beam Evaporation

Electron beam evaporation is a thin-film technique used for depositing patterned heater lines and pads for eventual 3ω measurement. In electron beam evaporation, a beam of electrons causes atoms in a target material to sublimate into the gaseous phase. These gaseous atoms then precipitate onto a sample within line of sight [57]. A shadow mask was used to obtain the specific pattern for depositing a 100 nm layer of gold on top of a 10 nm layer of chromium for an adhesion layer. The bulk ceramic sample with patterned heater line is then ready for subsequent 3ω measurements.

2.2 Characterization techniques

2.2.1 X-Ray Diffraction

X-ray diffraction (XRD) was used for determining the phases present within a material based on the principles of Bragg's Law [56]. Every crystalline material has a unique diffraction pattern that can solved via XRD. Every crystal has long range order of repeating unit cells of atoms. The d-spacing, which is the distance between repeating layers of crystals, can be measured by changing the diffraction angle of the incident x-rays. XRD is used to determine the phase purity of ceramic composites while also provided an estimate of the phase fraction found in each composite.

2.2.2 Scanning Electron Microscopy

Scanning electron microscopy (SEM) was used to characterize the microstructures of ceramics under an electron beam. SEM is used rather than optical microscopy for materials with features that are smaller than the wavelength of light. The incident electron beam interacts with the ceramic material and either the secondary electrons (electrons ejected from the electron shell around atoms) or backscatter electrons (incident electrons that rebound back out of the material) are detected and quantified [56]. SEM was used to generate micrographs of composites for grain size analysis and computational modeling. Energy dispersive X-ray spectroscopy (EDS) is a feature of the SEM that quantifiably measures the amount of each atom within the sample. This technique is useful for phase fraction analysis and for determining the location of atoms within the grains of the microstructure.

2.2.3 Thermal Conductivity Measurements

2.3 Computational Models

Finite element modeling is a technique for assigning material properties to specific points on a mesh and then calculating bulk material properties. Two finite element frameworks are considered OOF2 (object-oriented finite element analysis v2) and MOOSE (Multiphysics object-oriented simulation environment). Both frameworks will be outlined below with deeper discussion in subsequent chapters.

2.3.1 Object-oriented Finite Element Analysis (OOF2)

OOF2 is freeware distributed through NIST (National Institute of Standards and Technology) and has been used to study thermal, electrical, and mechanical properties of materials. The strength of OOF2 originates in its robust meshing of real microstructures obtained through SEM. By utilizing real microstructures, actual grain shapes and compositions can be accounted for as opposed to using theoretical hexagonal microstructures where every grain is the same shape, size, etc.

2.3.2 Multiphysics Object-Oriented Simulation Environment (MOOSE)

MOOSE is distributed though INL (Idaho National Laboratory) and is a flexible finite element framework with many additional physics modules including thermal transport, phase field modeling, and mechanical properties among other things. While many of the MOOSE applications are for nuclear applications, the physics and modeling could be used by any materials engineer. Specifically, the phase field and thermal modules were used for various models and calculations. Again, a more in-depth discussion of the various models will be introduced in later chapters.

Chapter 3: Thermal Conductivity and Kapitza Resistance of Three-Phase Ceramic Composites Through Experimental Measurements and Computations Models

3.1 Abstract

The thermal conductivity of three-phase ceramic composites consisting of aluminum oxide (Al_2O_3), magnesium aluminum spinel ($MgAl_2O_4$), and cubic 8 mol% yttria stabilized zirconia (8YSZ) is measured experimentally using laser flash analysis, dilatometry, and differential scanning calorimetry over a range of temperatures from 25 °C to 800 °C and modeled via OOF2 and MOOSE finite element analyses for two distinct grain sizes. The difference between experimental and calculated results is attributed to the Kapitza resistance of interfaces and grain boundaries within the material. A procedure for calculating the Kapitza resistance of a three-phase ceramic is outlined. The average Kapitza resistance of this three-phase composite is calculated to be 8.4×10^{-9} - 9.8×10^{-9} m^2K/W, depending on the grain size and thermal history. The results show that the grain boundaries between different phases (heterointerfaces) may have higher Kapitza resistance than grain boundaries in single-phase materials. One consequence of this is that Kapitza resistance in multi-phase materials will exhibit degradation of the thermal conductivity at larger grain sizes than typically observed in single-phase polycrystalline materials.

3.2 Introduction

Multiphase ceramics have been proposed to enhance the thermal conductivity of ceramics used in various materials applications, including nuclear fuels. Nuclear energy contributes to approximately 20% of the country's electricity and is an efficient way to provide baseline power. One of the drawbacks of conventional uranium dioxide (UO_2) nuclear fuel is the low thermal conductivity both at room temperatures and elevated temperatures found in reactor environments [3,4]. Over the lifetime of a fuel pellet, the low thermal conductivity can lead to macroscopic changes in the mechanical properties of the fuel, chiefly cracking which could result in the failure of the fuel and cladding material [58].

Inert matrix nuclear fuels have been proposed as a novel approach that incorporates fissile phases into an inert or non-fissile host matrix to enhance thermal conductivity, improve radiation damage tolerance, and/or achieve superior mechanical properties compared to single phase UO_2 [59, 60, 61]. Previous research has successfully demonstrated a two-phase concept with minority nuclear fuel surrogate particles dispersed through an inert matrix [2]. Recently, MgO has been proposed as an inert matrix due to its high thermal conductivity with $A_2B_2O_7$ pyrochlores such as actinide zirconates used to accommodate actinides [62]. Rock-like oxide fuels (ROX) are also candidates and contain spinel and fluorite oxide inert matrix phases and show increased thermal conductivity compared to UO_2 [63].

Thermal conductivity as a function of temperature, $\kappa(T)$, is the material property that governs thermal transport and can be calculated as follows,

$$\kappa(T) = \alpha(T)C_p(T)\rho(T) \tag{3-1}$$

where $\alpha(T)$ is the thermal diffusivity, $C_p(T)$ is the specific heat capacity, and $\rho(T)$ is the density. There are two means by which heat transfers through a crystalline material. Phonons (lattice

vibrations) are the primary mechanism for heat transfer for the ceramic oxides evaluated here. Collective lattice vibrations result in the propagation of phonons through the lattice until they are scattered at point defects, grain boundaries, or other lattice imperfections [28]. Electrons are also thermal carriers, but provide a minor contribution in electrical insulators. Phonon driven thermal conductivity shows decreased thermal conductivity at reactor temperatures when compared to room temperature and follows the trend $\lambda(T) = 1/T$ above the Debye temperature. This change in thermal conductivity as a function of temperature for the materials used in this study is shown in Fig. 1 and compared to compared to UO_2.

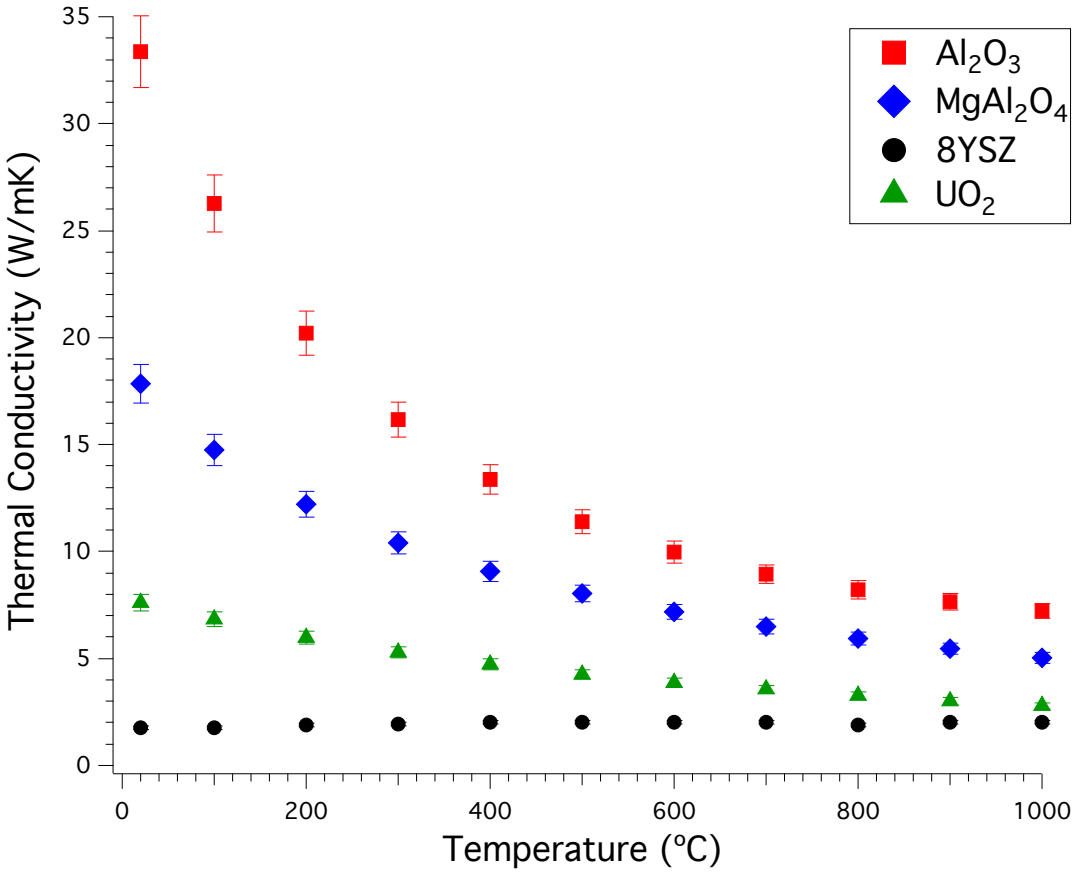

Figure 3.1 Thermal conductivity as a function of temperature for UO_2 compared to the components of the multiphase composite: Al_2O_3, $MgAl_2O_4$, and 8YSZ [64-67].

This research fabricates and evaluates fine and large grain three-phase composites containing aluminum oxide (Al_2O_3), magnesium aluminum spinel ($MgAl_2O_4$), and 8 mol% yttria-stabilized zirconia (8YSZ) as a potential inert matrix fuel. 8YSZ is used as a surrogate for UO_2 in the composite since 8YSZ and UO_2 are structurally similar and are thermodynamically comparable in terms of general stability. While the thermal conductivity of YSZ is lower than unirradiated UO_2 as plotted in Fig.1, it better matches that of irradiated UO_2 [64, 65, 68]. YSZ was selected over CeO_2, another proposed surrogate, which is susceptible to reductions and reactions [68]. Both Al_2O_3 and $MgAl_2O_4$ introduced as components in the inert matrix as they have increased thermal conductivities and are therefore expected to significantly increase the thermal conductivity of the surrogate fuel [66, 67].

It is known that a temperature discontinuity exits at the interfaces between two phases or two crystallographic orientations [28], termed Kapitza resistance after Kapitza who first studied the interfacial thermal resistance using the interface between helium and a metal substrate in 1941 [29]. This Kapitza or interfacial resistance can influence the thermal conductivity of multiphase inert matrix nuclear fuel. While Kapitza resistance has been calculated from experiments for single phase materials including Y-TZP and $SrTiO_3$ [28, 30], as well as several other types of two-phase composites, the Kapitza resistance of a three-phase composite has not been experimentally determined. We seek to determine the Kapitza resistance of grain boundary interfaces as a function of temperature for three-phase Al_2O_3, $MgAl_2O_4$, and 8YSZ composites with a range of grain sizes utilizing a combination of experimental measurements and finite element analysis (FEA) modeling using the MOOSE framework.

3.2 Experimental Procedures

Initially, powders of alumina (TM-DAR, Taimicron, Japan), spinel (S30CR, Baikowski, Charlotte, NC), and cubic 8YSZ (TZ-8YS, Tosoh USA, Grove City, OH) are attrition milled (HD-01, Union Process, Akron, OH) in equal volume fractions for 8 hours. The resulting slurry is dried overnight at 100 °C and subsequently ground with a mortar and pestle. The powder is then pressed into cylindrical samples using a cold isostatic press for 5 minutes at 55 kpsi. The green bodies had a theoretical density of 55%. Two different sintering profiles are utilized to produce different grain sizes while maintaining a similar composition. For a large grained material, the green bodies are sintered in air at 1550 °C for 10 hours to 97% density, measured via the Archimedes displacement method. For a finer grained material, the green bodies are sintered using a two-step sintering route. First, the samples are brought to 1450 °C with no dwell time before being lowered to 1325 °C for 5 hours to achieve 96% density, again measured via the Archimedes displacement method. Sintered bodies are used to prepare samples for thermal measurements and characterization. Scanning electron microscopy (SEM) (FEI Magellan XHR SEM, Hillsboro, OR) is used to characterize the microstructure.

Experiments to determine thermal diffusivity ($\alpha(T)$), specific heat capacity ($c_p(T)$), and density ($\rho(T)$) are conducted to calculate the thermal conductivity via Equation 1. The values are individually measured as a function of temperature from 25 °C to 800 °C in 100 °C intervals starting at 100 °C. Thermal diffusivity was measured with a laser flash apparatus (Netzsch 457 LFA, Germany). Heat capacity as a function of temperature was measured with differential scanning calorimetry (Netzsch 404 F1 DSC, Germany). Density was measured with a horizontal push-rod dilatometer (Netzsch 402 CD, Germany). Further details of these methods are provided in a previous publication [6].

A combination of object-oriented finite element analysis version 2 (OOF2) and multiphysics object-oriented simulation environment (MOOSE) were employed to model the thermal conductivity of the composite [55, 69, 70]. Both OOF2 and MOOSE are open source, finite element software distributed by National Institute of Standards and Technology (NIST) and Idaho National Laboratory (INL), respectively. SEM micrographs of the different microstructures were meshed in OOF2 following a process of successive refining of triangular elements to a high level of homogeneity. The homogeneity index is defined as the ratio of elements that completely exist in one phase. Meshes in this study were refined to above 99% homogeneity. In a study by Teague *et al*. [71], it was determined that refining to a minimum of 97% homogeneity resulted in less than 5% deviation of thermal conductivity values. This approach has been previously implemented to model the thermal conductivity of ceramic composite [6, 7, 72].

The resulting meshes were imported into MOOSE to model the effective thermal conductivity as a function of temperature from 25 °C to 800 °C in the same increments as the laser flash analysis experiments. OOF2 also offers this capability, however, MOOSE has additional physics modules for analysis of different materials properties on the same microstructure meshes. One side of the mesh was held at a constant temperature and the parallel side was assigned a flux value to simulate a 10 °C temperature gradient across the microstructure. The two other parallel sides were kept adiabatic. Each unique phase was assigned a thermal conductivity value taken from literature and the effective thermal conductivity of the composite was determined. Five micrographs were used for the model before deviations in thermal conductivity between micrographs were unchanging. The effective thermal conductivity was calculated with the following relationship:

$$\kappa_{eff}(T) = -\frac{q}{\frac{T_r - T_l}{l}} \tag{3-2}$$

where $\kappa_{eff}(T)$ is the effective thermal conductivity, q is the heat flux, T_r and T_l are the temperatures on the right and left boundaries, and l is the side length of microstructure [70].

A limitation of finite element analysis is the inability to capture solid state physics at the atomistic level which therefore limits the MOOSE model to length scale regimes where continuum behavior dominates. In most ceramic materials, atomistic treatment of certain phenomena such as phonon mean free path are necessary around 100 nm [27, 73]. Therefore, it would be necessary to use another model such as molecular dynamics for materials with grain sizes below 100 nm.

3.4 Results and Discussion

3.4.1 Degradation of thermal conductivity as a function of grain size

A typical microstructure of the three-phase composite is shown in Figure 3.2, with backscattered electron imaging showing clearly the different phases dependent on Z-contrast. Prior XRD studies confirmed that no new phases form in this materials with a nominal grain size of 1.2 μm [74]. The corresponding volume phase fractions from backscattered SEM images is calculated to be 0.29 $MgAl_2O_4$, 0.35 Al_2O_3, and 0.35 8YSZ. The grain size of the two-step sintered samples is 450 nm with corresponding volume phase fractions equal to 0.30 $MgAl_2O_4$, 0.36 Al_2O_3, and 0.33 8YSZ. The differences in composition between the phase fractions all fall within one standard deviation when calculating the phase fractions. The phase fractions are quantified by counting the pixels of each phase of the microstructure within the OOF2 framework.

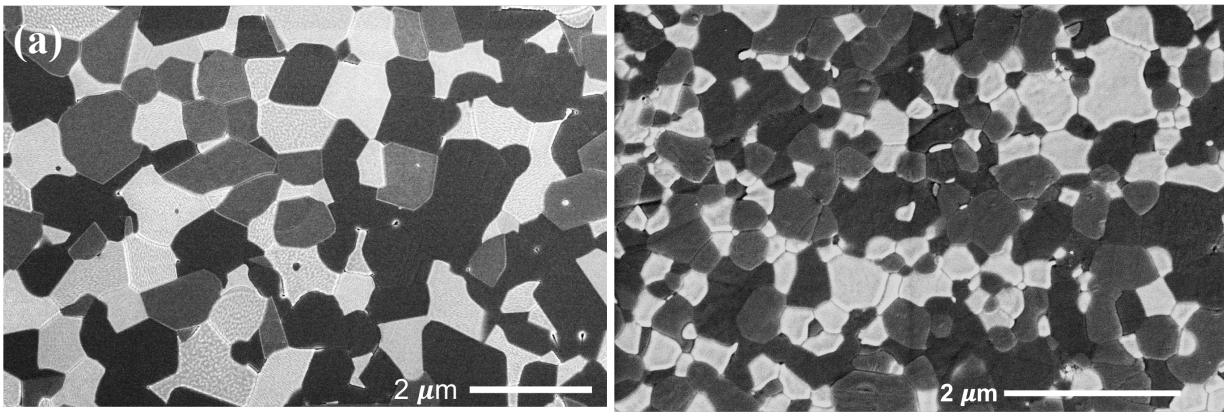

Figure 3.2 Backscattered SEM of equal volume three-phase composite showing only 8YSZ (white), alumina (grey), and spinel (black) grains after sintering, polishing and thermal etching. (a) Large grain size, (b) Fine grain size.

In Figure 3, the experimentally determined thermal conductivity as a function of temperature for the large and fine grain materials is compared. There is an approximate 10% reduction in thermal conductivity at room temperature from the 1.2 μm grain size to the 450 nm grain size. The standard error assumed for calculation of thermal conductivity when calculated using the product of thermal diffusivity, specific heat capacity, and density is 5% [75], and as such this reduction is statistically significant. The specific heat capacity is assumed to be independent of grain size and the density values of each composite are measured via dilatometry. The magnitude of degradation diminishes at higher temperatures, from 10% reduction at room temperature to less than 2% at 800°C. This degradation is attributed to the Kapitza resistance associated with the reduction in grain size since compositionally the samples are identical within 2%. To understand this thermal conductivity degradation in greater detail, the Kapitza resistance for each composite is calculated in Chapter 3.4.3. Several models to calculate the thermal conductivity of the composite will be investigated for their accuracy to the experimental measurements.

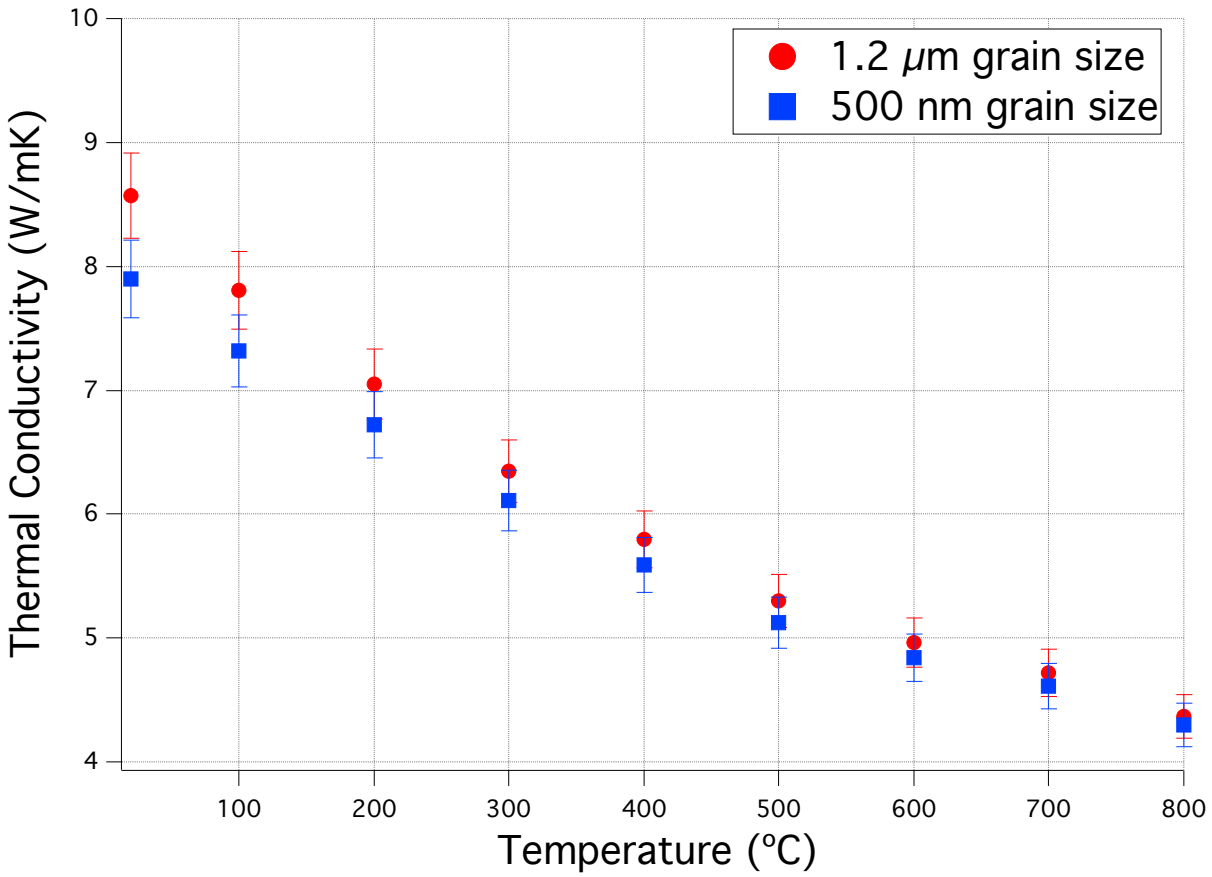

Figure 3.3 Experimental measurements using laser flash analysis shows reduction of thermal conductivity as a function of grain size from 25°C to 800°C. The magnitude of degradation is highest at low temperature.

3.4.2 Comparison of experimental and modeled thermal conductivity

A representation of the OOF2 meshing process and resulting heat flux map is shown in Figure 4. In the heat flux map, brighter regions represent areas of high heat flux and the dark regions are areas of low heat flux, corresponding to phases with high thermal conductivity (alumina, spinel) and low thermal conductivity (8YSZ) respectively.

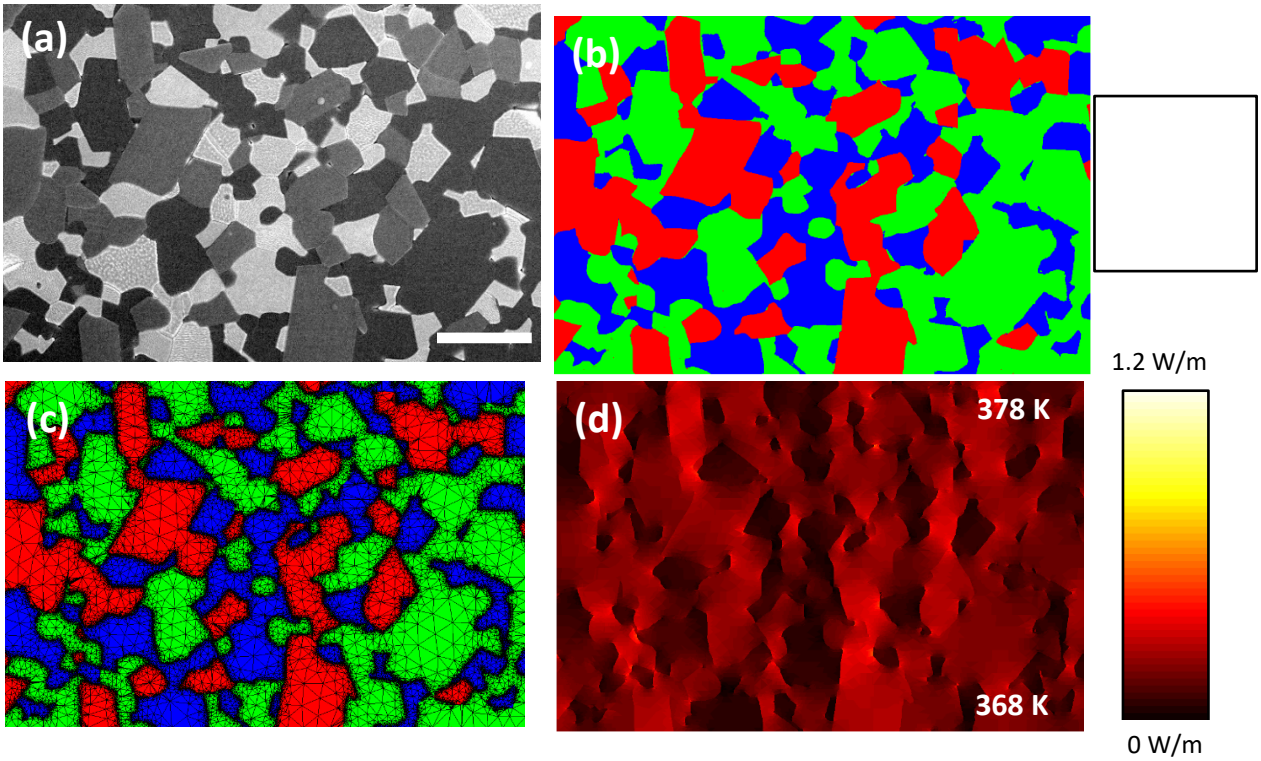

Figure 3.4 OOF2 meshing process and heat flux map. (a) Backscattered SEM image showing the three distinct phases. (b) Colors assigned to each phase for easier thresholding while applying material properties within OOF2. (c) Meshing with triangular elements with a high density of nodes at interfaces between phases. (d) A temperature gradient of 10 K is applied across the microstructure, so a heat flux map can be visualized within OOF2.

The experimentally measured values in Figure 3 are compared in Figure 5 to various models used predict the thermal conductivity including MOOSE, Bruggeman model [76], Rule of Mixtures, and the Geometric Mean. The models use thermal conductivity values from Figure 3.1, as well as the phase fractions calculated from microstructure analysis. The three-phase Bruggeman model is given below in Equation 3-3,

$$V_1\left(\frac{k_1-k_{eff}}{k_1+2k_{eff}}\right)+V_2\left(\frac{k_2-k_{eff}}{k_2+2k_{eff}}\right)+V_3\left(\frac{k_3-k_{eff}}{k_3+2k_{eff}}\right)=0 \quad (3\text{-}3)$$

where V_i is the phase fraction of the i^{th} phase, k_i is the thermal conductivity of the i^{th} phase, and k_{eff} is the effective thermal conductivity of a random dispersion of three phases. The commonly used upper bound of the Rule of Mixtures is given by Equation 3-4,

$$k_{eff}=V_1k_1\times V_2k_2\times V_3k_3 \quad (3\text{-}4)$$

where the variables have the same values as the Bruggeman model in Equation 3-3. Finally, Equation 3-5 represents the Geometric Mean.

$$k_{eff}={k_1}^{V_1}{k_2}^{V_2}{k_3}^{V_3} \quad (3\text{-}5)$$

Across the entire temperature range, the Rule of Mixtures calculations yields significantly higher thermal conductivity values compared to the experimental results, which has been observed in previous studies for ceramic composites [72]. The Bruggeman model is also higher than experimental results. The Geometric Mean and MOOSE models offer the closest approximations, but still with some significant deviations from the experimental data.

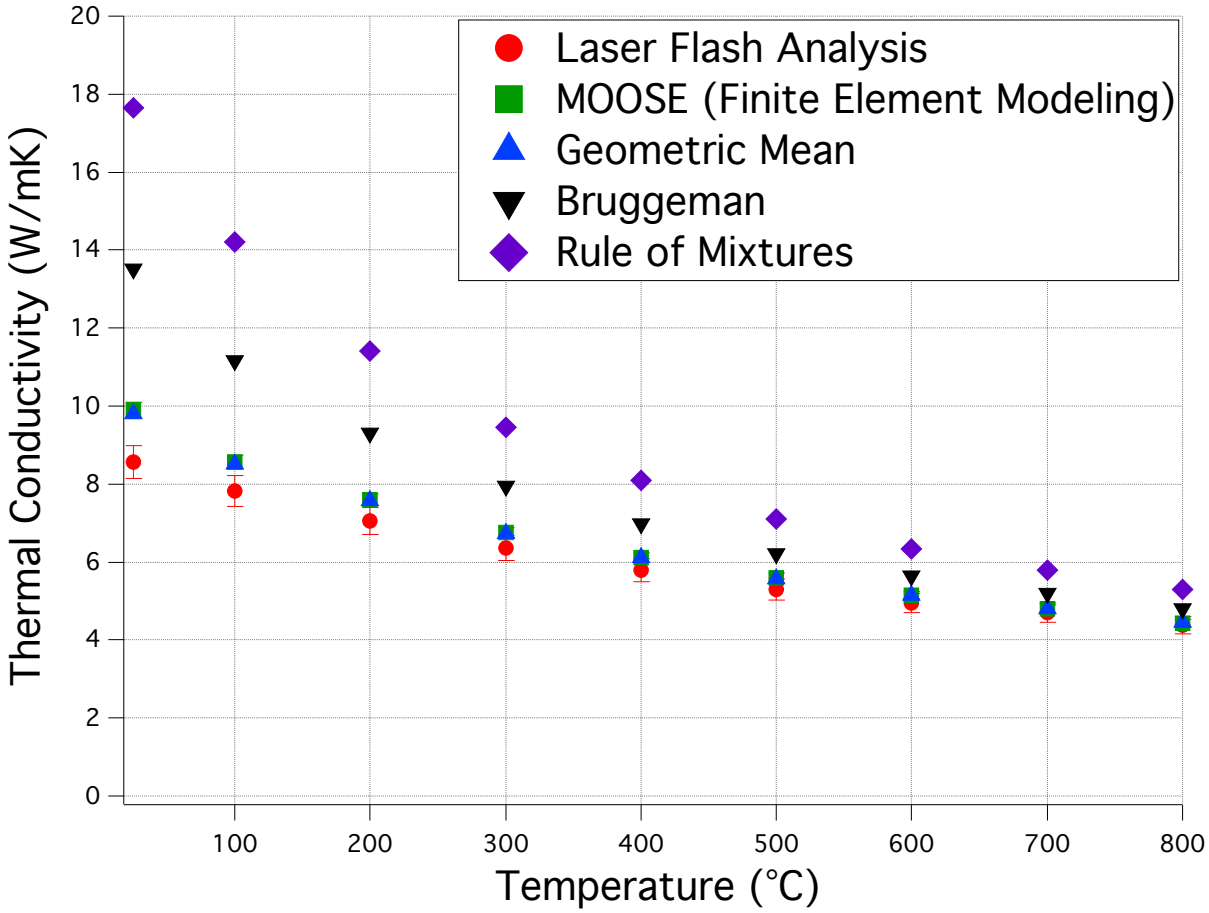

Figure 3.5 Thermal conductivity as a function of temperature for the 1.2 μm grain size Al_2O_3-$MgAl_2O_4$-8YSZ composite measured experimentally modeled using finite element modeling via MOOSE, Geometric Mean, Bruggeman, and Rule of Mixtures calculations.

To study this phenomenon further, an alumina, spinel, and 8YSZ composite with a smaller grain size is also evaluated using the same models. The models do not consider grain size; differences between samples with the different grain sizes are attributed to minor variations in the measured phase fractions. Here, the finer grain material has a measured nominal grain size of 450 nm with similar composition. The results in Figure 3.6 follow the same trend when compared to the experimental measurements as in Figure 3.5; the Rule of Mixtures calculation has the highest deviation when compared to the experimental results, followed by the Bruggeman model, with the

MOOSE and Geometric Mean results having the closest agreement but still significant deviations. In all models, the deviation in thermal conductivity values is much higher at room temperature than at higher temperatures such as 800 °C. Angle *et al.* [6] found a similar trend when evaluating thermal conductivity of three- and four-phase ceramic composites using OOF2 and proposed that the discrepancy between experimental data and the best fit models could be due to the Kapitza resistance, or the thermal resistance due to interfaces and grain boundaries [28, 77].

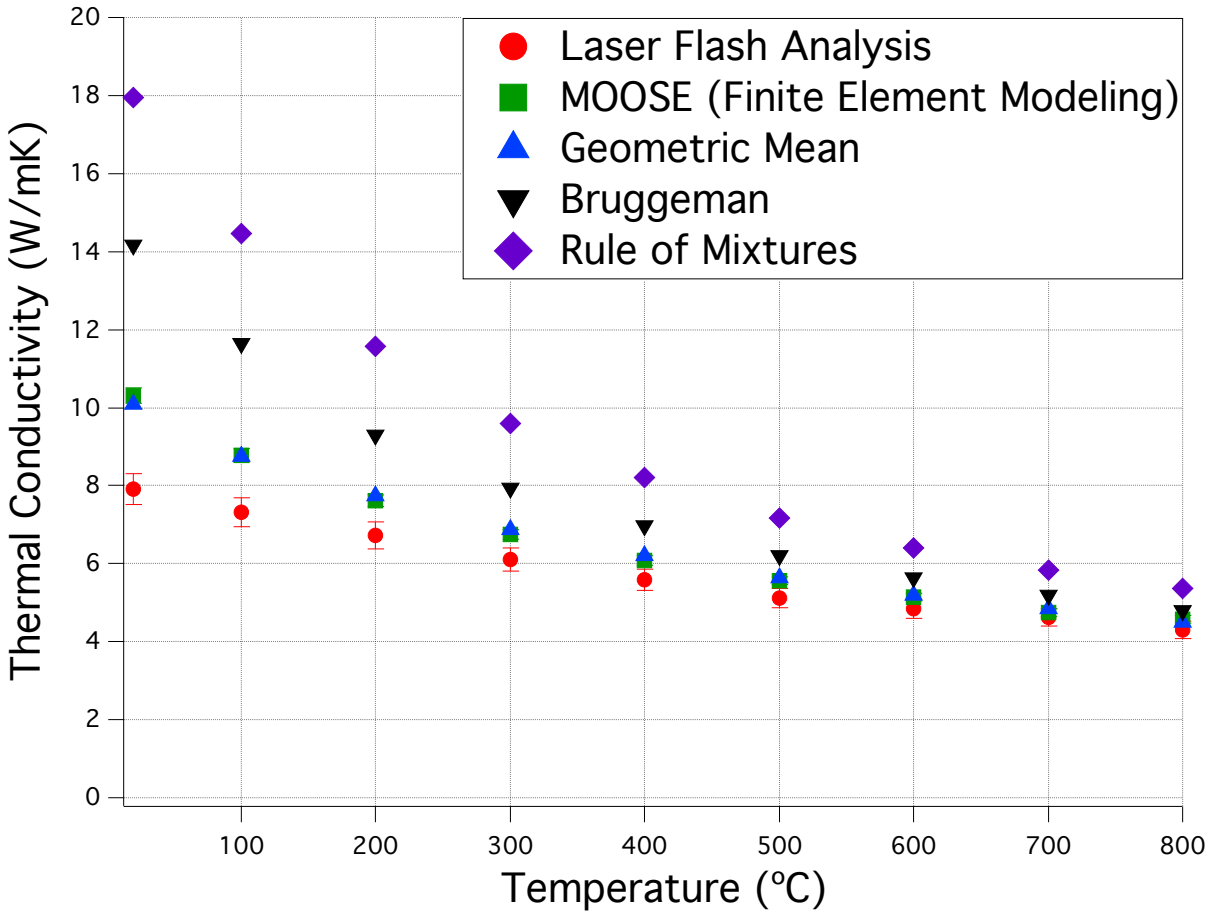

Figure 3.6 Thermal conductivity as a function of temperature for the 450 nm grain size Al_2O_3-$MgAl_2O_4$-8YSZ composite measured experimentally modeled using finite element modeling via MOOSE, Geometric Mean, Bruggeman, and Rule of Mixtures calculations.

3.4.3 Kapitza resistance of three-phase composites

The Kapitza resistance of single- and two-phase systems has been studied for a limited range of oxides and composites [30, 33, 78, 79]. Several models have been proposed to calculate the Kapitza resistance. The model of Smith *et al.* [78] assumes that all of the scattering from thermal conductivity extrapolated to 0K is due to grain boundaries and neglects scattering from point defects and other defects. This model also fails to capture any temperature dependence of the Kapitza resistance. A better model developed by Yang *et al.* [38] uses the changes in thermal conductivity with grain size to predict the temperature and grain size dependence of Kapitza resistance [28, 36, 80]. This approach uses the following equation to express the Kapitza resistance as a function of temperature:

$$k(T,d) = \frac{d\, k_i(T)}{d + R_k k_i(T)} \tag{3-6}$$

where $k(T,d)$ is the temperature and grain size dependent thermal conductivity [W/mK], d is the grain size [m], $k_i(T)$ is the intrinsic thermal conductivity which is dependent on temperature but independent of grain size [W/mK], and R_k is the Kapitza resistance [m^2K/W]. This equation has been successfully used for calculations of Kapitza resistance in single-phase oxides [28, 33]. Here, we use it for a three-phase calculation utilizing the results from both experiment ($k(T,d)$) and finite element modeling ($k_i(T)$). The experimentally measured thermal conductivity values are known to be both temperature and grain size dependent. However, the modeled results are independent of grain size, which allows the MOOSE values to serve as the intrinsic thermal conductivity. The thermal conductivity inputs for MOOSE are taken from literature from materials with grain sizes significantly larger than 1 μm, where the few interfaces make negligible impact on the thermal conductivity [65-67]. A plot of Kapitza resistance as a function of temperature is given in Figure 3.7 for the three-phase composite as well as single-phase YSZ [28].

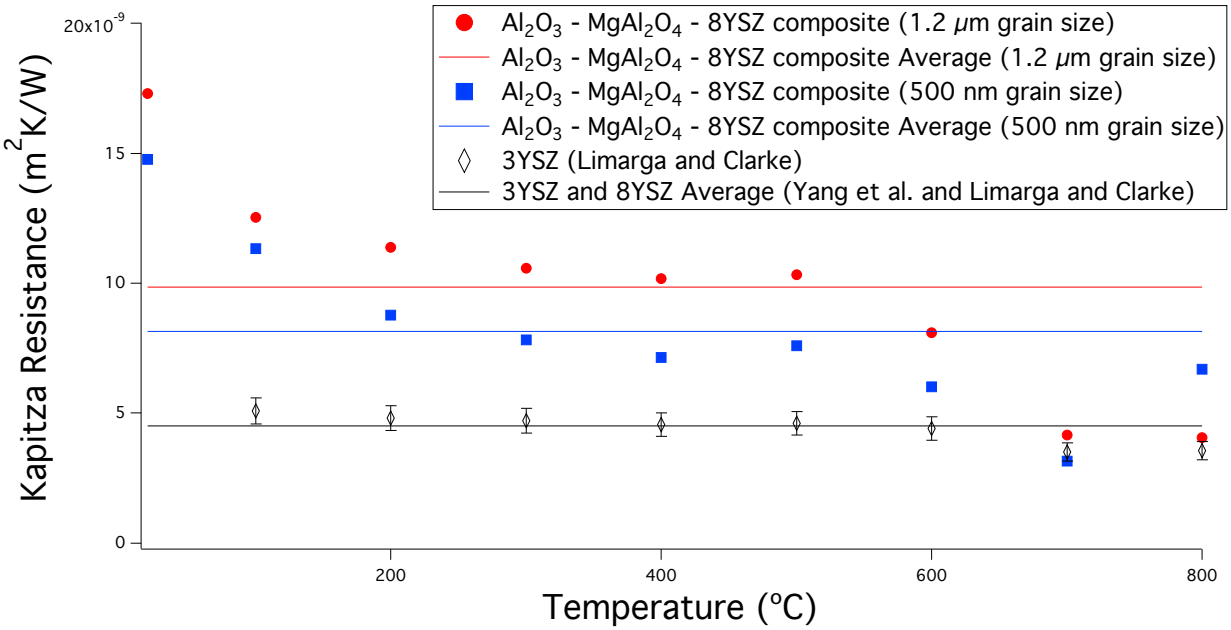

Figure 3.7 Kapitza resistance as a function of temperature comparing three-phase material with two different grain sizes with prior results on 8YSZ using the temperature dependent method based on the work of *Limarga and Clarke* and Yang *et* al [28, 33].

Using this method, the average Kapitza resistance of the three-phase material with 1.2 μm grain size is determined to be 9.8 x 10^{-9} m^2K/W and the average Kapitza resistance of the 450 nm grain size material is 8.1 x 10^{-9} m^2K/W. Both values are significantly higher than the values for 3YSZ and 8YSZ of 4.5x10^{-9} m^2K/W, as shown in Table 1. Both of these values are the averaged value from 25 °C to 800 °C, but it can be seen from Fig. 3.7 that there appears to be a strong temperature dependence, with a drop in Kapitza resistance at higher temperature (>600 °C) for both the composite and YSZ. At room temperature, the Kapitza resistance of the composite is 1.5-1.7 x 10^{-8} m^2K/W which is significantly larger than the single-phase values for 8YSZ at room temperature (4.5 x 10^{-9} m^2K/W). We know that at higher temperatures, there is increased solubility of yttria in zirconia and less segregation at the grain boundaries which may lead to this decrease

in Kapitza resistance in YSZ [81]. The composite sees a 30% drop in resistance and the YSZ sees an approximate 20% drop in resistance from 600 °C to 700 °C. This trend of the composite thermal conductivity decreasing as a function of temperature at high temperatures suggests that in many materials the Kapitza resistance may be dependent on solubility and grain boundary segregation, so ignoring the temperature dependence may not be correct.

The difference in Kapitza resistance values at all temperatures for the two composites is hypothesized to be a result of the grain boundary character and type. Since the two samples were annealed and sintered at different temperatures for different amounts of time there may be a reduction of low energy boundaries at the higher annealing temperature, which may contribute to the higher Kapitza resistance values for larger grain sizes. Research by Chernatynskiy *et* al. [82] on the Kapitza resistance of CeO_2 found that the Kapitza resistance is highly dependent on the misorientation angle and grain boundary energy [82].

Table 3.1 Kapitza resistance values from the temperature dependent method for the three-phase composite and single-phase YSZ. The grain size is included as it is used in the calculation of Kapitza resistance per equation 5.

Material	Average Kapitza Resistance (m^2K/W)	Kapitza Resistance at 25°C (m^2K/W)	Grain Size	Reference
Al_2O_3-$MgAl_2O_4$-8YSZ	9.8×10^{-9}	1.7×10^{-8}	1.2 μm	This Work
Al_2O_3-$MgAl_2O_4$-8YSZ	8.1×10^{-9}	1.5×10^{-8}	450 nm	This work
3YSZ	4.5×10^{-9}	4.5×10^{-9}	120 nm	*Limarga and Clark*[32]
8YSZ	4.5×10^{-9}	4.5×10^{-9}	10 – 100 nm	*Yang et al.*[38]

These results indicate that the additional phases in the composite lead to an increase in the overall Kapitza resistance compared to single-phase systems. We postulate this is due to the heterogeneous nature of the interfaces compared to the homogeneous grain boundaries in single-phase materials. Within the bulk composites studied here, there are many difference types of grain boundaries as well as different chemistries across the boundaries. There are six possible interfaces present in the bulk material: Al_2O_3 - Al_2O_3, Al_2O_3 - $MgAl_2O_4$, Al_2O_3 - 8YSZ, $MgAl_2O_4$ – $MgAl_2O_4$, $MgAl_2O_4$ – 8YSZ, and 8YSZ – 8YSZ, with interfaces between dissimilar phases which we hypothesize results in the increased Kapitza resistance of multiphase ceramics compared to single phase boundaries. The heterointerfaces may serve as more effective blocks to phonon transport.

3.4.4 Calculated thermal conductivity as a function of grain size at 25 °C and 800 °C

Differences in crystal structure and elastic modulus between each phase have been previously calculated to affect the Kapitza resistance [35]. Prior experiments on significantly reducing the thermal conductivity by reducing the grain size of ceramics, mostly found this effect with ≤100 nm grain size ceramics [28, 83]. We hypothesize that the presence of heterointerfaces degrades thermal conductivity at larger grain sizes compared to single-phase materials, since our materials had grain sizes from 450 nm to 1.2 μm, yet none of the models were able to accurately determine the thermal conductivity as measured experimentally by laser flash analysis, dilatometry, and differential scanning calorimetry. Heterointerfaces will therefore have a significant impact on lowering the thermal conductivity, depending on the temperature range of interest. Figure 8 shows the predicted thermal conductivity including Kapitza resistance of the three-phase composite as a function of grain size for two temperatures, 25 °C and 800 °C. At room temperature, any reduction in grain size below 10 μm will lower the thermal conductivity for this three-phase material. In contrast, published calculations incorporating Kapitza resistance for 8YSZ show that a plot of the thermal conductivity as a function of grain size for single-phase 8YSZ reaches a near constant maximum thermal conductivity at 1 μm grain size at 27 °C [84]. (Kapitza resistance values for Al_2O_3 and $MgAl_2O_4$ using the temperature dependent Kapitza calculation could not be found in the published literature.)

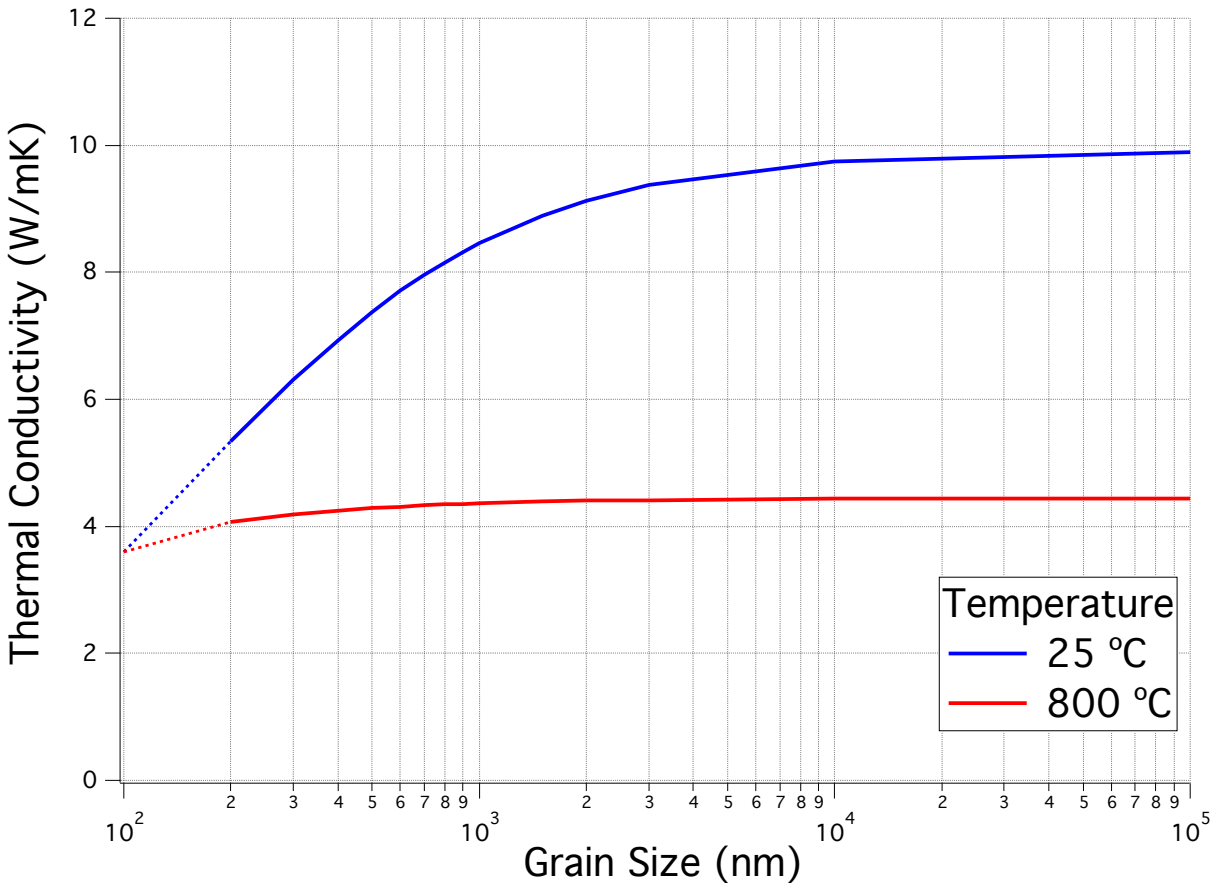

Figure 3.8 Predicted thermal conductivity incorporating Kapitza resistance in OOF2/MOOSE as a function of grain size for the three-phase Al_2O_3-$MgAl_2O_4$-8YSZ. This calculation assumes the microstructure will be self-similar at all grain sizes. The actual Kapitza resistances calculated at different temperatures from Figure 7 were used. Dotted lines below 200 nm indicate the beginning of the limits of MOOSE.

The premise of inert matrix fuel research is largely predicated on increasing the thermal conductivity of the fuel. In this instance, the effective thermal conductivity of the composite is predicted to increase by a factor of two at 25 °C when compared to conventional UO_2 fuel. A nanocrystalline grain size would be desirable for improved mechanical properties and higher radiation damage tolerance with grain boundaries serving as effective sinks for point defects

generated during irradiation. However, Figure 3.8, clearly shows that this doubling of the thermal conductivity by making a composite would be completely negated if the grain size is reduced to a nanocrystalline grain size, creating more interfaces with high Kapitza resistance. This reduction is most striking at lower temperatures. The thermal conductivity decreases only 15% between 1 μm and 100 nm at 800°C, but there is a 100% reduction at 25°C over the same range of grain sizes. (A different model that accounts for atomistic effects is necessary for simulating the effective thermal conductivity below 100 nm).

3.4.5 Investigation into Kapitza Resistance of Two-and Three Phase Composites by Extrapolation of Thermal Resistivity

Efforts to fabricate and measure the thermal conductivity of the constituent two-phase ceramic composites are currently ongoing. However, finite element models have been used to simulate the thermal conductivity of Al_2O_3 – $MgAl_2O_4$, Al_2O_3 – 8YSZ, and $MgAl_2O_4$ – 8YSZ composites. Within this section, these results will be presented as well as insight into an alternative method from literature that can be used to estimate the Kapitza resistance. As mentioned earlier, this methodology from an article by Smith *et al.* [78] does not have a temperature dependence. As shown in the previous sections, it is hypothesized that there is a temperature dependence of the Kapitza resistance and it may be exaggerated for composites.

The Kapitza resistance can be calculated from a graph of thermal resistivity (the inverse of thermal conductivity) as a function of temperature. As discussed in Smith *et al.* [78], the thermal resistivity as a function of temperature should have a linear dependence and follow the equation:

$$\frac{1}{k(T)} = A + B \cdot T \tag{3-7}$$

Where A is the thermal resistivity term for impurity scattering and B is the thermal resistivity term of phonon-phonon scattering [85]. In this formulation, the impurity scattering term is independent of temperature and in the derivation of Smith *et al*. [78], only accounts for thermal resistance due to grain boundaries and not point defects. However, point defects may scatter phonons much more efficiently than grain boundaries [28].

To start, the thermal resistivity as a function of temperature is plotted for the experimental measurements and simulated OOF2 data for the three-phase composite (Fig. 3.9). This value will be compared to the average value calculated previously. The y-intercept of each line is determined from the plot and used in conjunction with the linear average grain size to calculate the Kapitza resistance by the equation:

$$R_K = A * d \tag{3-8}$$

where R_K is the Kapitza resistance (units m^2K/W), A is the y-intercept which represents the scattering of phonons by defects (units mK/W), and d is the linear average grain size (units m).

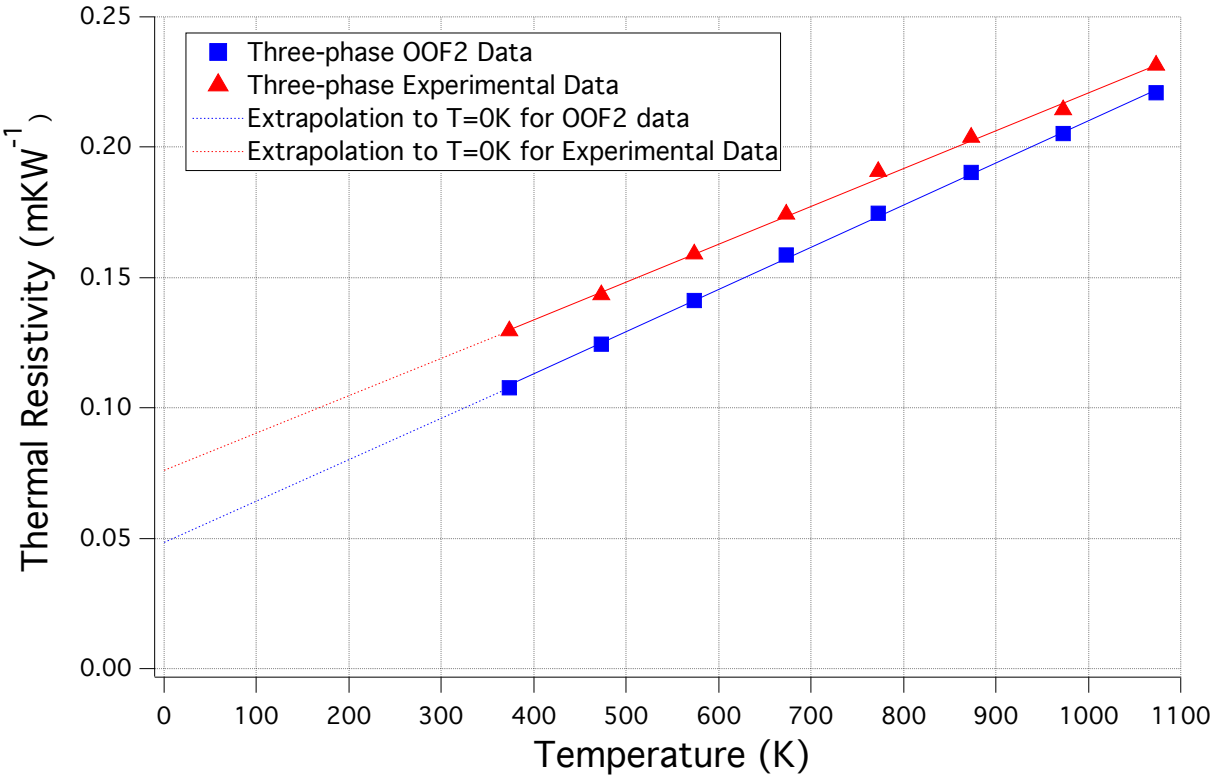

Figure 3.9 Thermal resistivity as a function of temperature for the three-phase composite with large-grain size extrapolated to T = 0 K.

The values for both the OOF2 modeled data and the experimental data were calculated to be $2.9x10^{-8}$ m^2KW^{-1} and $4.6x10^{-8}$ m^2KW^{-1}, respectfully. Smith *et al.* calculated the Kapitza resistance of Al_2O_3 to be $1.3x10^{-8}$, which has the same order of magnitude as the values determined for the three-phase composite (Table 3.2) [78]. The values calculated from both the Yang technique and the Smith technique deviate by about an order of magnitude [38,78]. This may be due to how the Kapitza resistance is derived when extrapolating thermal resistivity to 0 K. In this derivation, the "A" term contains thermal resistivity information related to both the scattering due to grain

boundaries and point defects. By subtracting the temperature dependent Kapitza resistance from the resistance calculated by the scattering term, the thermal resistivity due to point defects may be back calculated. Nevertheless, in both cases, the Kapitza resistance of the composite is higher than the Kapitza resistance of the single-phase material available in the literature. It is recommended that the model described in early section be used instead of the Smith model [78] due to the likely temperature dependence of the Kapitza resistance, which has also been observed in more recent studies [82].

Table 3.2 Kapitza resistance values calculated with the y-intercepts from Fig. 3.9 using the Smith method. Both the experimental and OOF extrapolations are presented as well as the Kapitza resistance for porous Al_2O_3 determined by Smith *et al.* [78].

	Kapitza Resistance (m^2KW^{-1})
Experimental Data	$4.6x10^{-8}$
OOF2 Data	$2.9x10^{-8}$
Al_2O_3 [31]	$1.3x10^{-8}$

Preliminary research has also investigated the three binary-phase composites of Al_2O_3-$MgAl_2O_4$, Al_2O_3-8YSZ, and $MgAl_2O_4$-8YSZ with equal volume fractions. As expected, the composites containing Al_2O_3 have higher thermal conductivity values than the composite containing $MgAl_2O_4$ and 8YSZ (Figure 3.10).

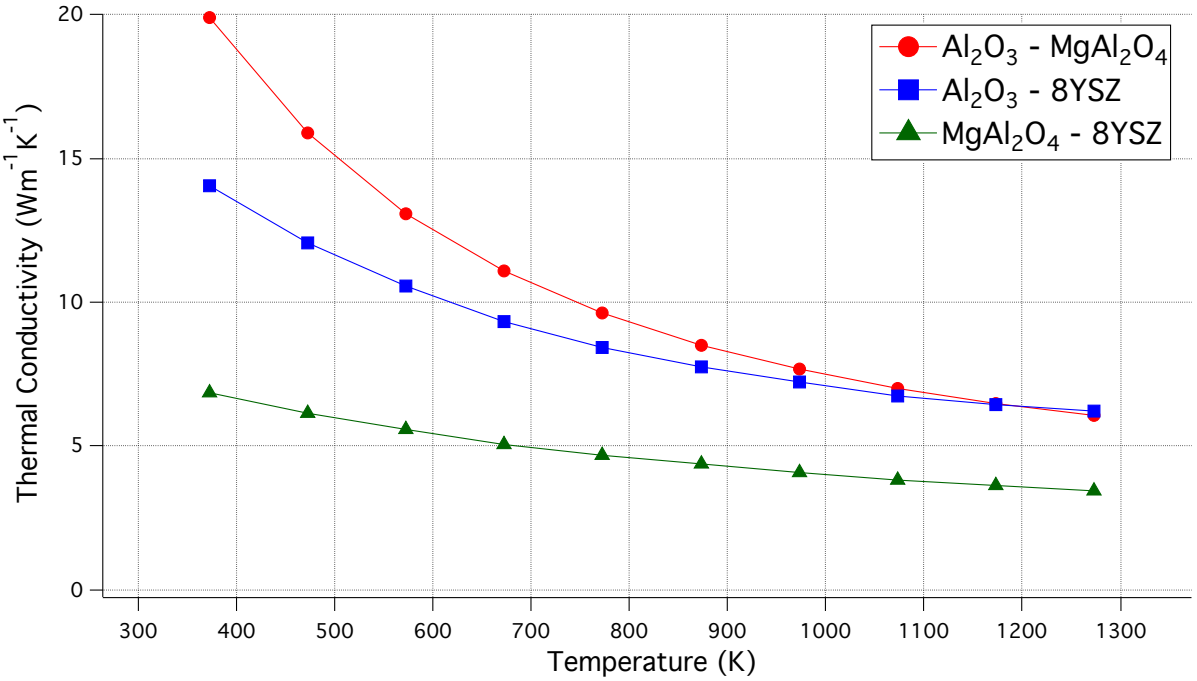

Figure 3.10 OOF2 simulations of the thermal conductivity as a function of temperature for three binary-phase composites showing the composites containing Al_2O_3 have higher thermal conductivities.

Analyzing these systems also allows for the estimation of the thermal resistance due to defects via the Smith technique (Figure 3.11). The Kapitza resistances obtained from the linear extrapolation of thermal resistance as a function of temperature at 0 K are of the same order of magnitude as the values reported in literature for single phase materials as well as the calculated values for the three-phase composite (Table 3.3) and demonstrate that different composite systems have different average Kapitza resistance values. However, these thermal resistances are possibly

dominated by the value for the thermal resistance of point defects. Future work is underway to characterize the effect of dissimilar interfaces within each binary-phase composite on the thermal conductivity.

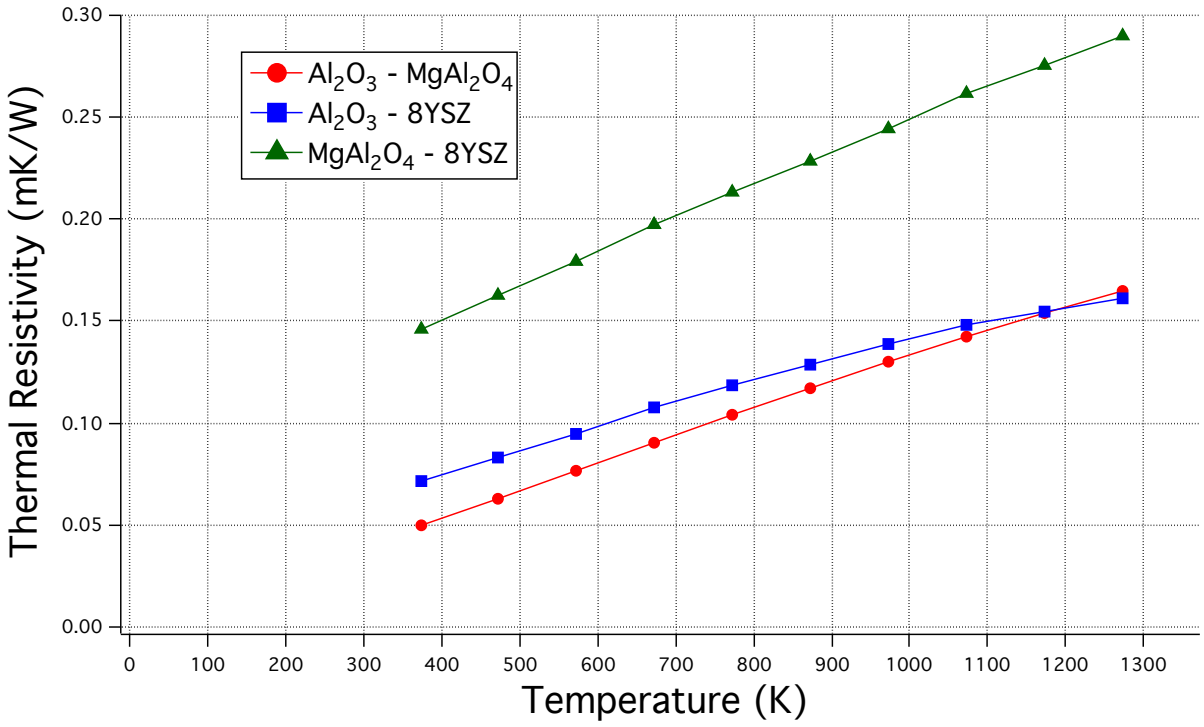

Figure 3.11 Inverse thermal conductivity as a function of temperature plots used to calculate the Kapitza resistance via the Smith technique for the three binary-phase composites.

Table 3.3 Extrapolation of y-intercept values from **Fig. 3.11.** The Smith technique was applied and the Kapitza resistance for each of the binary phase composites was calculated.

	Y-intercept from Fig. 20.	ϕ* (Linear Average Grain Size)	Kapitza Resistance (m^2*K*W^{-1})
Alumina/Spinel	0.0873193	$6.0x10^{-7}$	$5.239x10^{-8}$
Alumina/YSZ	0.0365913	$6.0x10^{-7}$	$2.195x10^{-8}$
YSZ/Spinel	0.0027275	$6.0x10^{-7}$	$1.637x10^{-8}$

3.5 Conclusions

The thermal conductivity was experimentally determined and modeled for a three-phase Al_2O_3-$MgAl_2O_4$-8YSZ ceramic composite with different grain sizes. A reduction in thermal conductivity is attributed to the Kapitza resistance, which was calculated for each composite. The calculated Kapitza resistance of the three-phase composite with 1.2 μm grain size has an average value of 9.8 x 10^{-9} m^2K/W from 25 °C – 800 °C and the composite with 450 nm grain size has an average Kapitza resistance of 8.1 x 10^{-9} m^2K/W, Kapitza resistance values higher than found in literature for YSZ. There is also a strong temperature dependence of the Kapitza resistance. This increased Kapitza resistance is attributed to the presence of heterointerfaces within the composite, and it is hypothesized that the Kapitza resistance of heterointerfaces in composites is intrinsically higher than the Kapitza resistance of grain boundaries in the corresponding single-phase materials. While nanocrystalline inert matrix fuels would have detrimentally lowered thermal conductivity due to the heterointerfacial Kapitza resistance, lower temperature applications such as thermoelectrics can use this effect by using composite heterointerfaces and reduced grain sizes in order to decrease thermal conductivity. Further research is ongoing on analyzing the types of oxide interfaces that are most effective in reducing thermal conductivity.

3.6 Acknowledgements

Co-authors for this work include: Andrew T. Nelson of Los Alamos National Laboratory and Kara J. Phillips-Bridges and Martha L. Mecartney of University of California, Irvine. Materials preparation, LFA measurements, and preliminary computational modeling were conducted based in part on work supported by the Department of Energy under Award Number DE-NE0000711. Final results on the computational work were supported by NSF DMR 1611457. SEM and XRD work were performed at the UC Irvine Materials Research Institute (IMRI). AWT acknowledges support from UCI for a fellowship funded by the Nuclear Regulatory Commission (NRC).

Chapter 4: Comparison of Laser Flash Analysis and 3 Omega Method Thermal Measurement Techniques on 8YSZ and an Al_2O_3 – $MgAl_2O_4$ – 8YSZ Composite

4.1 Abstract

In this chapter, a technique for making low temperature thermal conductivity is discussed and applied to ceramic samples. This technique, known as the 3ω Method, is outlined from sample preparation through data analysis and the results are compared to the more traditional technique of laser flash analysis. Three samples were prepared for each technique: single-phase 8YSZ and a three-phase composite of Al_2O_3, $MgAl_2O_4$, and 8YSZ with two distinct grain sizes. A fourth sample of polycrystalline $MgAl_2O_4$ was also prepared and measured via 3ω method and compared to literature results from laser flash analysis studies. Results show that all four samples have agreement between the two techniques, with thermal conductivity values from 3ω measurements falling within the error range associated with the propagation of error from laser flash analysis, differential scanning calorimetry, and dilatometry. This work is the first time 3ω measurements of bulk ceramic materials have been validated against thermal conductivity results from laser flash analysis. Finally, future work on how to use the 3ω Method for potential measurement of the Kapitza resistance, or interfacial thermal resistance, across bicrystals or materials with very large grains will be discussed.

4.2 Introduction

The thermal conductivity of crystalline ceramics has been studied extensively for a range of materials, composites, and systems [28]. A traditional technique for experimentally calculating the temperature dependent thermal conductivity of a material is the use of laser flash analysis in conjunction with dilatometry and differential scanning calorimetry [86]. Within this paper, the 3ω method for measuring thermal conductivity is compared to the laser flash analysis. The differences between the two techniques will be discussed as well as the preparation required to complete a measurement.

The 3ω method was pioneered by Cahill in 1990 and is an electrothermal technique for extracting the thermal conductivity of a bulk or thin film material [87]. This technique has been extensively used to study glasses, metals, and composites [88,89]. However, very few bulk ceramic materials have been studied [72] and no 3ω results for bulk ceramics have been compared to results from laser flash analysis on the same materials. While both 3ω method and laser flash analysis (which will be used to express the combination of laser flash analysis, differential scanning calorimetry, and dilatometry), measure thermal conductivity, they have different operating temperature ranges. Laser flash analysis has the capability to go from cryogenic temperatures to temperatures in excess of 2000 K making it a very robust measurement system [90]. On the other hand, 3ω has a rather limited temperature range of cryogenic to approximately 750 K [87]. This limitation is imposed by the temperature sensitivity of the electrode and heater line. While the focus has been mainly on the laser flash method, ideally three separate measurement measurements for thermal diffusivity, density, and specific heat capacity are necessary to satisfy Eq. 4-1 for thermal conductivity.

$$\lambda(T) = \alpha(T)\rho(T)c_p(T) \tag{4-1}$$

Therefore, the laser flash method requires three individual samples for three separate measurements. A benefit of the 3ω method is that only one sample is required to extract thermal information from the sample. Multiple samples are run per material for statistical purposes.

Within this chapter, the thermal conductivity of a single-phase 8 mol% yttria-stabilized zirconia (8YSZ) and magnesium aluminum spinel ($MgAl_2O_4$) were measured with 3ω method and compared to either experimental laser flash analysis results or literature values to determine the efficacy of the 3ω technique. Next, the temperature dependent thermal conductivity of a three-phase composite consisting of equal volume fractions of 8YSZ, aluminum oxide (Al_2O_3), and $MgAl_2O_4$ was measured for two different grain sizes. This chapter outlines the necessary steps required to fabricate samples as well as perform the measurement and analysis. Finally, the accuracy of 3ω compared to laser flash analysis will be determined.

4.3 Experimental Procedures

4.3.1 Sample Preparation and Characterization

Single-phase samples were prepared by milling either cubic 8YSZ (TZ-8YS, Tosoh USA, Grove City, OH) or ($MgAl_2O_4$ S30CR, Baikowski, Charlotte, NC) for 8 hours in an attrition mill. The resulting slurries were dried, ground with an agate mortar and pestle, and pressed in a cold isostatic press for 5 minutes at 55 kpsi. The cylindrical green bodies had green densities of approximately 55% theoretical density. The green bodies were then sintered in air at 1550°C for 10 hours to 98 - 99% theoretical density. Square samples measuring 8 by 8 by 2 mm were cut for LFA and 3ω measurements. A similar approach was taken for the three-phase composites consisting of alumina (TM-DAR, Taimicron, Japan), spinel (S30CR, Baikowski, Charlotte, NC), and cubic 8YSZ (TZ-8YS, Tosoh USA, Grove City, OH). However, to achieve a finer grain sized material, a two-step sintering route was utilized; the sample was sintered at 1425°C for 5 minutes before the temperature is lowered to 1325°C for 5 hours. Both microstructures were sintered to approximately 97% theoretical density. All density measurements were performed using the Archimedes displacement method and confirmed using a geometric density measurement. The grain size and phase fractions were determined via scanning electron microscopy (SEM) (FEI Magellan XHR SEM, Hillsboro, OR). As reported in Chapter 3, the two grain sizes are 1.2 μm and 500 nm with similar compositions of all three constituent phases.

4.3.2 3ω Method

To prepare samples for 3ω measurement, a methodology developed by Professor Dames at University of California, Berkeley was followed [91]. First, the 4-point probe electrodes were deposited using electron beam evaporation (Angstrom Engineering, EvoVac Glovebox Evaporator, Kitchener, Ontario, Canada). A shadow mask of the electrode (Photo Science

Company, Torrance, CA) was affixed to the surface of the samples before a 100 nm gold layer was deposited on a 10 nm chromium adhesion layer. The shadow mask was removed and the samples with electrodes were ready to be connected to the 3ω instrumentation. Silver epoxy was used to affix the pads of the electrodes to thin copper wire. The copper wire was subsequently soldered to thicker gauge copper wire which is more durable to gator clip connection. The first measurement for a sample is the resistance of the heater line measured using a multimeter (Keithley, Beaverton, Oregon) to ensure proper connections and uniform deposition of the electrodes. Samples are judged suitable if the resistance of the heater is line is below 10 Ω.

First, a thermal contact resistance (TCR) calibration of the heater line was performed. With the 3ω sample connected to the multimeter, voltage measurements as a function of current were recorded at various temperatures to determine the resistance at 0°C of the heater line. This calibration is required for thermal conductivity calculation and is unique to every individual heater line. The sample is placed on top of a hotplate which supplies constant temperature to the sample allowing for temperature dependent measurements. The temperature of the sample itself is monitored with a J-type thermocouple, which is mounted directly to the surface of the sample.

The in-phase and out-of-phase 3ω data was collected as a function of frequency for each sample at temperatures ranging from ~20°C to 150°C using a circuit board from Design Solutions, Inc. (Chanhassen, MN, USA). With the 3ω output, the thermal conductivity was calculated by both the in-phase and out-of-phase signals. This process will be presented in further detail in Chapter 4.4.2 and Appendix C.

4.3.3 Laser Flash Analysis

Square specimens were fabricated ~8 by 2mm for the LFA measurements. Diffusivity values were determined by fitting the temperature rise signal with a Cowen model. The LFA (Netzsch Instruments, Germany) method was utilized to determine the thermal diffusivity, D, of the samples. Samples were first coated with approximately 10 nm of Pt using a standard sputter coater. A second layer of graphite spray (Graphit 33, Kontakt Chemie, Germany) was then applied on top of the Pt later to improve absorption of the laser energy on the bottom face and enhance emissivity of the upper face. Laser flash analysis was then performed in an atmosphere of flowing argon. Diffusivity data was collected from room temperature up to 300 ^{0}C in increments on heating of 50 ^{0}C. Three shots per temperature were collected and the data shown the average for the reported value. The standard deviation of the thermal diffusivity data at each step was far below the standard error associated with the technique (3%) [75].

4.4 Results and Discussion

4.4.1 Calculating thermal conductivity using laser flash analysis

To calculate the thermal conductivity of a material using laser flash analysis, three experiments were performed; laser flash analysis, differential scanning calorimetry, and dilatometry. The thermal diffusivity of single-phase 8YSZ and the three-phase composites were measured via laser flash analysis. As shown in Figure 4.1, the thermal diffusivity of 8YSZ is quite low when compared to the three-phase composites and agrees with reported thermal diffusivity values in literature. The thermal diffusivity of the three-phase composite was lowered by approximately 15% at room temperature from the 1.2 μm grain size to the 500 nm grain size at 25°C. The reduction becomes less pronounced at higher temperatures until the associated errors between the two samples begin to overlap around 400 – 500 °C. Overall, the addition of Al_2O_3 and $MgAl_2O_4$ to 8YSZ increases the thermal diffusivity at all temperatures.

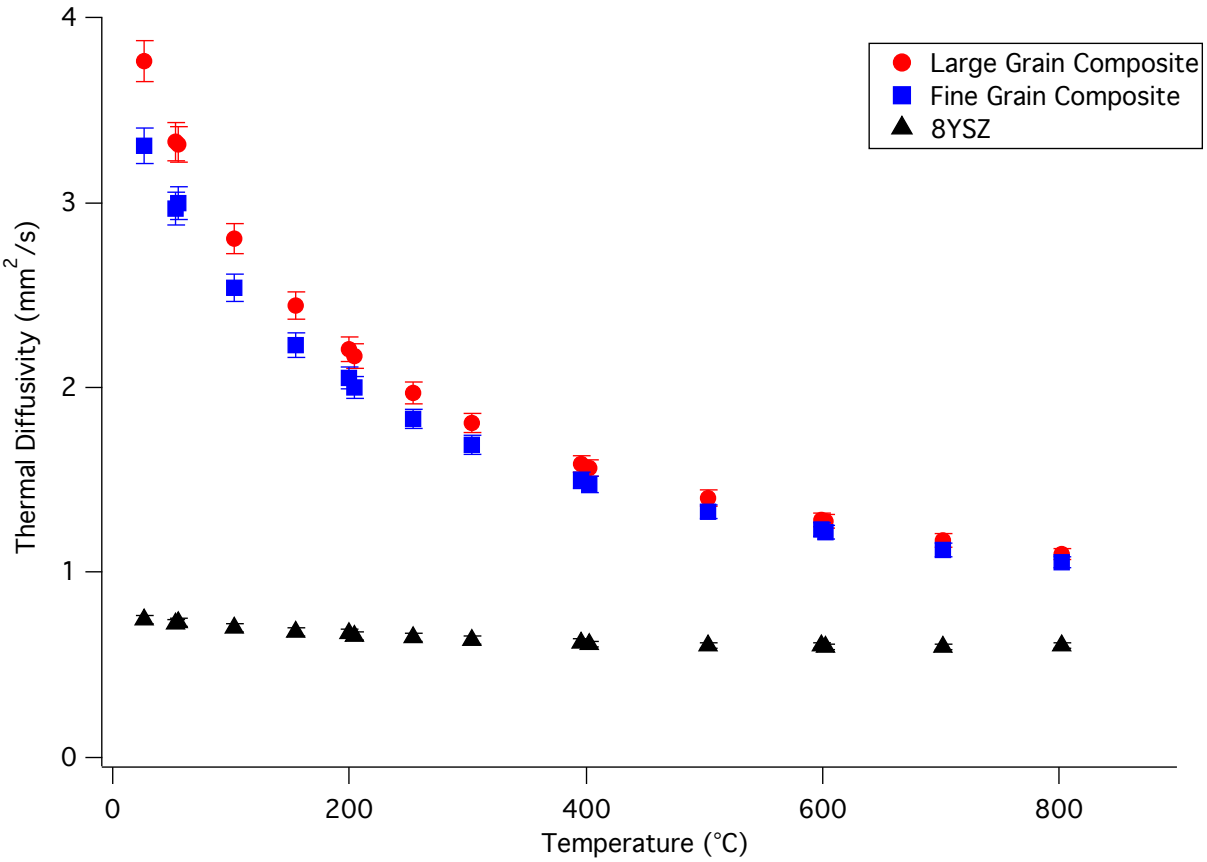

Figure 4.1 Thermal diffusivity as a function of temperature for 8YSZ and an Al_2O_3 – $MgAl_2O_4$ – 8YSZ composite with two distinct grain sizes as measured by laser flash analysis.

The specific heat capacity of the three-phase composite samples was also measured via differential scanning calorimetry. The specific heat capacity was assumed to be independent of grain size. The specific heat capacity as a function of temperature for an Al_2O_3 – $MgAl_2O_4$ – 8YSZ composite is shown in Figure 4.2.

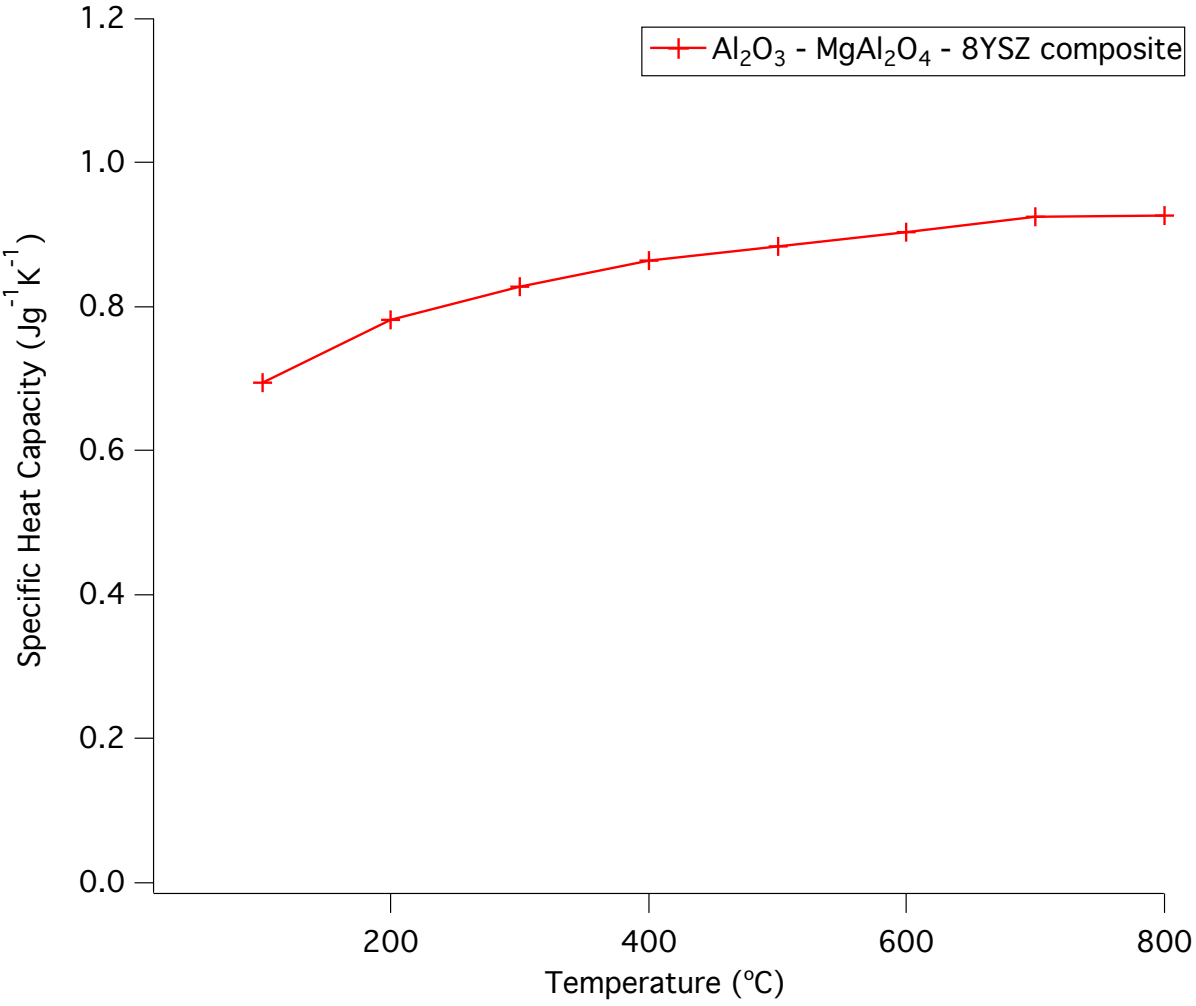

Figure 4.2 Grain size independent specific heat capacity as a function of temperature for equal phase fraction Al_2O_3 – $MgAl_2O_4$ – 8YSZ as measured by differential scanning calorimetry.

The final experiment for the full calculation of thermal conductivity as a function of temperature for the laser flash analysis is the measurement of thermal expansion via dilatometry. The thermal expansion as a function of temperature for the two distinct grain sizes for the Al_2O_3 – $MgAl_2O_4$ – 8YSZ are shown in Figure 4.3 Both sets of data were fit with a linear regression with a negative slope indicating positive thermal expansion values. The variances in starting densities was a result of the thermal processing of the two different samples which leads to two different

theoretical densities of the samples after densification by sintering. The density was taken into account after the calculation of the thermal conductivity; all samples were corrected to 100% theoretical density.

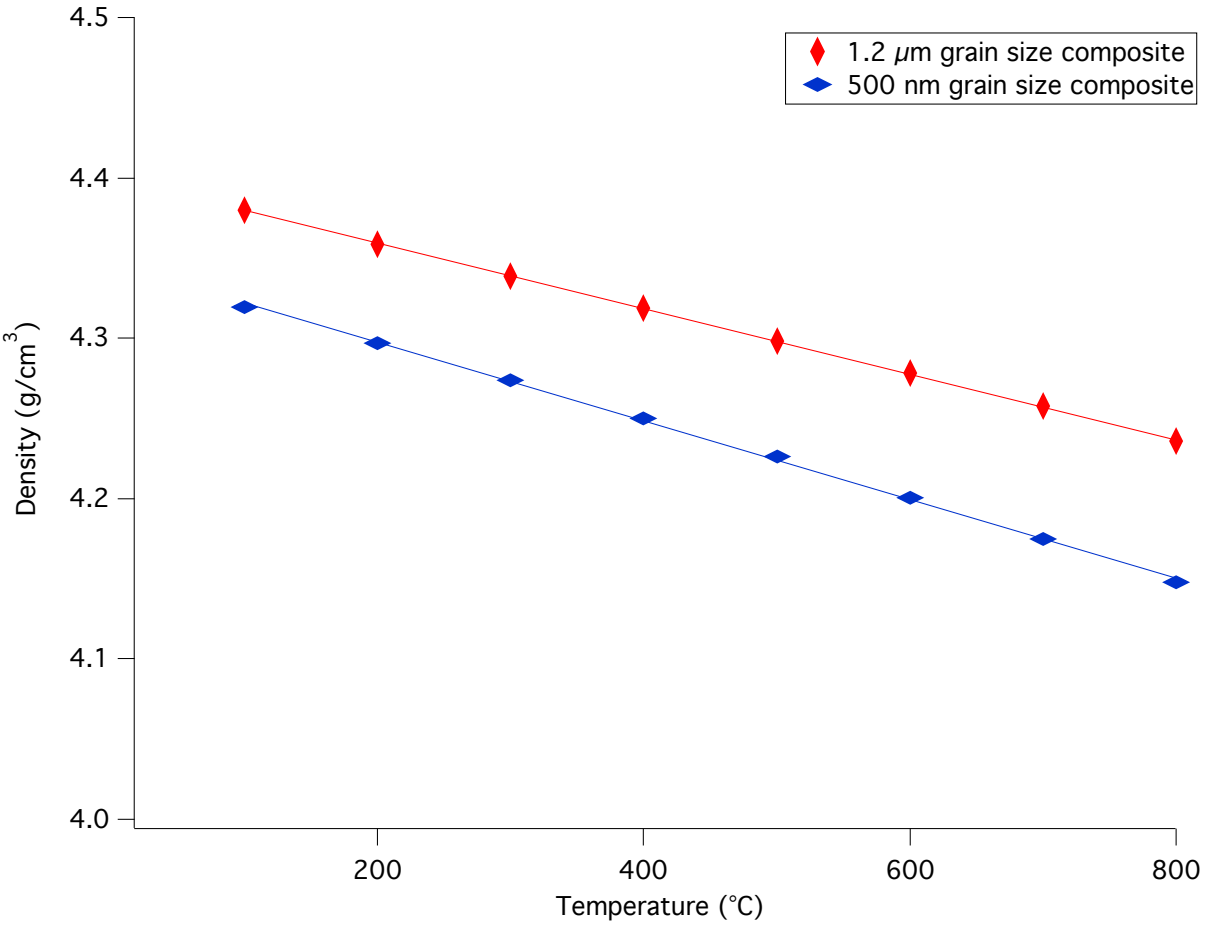

Figure 4.3 Density change as a function of temperature for Al_2O_3 – $MgAl_2O_4$ – 8YSZ composites with 1.2 μm and 500 nm grain sizes as measured by dilatometry.

The three values for thermal diffusivity, specific heat capacity, and density were multiplied together to calculate the temperature dependent thermal conductivity in accordance with Equation 4-1. Thermal conductivity values were corrected to 100% theoretical density with the following equation:

$$\kappa_{TD} = \kappa\left[1 - 3/2\left(1 - \frac{\rho_0}{\rho_{TD}}\right)\right]^{-1} \quad (4\text{-}2)$$

Where k_{TD} is the thermal conductivity at 100% theoretical density, k is the measured thermal conductivity at some nominal density, ρ_0 is the measured density, and ρ_{TD} is the 100% theoretical density. The thermal conductivity results are presented and compared to the 3ω measurements in the next subchapter.

4.4.2 Calculating thermal conductivity using 3ω method

In order to validate the 3ω method instrumentation, samples of single-phase 8YSZ and $MgAl_2O_4$ were prepared and analyzed as an initial benchmark experiment. 8YSZ and $MgAl_2O_4$ have been well studied in the literature and the thermal conductivity as a function of temperature is known [65, 92, 93]. The following procedure is undertaken for each 3ω sample. Initially, a 4-point probe was used to measure the resistance of the heater line that was evaporated on the sample. Resistance measurements for all heater lines vary from 5 - 9 Ω. The resistance of the heater line is a good indication of the quality of the evaporation. Previous attempts at using aluminum heater lines as opposed to gold yielded extremely high resistance values that were incompatible with the 3ω circuit board (maximum resistance of 50 Ω). It is advised that using the more expensive gold and chromium heater lines as opposed to aluminum will lead to easier 3ω measurements for ceramic samples.

All samples were calibrated using thermal contact resistance (TCR) measurements from temperatures ranging from 20 – 50 °C or 20 – 70 °C and input voltages from 0.2 – 0.4 mA. An example of the measurements is shown in Figure 4.4 for an 8YSZ sample. When the voltage as a function of resistance is plotted for the specified range of input currents, each temperature set has a very strong linear fit (indicated by an R^2 value of approximately 1.0). The y-intercepts of these regression was then used to determine the theoretical resistance of a cold heater line at 0 °C. An example of this regression is shown in Figure 4.5, where the slope and y-intercept of the linear fit were used to determine both the resistance of the heater line at 0 °C and α, the coefficient of thermal contact resistance. Both of these values are specific to each individual heater line and are necessary for calculating the thermal conductivity using the 3ω Method [91,94].

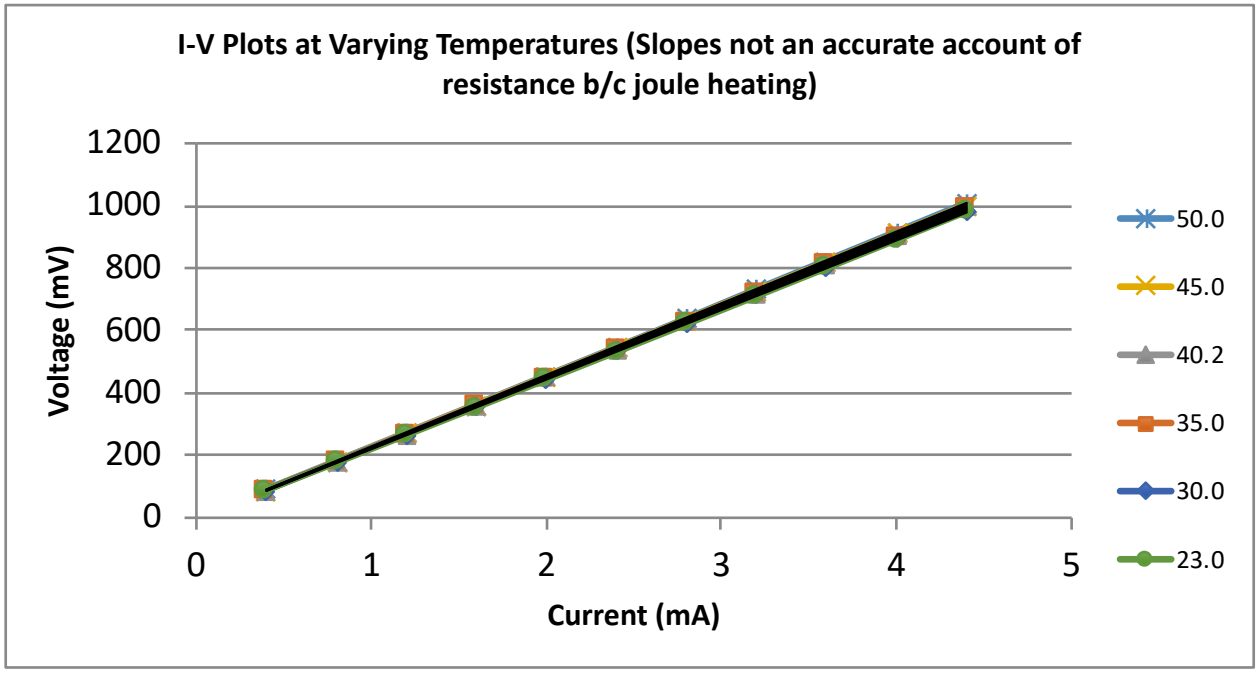

Figure 4.4 TCR calibration results for voltage as a function of current for various temperatures for single-phase 8YSZ.

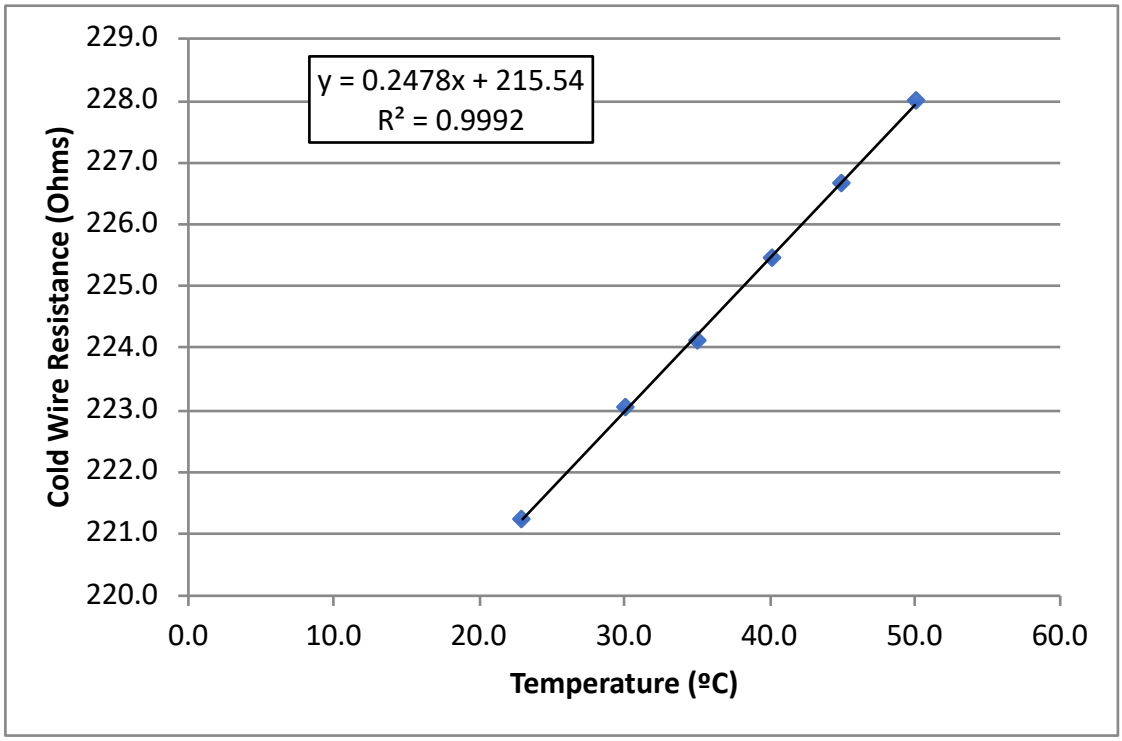

Figure 4.5 TCR calibration output for determining the resistance of the heater line at 0 °C and α, the coefficient of thermal contact resistance for 8YSZ.

With the heater line calibration completed, the in-phase and out-phase 3ω voltages were measured as a function of frequency. The frequency range was determined using the following relationships based on the thermal penetration depth, the heater line width, and the thickness of the sample:

$$\left(\frac{Sample\ Thickness}{5}\right) \geq L_p \geq 5 * (Heater\ Line\ Width) \tag{4-3}$$

Where L_p is the thermal penetration depth which can be estimated from the frequency (ω) by the relationship:

$$L_p \sim \frac{1}{\sqrt{\omega}} \tag{4-4}$$

Proper selection of the frequency range is imperative for accurately sampling the thermal transport within the bulk material. Selecting frequencies that are too high or low could result in measurements of the substrate below the bulk sample or surface effects. The frequency range, sampling rate, and input current were input by the user to the LabVIEW program before beginning a measurement.

The LabVIEW program measures and records the in-phase and out-of-phase 1ω and 3ω voltages as a function of frequency. An example of an entire 3ω data set is shown in Figure 4.6. When analyzing the data, there are certain criteria that need to be met for both the in-phase and out-of-phase signals to ensure confidence in the measurement. First, the in-phase 3ω signal should have a linear regime outside of the high frequency region. The slope of this region was used for the thermal conductivity calculation. Second, the out-of-phase 3ω signal should have a regime of constant voltages corresponding to the linear region in the in-phase signal. These out-of-phase voltages were also used to calculate the thermal conductivity values.

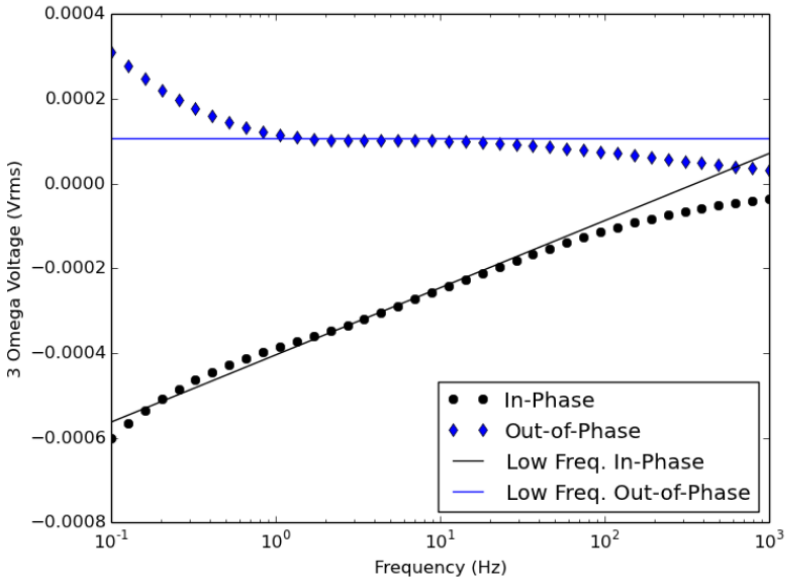

Figure 4.6 Example 3ω data set showing the in-phase and out-of-phase regimes. The fit trendline indicates the ideal regions for calculating thermal conductivity [91].

To calculate the thermal conductivity from the in-phase signal, the following equation was used:

$$k_{3\omega,ip} = \frac{\alpha R^2 I^3}{4\pi L} \left(\frac{dV_{3\omega}}{dln(\omega)}\right)^{-1} \tag{4-5}$$

Where $k_{3\omega,ip}$ is the thermal conductivity calculated from the in-phase 3ω voltage [W/mK], α is the temperature coefficient of thermal resistance [1/K], R is the electrical resistance [Ω], I is the electrical current [A], L is the length of the heater line [m], and $\frac{dV_{3\omega}}{dln(\omega)}$ is the slope from the linear regime of the in-phase 3ω voltage as a function of the natural logarithm of frequency. An example linear regression of this slope calculation is provided in Figure 4.7.

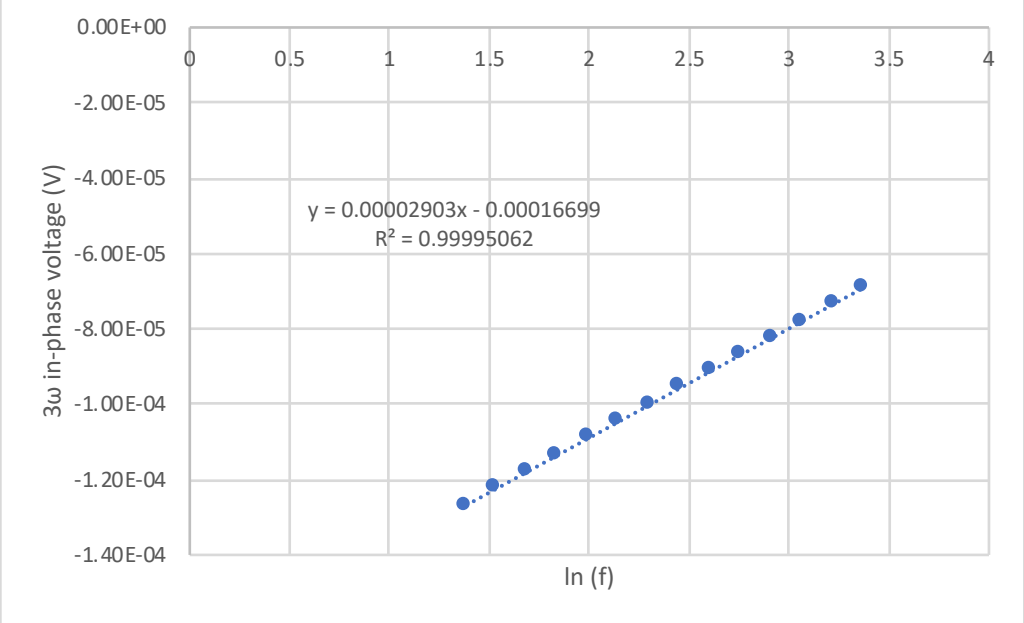

Figure 4.7 In-phase 3ω voltage as a function of ln(f) for single-phase 8YSZ. A highly linear regime was selected and the slope was calculated as a parameter for the thermal conductivity calculation in Eq. 4-5.

The corresponding constant out-of-phase 3ω voltage region should align well with the region displayed in Figure 4.7. The equation for calculating the thermal conductivity from the out-of-phase 3ω voltage is:

$$k_{3\omega,op} = \frac{\alpha R^2 I^3}{8LV_{3\omega,op}} \tag{4-6}$$

Where $k_{3\omega,op}$ is the thermal conductivity calculated from the out-of-phase 3ω voltage [W/mK] and $V_{3\omega,op}$ is the out-of-phase 3ω voltage [V]. Note that only one voltage value is used for the out-of-phase calculation. By selecting the out-of-phase region with constant values, there is little to no deviation in the calculated thermal conductivity. Most publications report the in-phase 3ω voltage calculation for thermal conductivity. However, the out-of-phase calculation should have minor deviations from the in-phase calculation and is a good internal check on the system.

4.4.3 Comparison of 3ω method and laser flash analysis for single-phase 8YSZ and $MgAl_2O_4$

The thermal conductivity of single-phase 8YSZ and $MgAl_2O_4$ were measured using the 3ω method from 25 – 150 °C. While Angle *et al.* conducting 3ω measurements on bulk ceramic samples, this is the first known measurement with validation against thermal conductivity results from laser flash analysis [72]. Figure 4.8 shows the comparison between the two experimental methods for 8YSZ with differences of less than 5% between techniques. The two experimental values also have good agreement with values for thermal conductivity for 8YSZ found in the literature from multiple researchers [56].

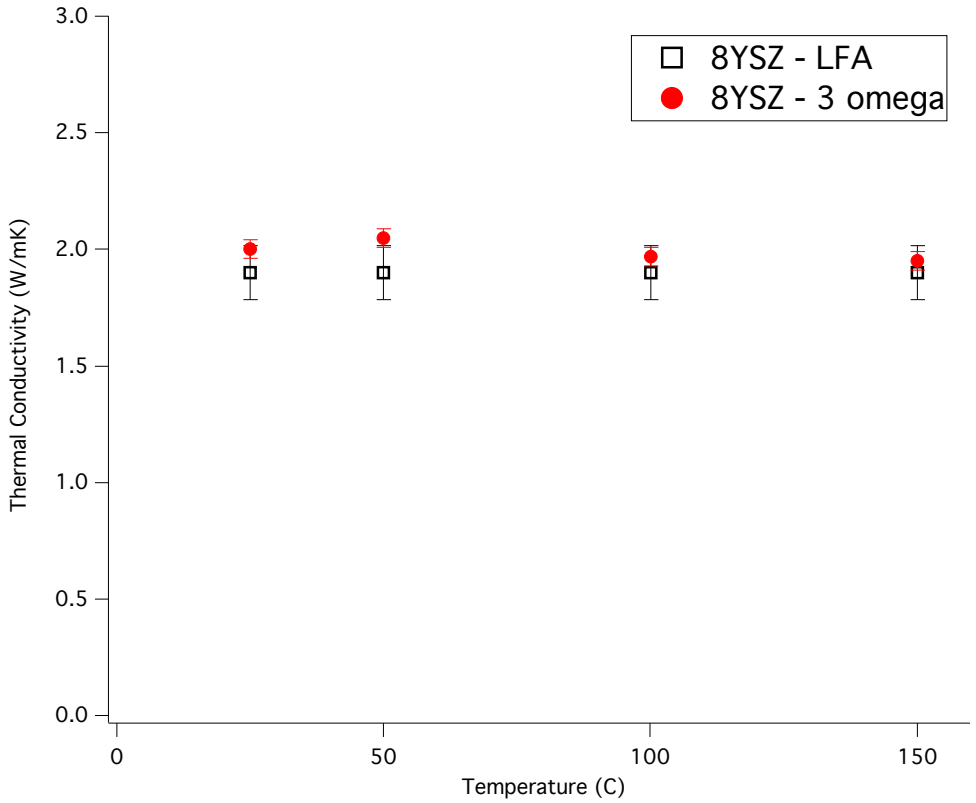

Figure 4.8 Comparison of thermal conductivity values for laser flash analysis and 3ω method for 8YSZ.

Similarly, Figure 4.9 compares the thermal conductivity of single-phase $MgAl_2O_4$ measured via the 3ω method with literature values from Wilkerson *et al.* collected using laser flash analysis. Again, the agreement between the two techniques was high, with the two data sets deviating by less than 5% for all 4 temperatures measured [67]. In this section, the 3ω method was used to accurately measure the thermal conductivity of low temperatures for two different single-phase oxide materials with varying thermal conductivities. Next, the thermal conductivity of a multiphase oxide system with similar composition but varying grain size will be analyzed.

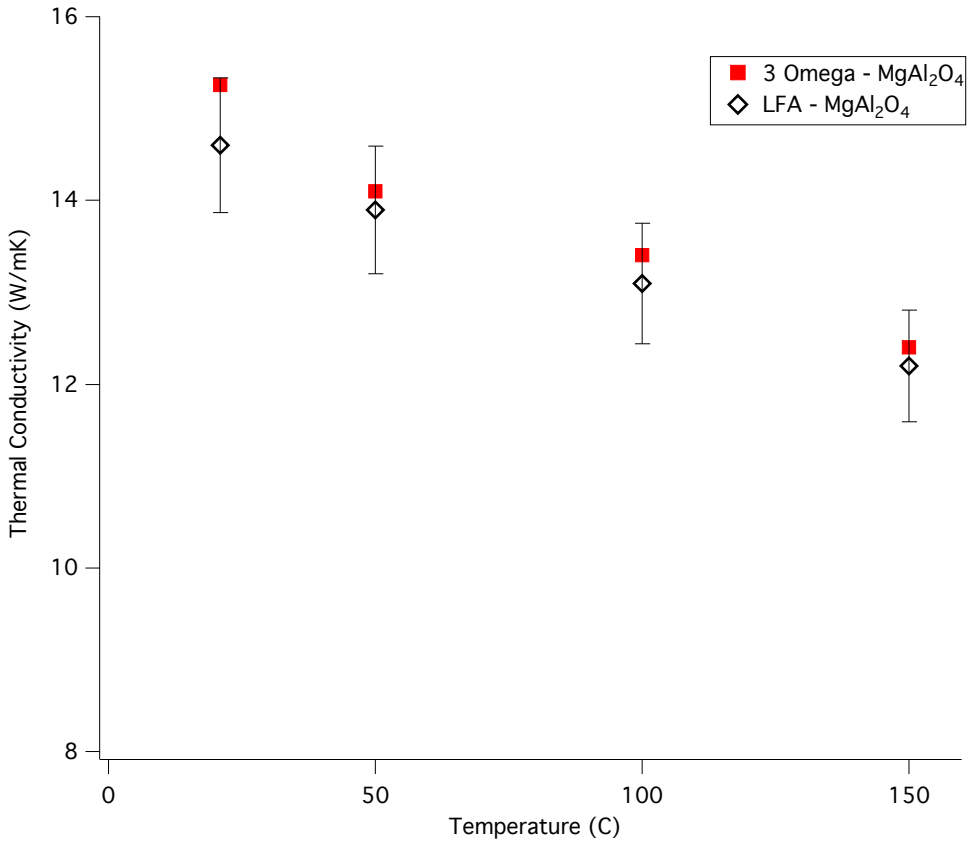

Figure 4.9 Comparison of thermal conductivity values for laser flash analysis and 3ω method for $MgAl_2O_4$ [67].

4.4.4 Comparison of 3ω method and laser flash analysis for three-phase composite

Al_2O_3 – $MgAl_2O_4$ – 8YSZ composites with 1.2 μm and 500 nm grain sizes were measured via both LFA and 3ω Method from 25 to 150 °C. From Figure 4.10, the 3ω measurements and laser flash analysis data show good agreement for both grain sizes. The associated error of LFA is ± 5% and all 3ω measurements fall within this error, with the 3ω measurements have an error of approximately ± 2%. This error is generated from the deviation between measurements on three different composite samples.

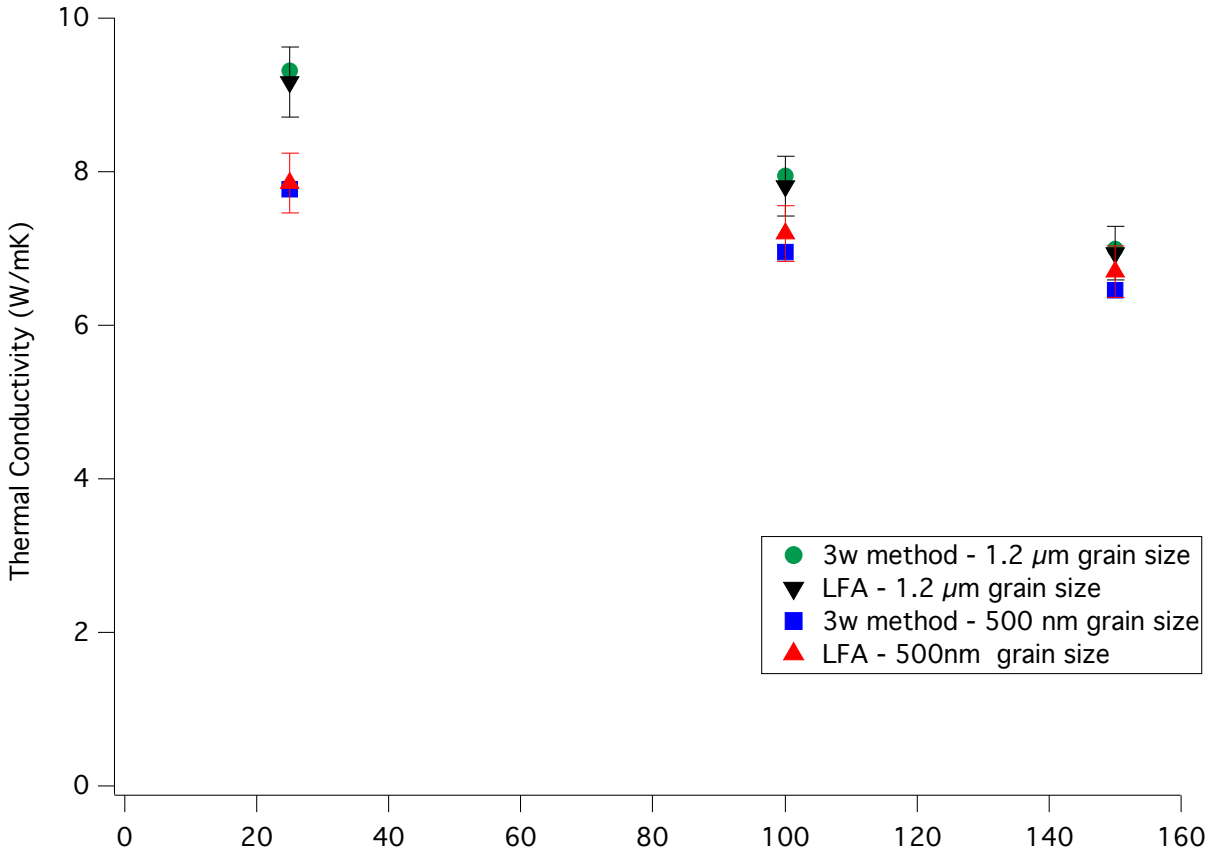

Figure 4.10 Comparison of thermal conductivity values for 1.2 μm and 500 nm grain size Al_2O_3 – $MgAl_2O_4$ – 8YSZ composites measured by laser flash analysis and 3ω Method.

Further comparison of the measurements of each method further confirm the conclusions of Chapter 4. Namely, that the higher density of grain boundaries in a 500 nm grain size composite leads to a reduction in the effective thermal conductivity of the composite when compared to 1.2 μm composites with similar composition. All four data sets are shown in Figure 4.10 and highlight the degradation due to changes in grain size and the 3ω method's ability to measure data close to the values measured by laser flash analysis. Through analysis of four distinct ceramic materials, the 3ω method accurately measured the thermal conductivity at low temperatures as validated by the corresponding laser flash analysis results and literature values. The final section of this chapter will compare and contrast the two techniques and lay groundwork for future studies that can take advantage of the 3ω Method.

4.4.5 Advantages and Disadvantages of 3ω Method and Laser Flash Analysis

At the low temperatures evaluated during this study, the 3ω method compared favorably with the more traditional laser flash analysis. The two techniques will be analyzed and suggestions will be made based on the strengths and weaknesses of both techniques. The main limitation of the 3ω method is the temperature range at which it can operate. Due to the sensitive nature of the heater line and electrode, the technique has only been used up to about 500 °C [95]. The current setup was limited to approximately 175 °C due to the material constraints imposed by the silver epoxy and solder that is used to connect the sample to the 3ω instrumentation. Utilizing materials with a higher thermal threshold can slightly increase the temperature range; however, a vacuum chamber would be necessary for measurements up to 500 °C or down to cryogenic temperatures. The current temperature range is ideal for thermoelectric material characterization. Laser flash analysis measurements can be performed in excess of 1700 °C, which is an obvious advantage for analyzing high temperature materials such as nuclear fuels or thermal barrier coatings.

An advantage of the 3ω system is the cost when compared to a typical laser flash analysis instrument; especially when considering that in order to calculate thermal conductivity using laser flash analysis, one also needs to measure thermal expansion and specific heat capacity. While only one sample is necessary for thermal conductivity measurement for 3ω, three separate measurements are necessary to generate the information necessary to calculate thermal conductivity using laser flash analysis. Ideally, the 3ω method can be used as a screening technique to quickly ascertain the thermal conductivity at low temperatures before using laser flash analysis for high temperature measurements.

4.5 Conclusions

A system for measuring the thermal conductivity of bulk ceramics via the 3ω method was constructed and validated using single-phase 8YSZ and $MgAl_2O_4$ samples. The 3ω measurements have good agreement with literature and experimental laser flash analysis values for the two single-phase values with deviations of less than 5% at the four temperatures measured (25, 50, 100, 150 °C). Composites consisting of equal phase fractions of Al_2O_3 – $MgAl_2O_4$ – 8YSZ with two distinct grain sizes were also measured using the 3ω method and compared to measurements conducted using laser flash analysis. Results show that 3ω measurement of thermal conductivity fall within the 5% error associated with laser flash analysis from 25 to 150 °C for four different systems with varying thermal conductivity making it an ideal technique for low temperature measurements. This study shows that the 3ω method is a viable technique for measuring the thermal conductivity of bulk ceramic samples at low temperatures.

4.6 Acknowledgements

Co-authors for this work include: Andrew T. Nelson and Ursula Carvajal-Nunez of Los Alamos National Laboratory, Professor Chris Dames of University of California, Berkeley, and Martha L. Mecartney of University of California, Irvine. Materials preparation, LFA measurements, and preliminary computational modeling were conducted based in part on work supported by the Department of Energy under Award Number DE-NE0000711. Final results on the 3ω Method were supported by NSF DMR 1611457. SEM and XRD work were performed at the UC Irvine Materials Research Institute (IMRI). AWT acknowledges support from UCI for a fellowship funded by the Nuclear Regulatory Commission (NRC).

Chapter 5: Thermal conductivity of UN/U_3Si_2 Composite Fuel Forms

5.1 Abstract

The thermal conductivity of novel uranium nitride (UN) and uranium silicide (U_3Si_2) composites were investigated for potential application as an accident tolerant fuel with higher uranium density than conventional uranium dioxide (UO_2) nuclear fuel. Specimens of various compositions ranging from 10 vol% to 40 vol% U_3Si_2 with balance UN were fabricated and then characterized via SEM and XRD. Microstructures from SEM images were used as the input for thermal conductivity modeling using a combination of OOF2 (Object oriented finite element analysis version 2) and MOOSE (Multiphysics object-oriented simulation environment). Single phase thermal conductivity values for each phase were used as inputs for simulations from 373 K to 1673 K. Using pure UN and U_3Si_2 values yielded MOOSE model results that were approximately 9% higher than the corresponding experimental results, determined from a combination of thermal diffusivity, specific heat capacity, and density. This deviation was attributed to an unknown U-Si-N phase with unknown thermal properties. The thermal conductivity of this phase was estimated using a Rule of Mixtures calculation and then used in subsequent models. With the addition of the third unknown phase into the MOOSE models, the experimental and simulated results for the 20, 30, and 40 vol% U_3Si_2 composites showed good agreement. Thermal conductivity of irradiated material was also estimated by assuming thermal degradation of the U_3Si_2 phase.

5.2 Introduction

After the Fukushima accident in Japan in March 2011, there has been significant interest in developing accident tolerant fuels (ATFs) to help prolong reactor operation in the event of a loss of coolant accident (LOCA) [96-99]. One of the currents thrust of the ATF program is to make intrinsically safer fuels that are still compatible with the current fleet of light water reactors. Currently, conventional nuclear fuel rod consists of UO_2 ceramic fuel pellets encapsulated in Zr alloy cladding [2]. This system has been refined over the past ~60 years of development and has been proven as reliable, sustainable, and cost-effective at a large scale. However, the current fuel system is hindered by low thermal conductivity within the fuel (specially the fissile UO_2 fuel). Another consideration during a design-basis LOCA, is the potential for significant heat generation and hydrogen gas build-up as a result of steam oxidation of the Zr alloy [3,46]. With enough heat and hydrogen gas present, there is risk of a release of nuclear material through explosion (as shown during the Fukushima accident). Therefore, it is imperative to look at fuels that not lonely exhibit higher intrinsic safety, but that also can provide more efficient operation of nuclear reactors during normal operating conditions.

Many different combinations of fuels and claddings are currently under investigation including SiC-SiC cladding and various fuels including uranium nitrides, silicides, and carbides [47, 97, 100-102]. Composite fuels are also under investigation for applications of nuclear fuel to mitigate some of the drawbacks of conventional UO_2 fuel [103:105]. The system under investigation in these studies was a composite of uranium nitride (UN) and uranium silicide (U_3Si_2) of varying compositions. One of the focuses of accident tolerant fuels is the enhanced thermal conductivity compared to conventional UO_2 at room and reactor operating temperatures. The

differences in the constituent phases of the fuel, UN and U_3Si_2, are significantly higher than UO_2 as shown in Figure 5.1 [48, 49, 64].

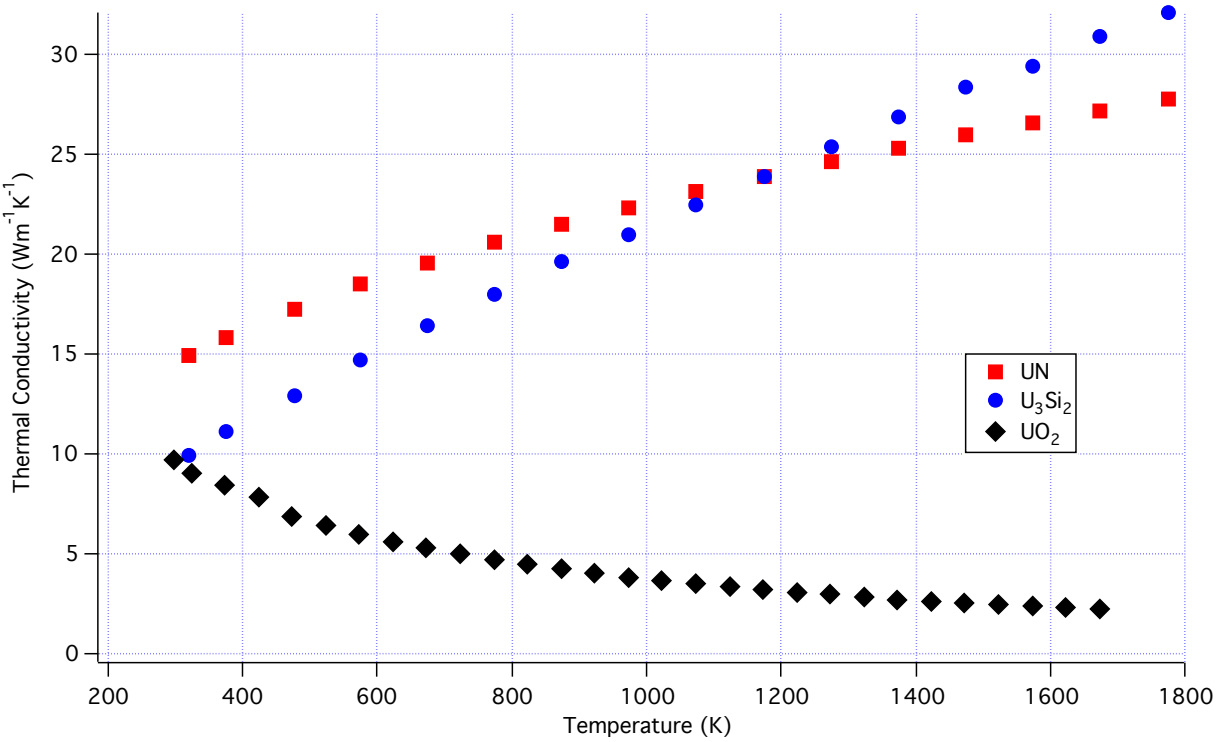

Figure 5.1 The thermal conductivity as a function of temperature for the constituent phases of the UN/U_3Si_2 composite compared to the thermal conductivity values for UO_2. Both UN and U_3Si_2 exhibit higher thermal conductivity above room temperature than UO_2 [48, 49, 64].

By utilizing a composite fuel of UN/U_3Si_2, the positives of the nitride and silicide systems can be achieved while potentially mitigating the drawbacks associated with each ceramic. As mentioned previously, both UN and U_3Si_2 have higher thermal conductivities than UO_2 and from a simple rule of mixtures calculation, it is anticipated that a composite fuel of these two materials would also have a higher effective thermal conductivity [48,49,106-108]. On top of the improved thermal properties, UN and U_3Si_2 also have higher uranium densities than conventional UO_2 [47]. However, UN undergoes pulverization under exposure to air, water, or steam. While U_3Si_2 also

oxidizes under exposure to air, water, or steam, it has more favorable performance when compared to UN [50,51,109,110]. Conventional UO_2 has favorable resistance to oxidation when compared to both UN and U_3Si_2.

5.3 Finite Element Analysis Modeling Procedures

5.3.1 OOF2 Microstructural Modeling

Micrographs of each composition were meshed using Object Oriented Finite-Element analysis version 2 (OOF2), which is developed by NIST [69]. Each phase in the micrograph was differentiated by assigning a unique color. A series of elements were overlaid on the micrograph and then repeatedly refined to increase the homogeneity of the mesh. A previous study determined that refining the homogeneity of a mesh beyond 97% resulted in thermal conductivity deviations of less than 5% [111]. In this study, all meshes were refined to a minimum of 99.5% homogeneity to ensure a high density of nodes at the phase interfaces and to minimize deviations during thermal analysis. An example of meshing for 30% U3Si2-UN SEM micrographs is shown Figure 5.2 (a-d) where the blue-colored phase is U_3Si_2 and the red-colored phase is UN.

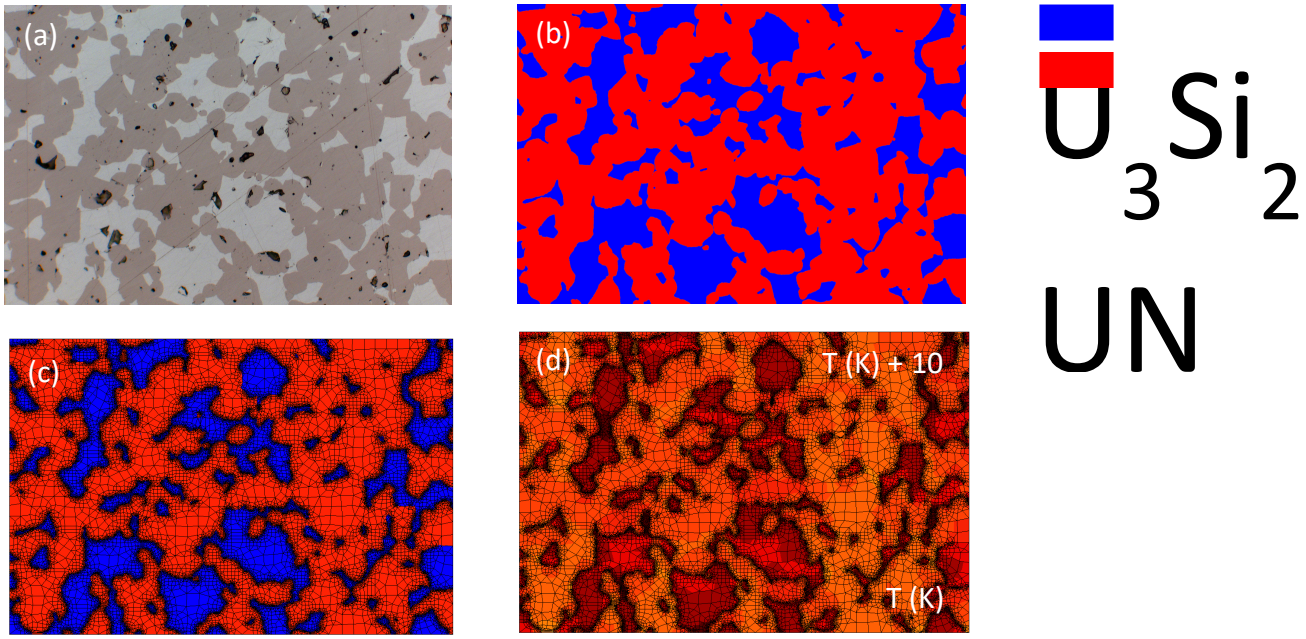

Figure 5.2 (a) An optical micrograph showing the two distinct phases of the composite. The light phase indicates the U_3Si_2 phase, the dark grey phase shows the UN phase, and the darkest region indicates porosity or grain pull out. **(b)** The colorized microstructure shows the composition without the porosity allowing for a simpler mesh to be applied. **(c)** The mesh showing the presence of many nodes at the interfaces between phases to capture the change in thermal conductivity. **(d)** A 10 K temperature gradient was applied from the top to bottom on the mesh. The thermal map shows regions of high thermal flux (indicated by the lighter color) allowing for a visualization of pathways of higher thermal transport.

5.3.2 MOOSE Thermal Conductivity Modeling

Meshes refined via OOF2 were imported into the Multiphysics object-oriented simulation environment (MOOSE) framework for thermal conductivity modeling. The MOOSE framework is an open-source framework developed by Idaho National Laboratory [55]. The 2D effective thermal conductivity of each microstructures was calculated by assigning each unique phase the thermal conductivity of that individual phase in a manner similar to Teague et al. [111], which was adapted from Millett et al. [112]. Thermal conductivity values for the UN and U_3Si_2 phases were taken from the literature [48,49,64]. For each microstructure, a constant temperature was assigned to the bottom boundary of the image, and a heat flux was assigned to the top boundary of the image to simulate a temperature drop of approximately 10 K for all simulations at all temperatures, shown in Figure 5.2 (d). The sides of the microstructure were kept adiabatic. The effective thermal conductivity (k_{eff}) was solved using the equations outlined by Teague et al. [111]. Five different microstructures were used for each composition and the variability between microstructures of the same composition was below 2%.

5.4 Results and Discussion

5.4.1 Comparison of Experimental and Modeled Results

Experimental measurements were performed on four different UN-U_3Si_2 compositions ranging from 10 vol% to 40 vol% U_3Si_2 with the remainder being UN to measure the temperature dependent thermal conductivity. As discussed previously in more detail, the thermal conductivity was calculated from a combination of laser flash analysis, dilatometry, and the Neumann-Kopp relation [113] to determine the thermal diffusivity, thermal expansion, and specific heat capacity, respectively. To confirm the experimental thermal conductivities, finite element modeling using the MOOSE framework was employed. Figure 5.3 (a-d) displays example microstructures taken using optical microscopy for each of the four compositions under investigation, where the dark grey phase is UN, the lightest phase is U_3Si_2, and porosity is the darkest black phase. Five to six microstructures were simulated using MOOSE to determine the effective thermal conductivity of the composite. Porosity for each microstructure was corrected to 100% theoretical density using the following equation:

$$\kappa_{TD} = \kappa\left[1 - 3/2\left(1 - \frac{\rho_0}{\rho_{TD}}\right)\right]^{-1} \quad (5\text{-}1)$$

Where κ_{TD} is the thermal conductivity at 100% theoretical density, κ is the thermal conductivity at some density ρ_0, and ρ_{TD} is the theoretical density.

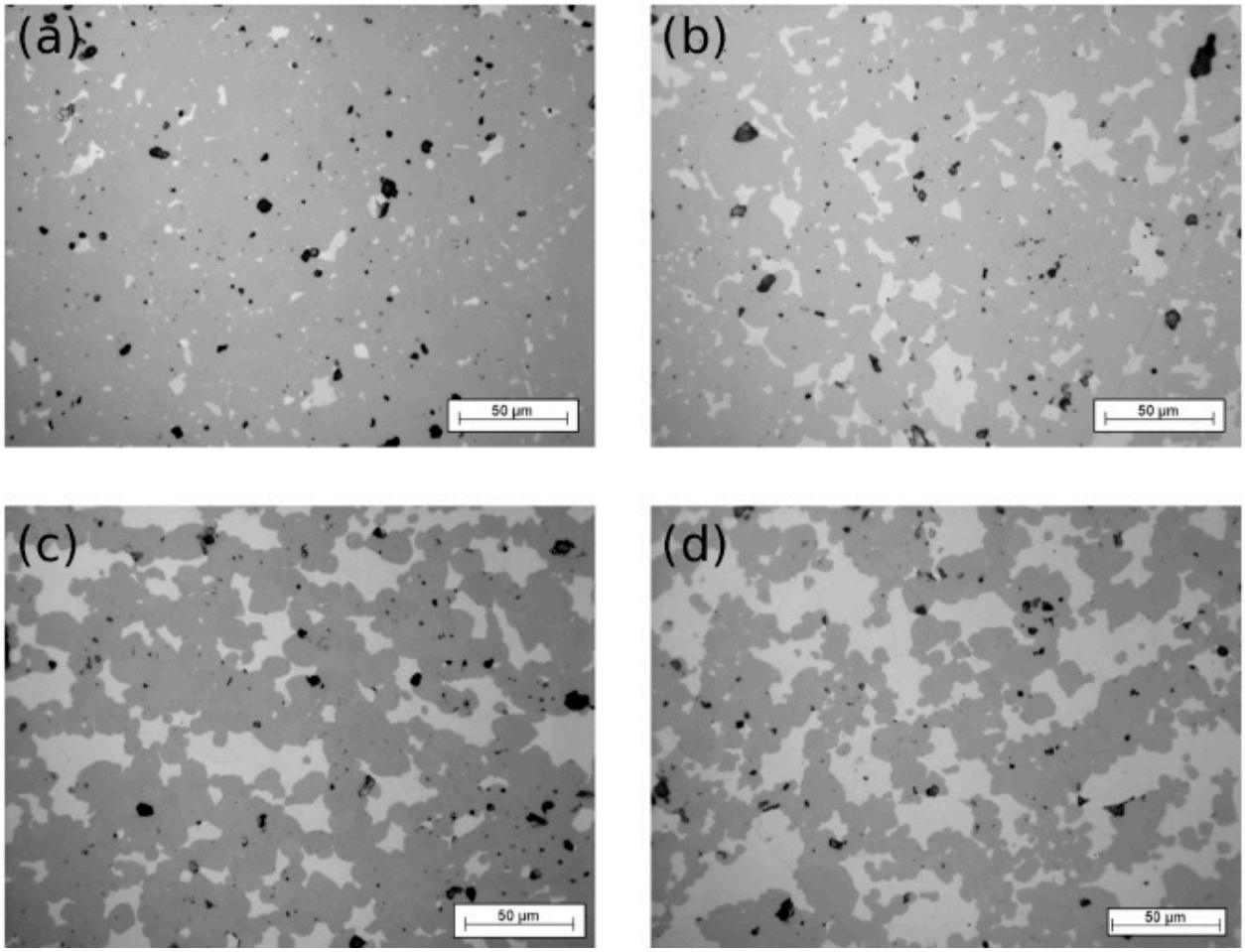

Figure 5.3 Micrographs showing the variations in compositions between samples **(a)** 10 vol% U_3Si_2 **(b)** 20 vol% U_3Si_2 **(c)** 30 vol% U_3Si_2 **(d)** 40 vol% U_3Si_2.

Upon comparing the experimental results and MOOSE results, the simulated thermal conductivities deviated by approximately 8% for the 20 vol% - 40 vol% compositions and by about 15% for the 10 vol% composition at all temperatures (Figure 5.4 (a-d)). While the Kapitza resistance of composites has been extensively discussed (see Chapter 3), it is not likely to have any influence since the grain size of the composite is on the order of 10 μm, well outside the range where Kapitza related effects are expected.

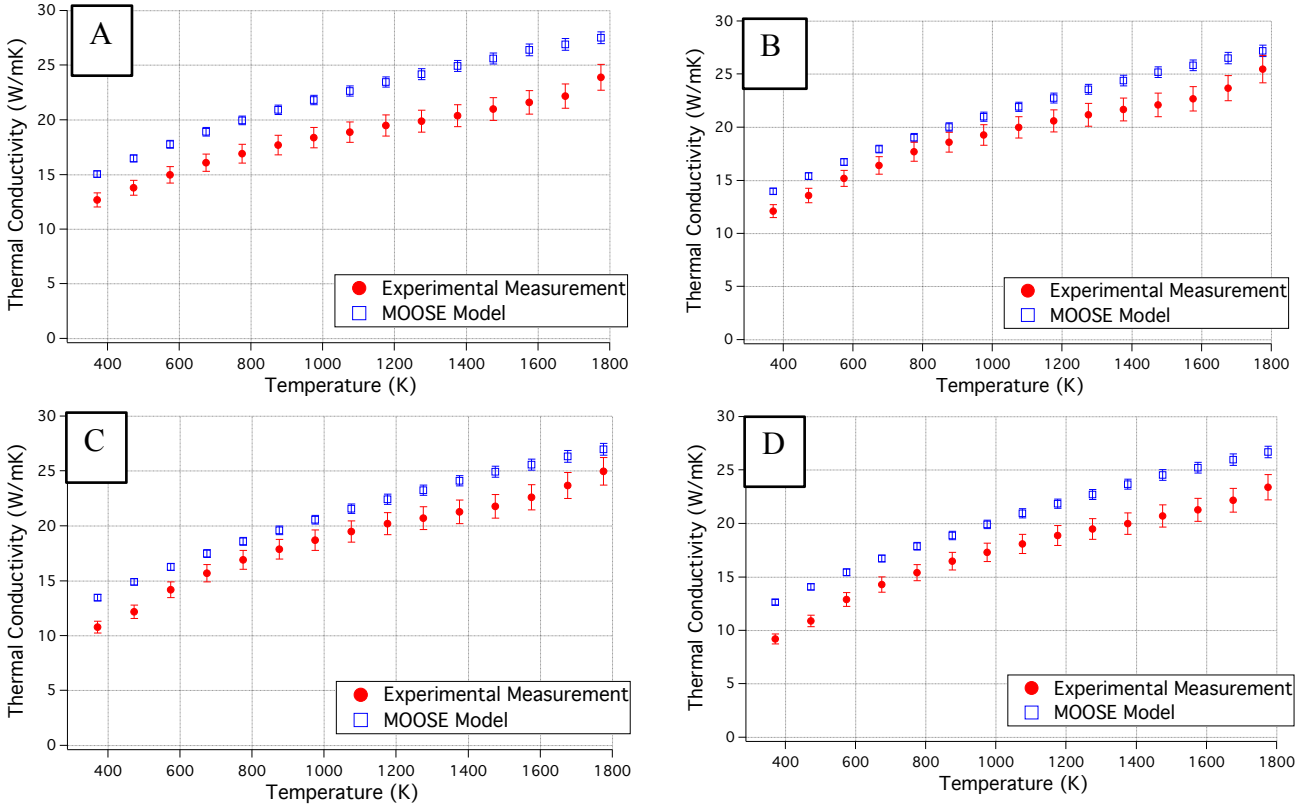

Figure 5.4 (a) Discrepancies between experimental values and modeled values for the 10 vol% U_3Si_2 specimens. **(b)** Discrepancies between experimental values and modeled values for the 20 vol% U_3Si_2 specimens. **(c)** Discrepancies between experimental values and modeled values for the 30 vol% U_3Si_2 specimens. **(d)** Discrepancies between experimental values and modeled values for the 40 vol% U_3Si_2 specimens.

Further characterization was performed on all compositions to better understand why the disagreement between experiment and model existed. First, x-ray diffraction (XRD) was used to look at the composition of each phase. Interestingly, the XRD pattern revealed an additional third phase that did not match any known cards within the ICDD database (Figure 5.5). The data clearly showed the UN and U_3Si_2 phases as well as the third phase (given in blue in Figure 5.5) present in compositions 20 vol% - 40 vol% of U_3Si_2. Initially, it was hypothesized that the unknown phase was U_3Si_5. However, the fit was not exact and a preliminary MOOSE model incorporating a silicide phase with a thermal conductivity equal to a rule of mixtures calculation of 70% U_3Si_2 and 30% U_3Si_5 did not significantly lower the discrepancy between experimental and modeled values at high temperatures. An example of this model for the 40 vol% U_3Si_2 with an assumed amount of U_3Si_5 present in the silicide is shown in Figure 5.6. The mismatch between experiment and model does not significantly improve across the entire range of temperatures.

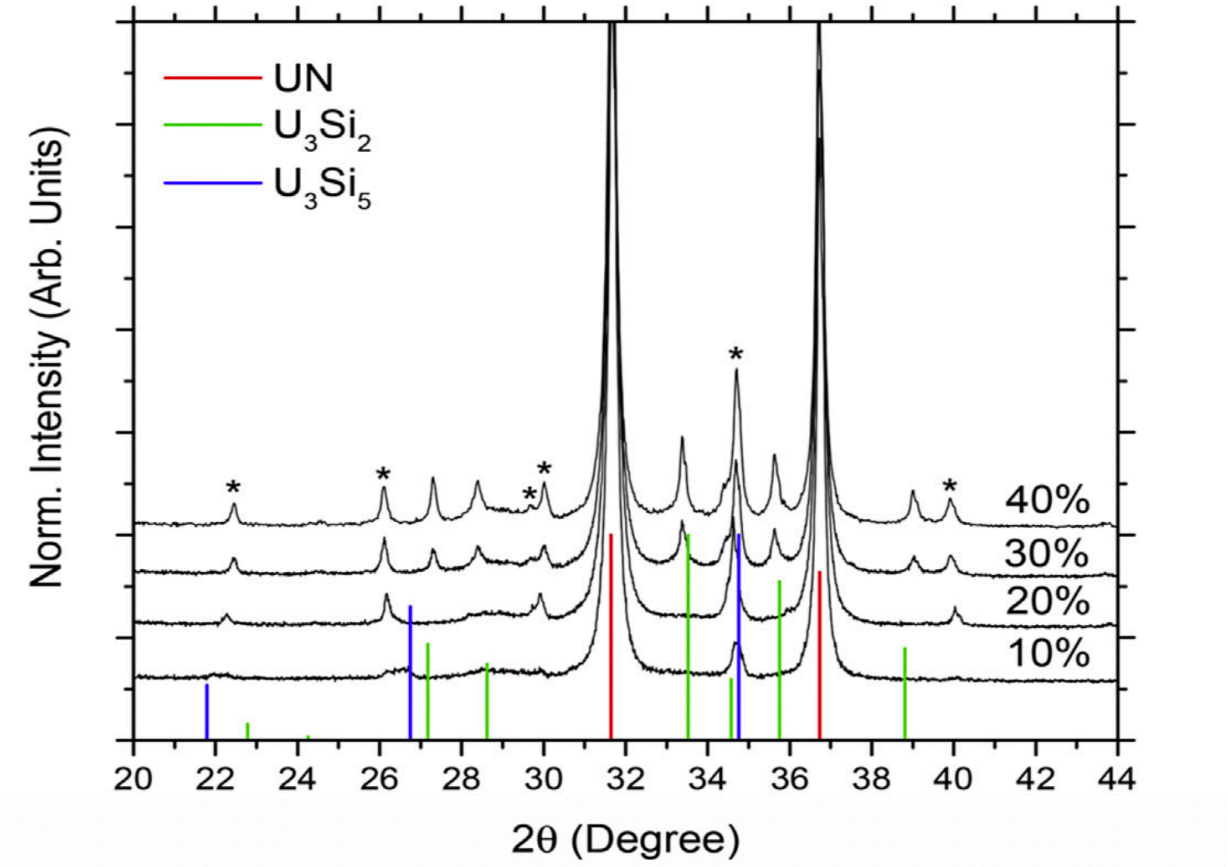

Figure 5.5 XRD pattern for the various compositions showing the peak positions of the UN and U_3Si_2 phases. Additionally, there are unknown phases marked by asterisks that do not correspond to U_3Si_5 or any other phases within the ICDD database for powder diffraction files.

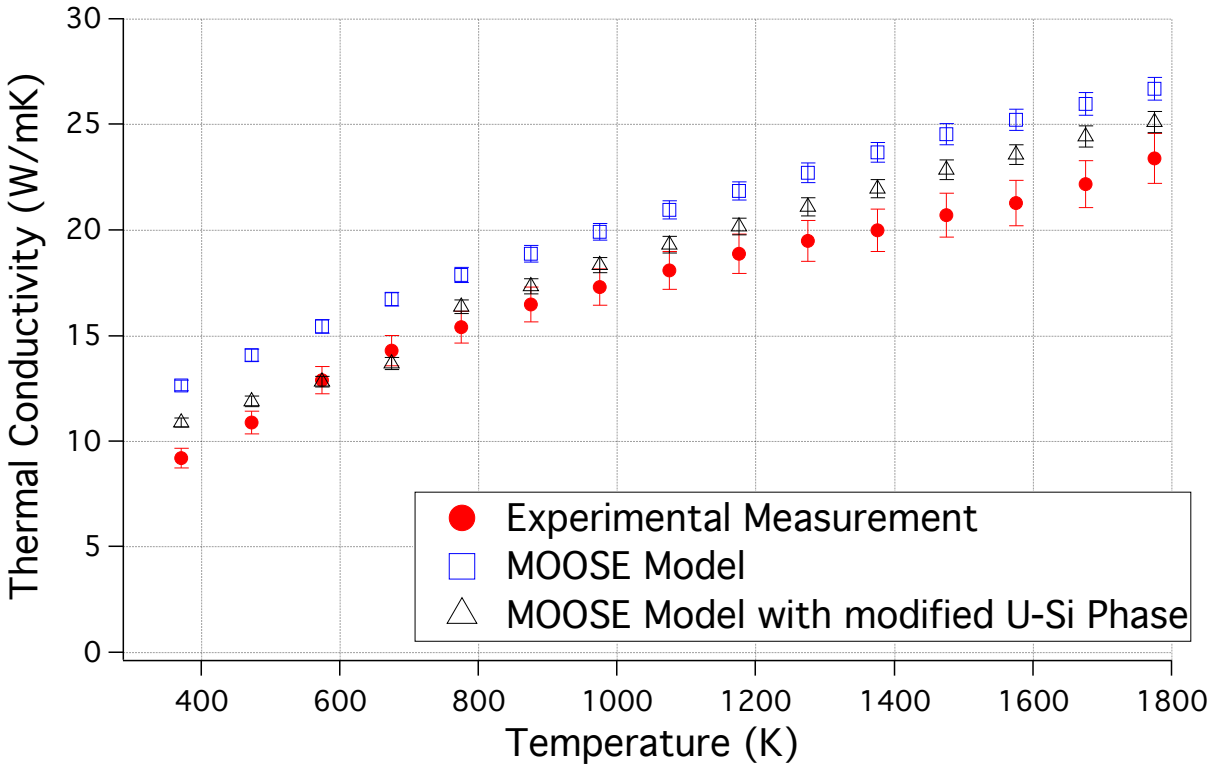

Figure 5.6 Comparison of experimental measurements and modeled data for the 40 vol% U_3Si_2 composites. The mismatch between model and experiment is improved at low temperatures when the thermal conductivity input of the silicide phase is adjusted to include 30% U_3Si_5 / 70% U_3Si_2. However, significant deviations still exist at high temperatures (>1200 K).

5.4.2 Influence of Unknown U-N-Si Phase on Effective Thermal Conductivity

To better understand the unknown phase, energy dispersive x-ray spectroscopy showed that the unknown phase contained uranium, nitrogen, and silicide forming a phase with unknown stoichiometry (nominally referred to as U-Si-N). Using UN and U_3Si_2 thermal conductivity input values in the MOOSE code, which assumed that the U-Si-N phase had the same thermal conductivity as U_3Si_2, yielded values that overpredicted the 20 vol% - 40 vol% experimental dataset values by an average of 8% over the entire temperature range and the 10 vol% values by an average of 15%. It is assumed that the reason a poor fit was provided with these inputs was a

result of the U-Si-N phase. Given that the U-Si-N phase has unknown properties, an attempt was made to calculate the thermal conductivity of that phase using a rule of mixtures approach with the inputs of phase pure UN and U_3Si_2 along with the phase fractions in Table 5.1 using the 30 and 40 vol% datasets.

Table 5.1 Percentages of phases as determined by EDS for the various compositions fabricated in this study. Errors for the given phase percentages are +/- 1%.

Composition	**UN**	**U_3Si_2**	**U-Si-N**	**U_3Si_5**
10%U_3Si_2-UN	92	0	6	2
20%U_3Si_2-UN	75	0	22	3
30%U_3Si_2-UN	70	14	15	0.4
40%U_3Si_2-UN	61	21	18	0.5

The results for the U-Si-N phase thermal conductivity are shown in Figure 5.7. At lower temperatures, the U-Si-N phase thermal conductivity drops on cooling below T = 773 K. This could be a result of the microcrack formation that was observed in the microstructure therefore dropping the thermal conductivity of the composite. The calculated U-Si-N phase thermal conductivity values were applied to newly meshed three-phase microstructures for the 10 vol% - 40 vol% compositions (blue phase in Figure 5.8 (b)).

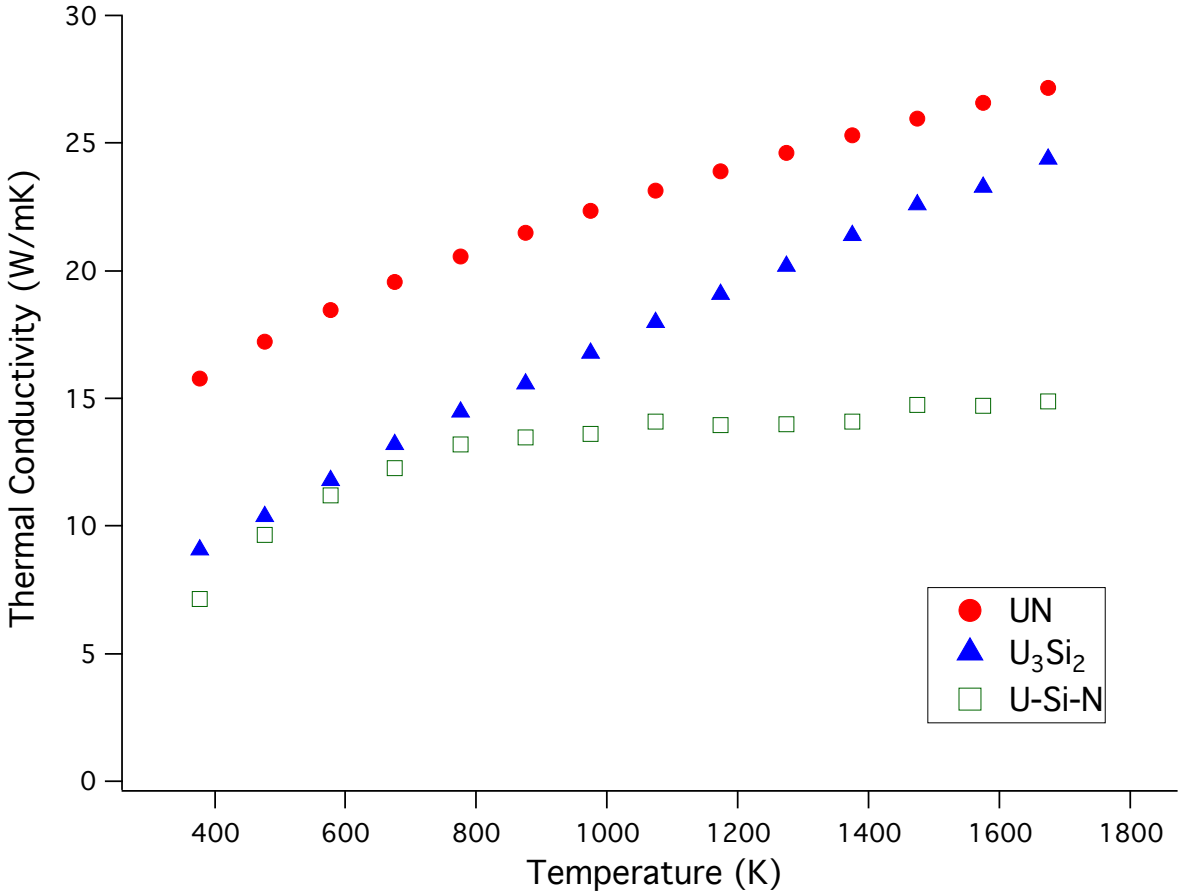

Figure 5.7 The thermal conductivity of the unknown U-Si-N phase was calculated using the rule of mixtures and is shown in orange squares. The thermal conductivity values are lower than both of the constituent phases, especially at high temperatures.

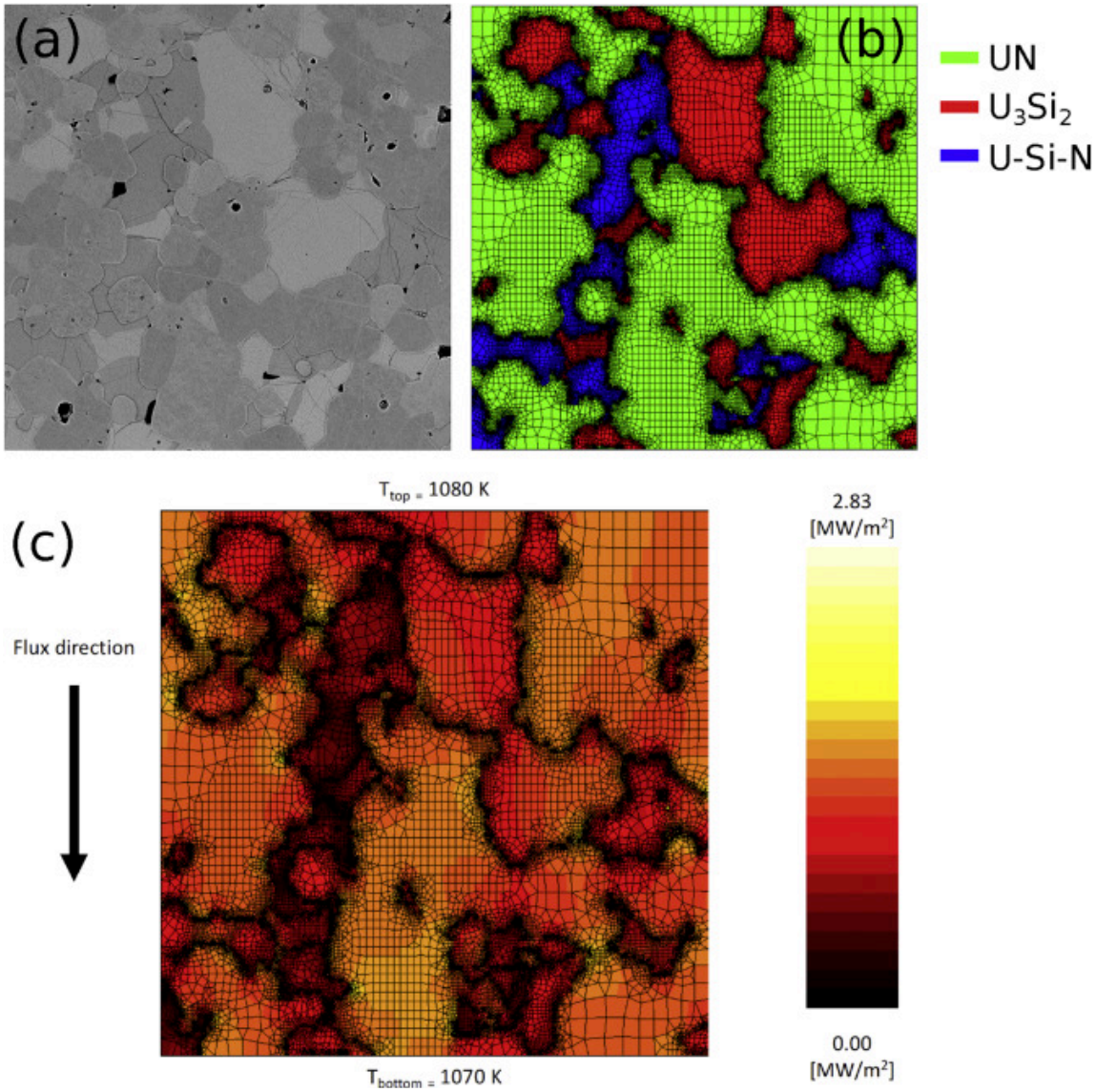

Figure 5.8 An overview of the OOF2 meshing process for the now three-phase composite. **(a)** The SEM micrograph shows a third phase. **(b)** This third phase is easier to see once the micrograph has been colorized and meshed. Again, there is a high density of nodes at the boundaries between phases. **(c)** The thermal map shows the regions of high thermal transport through the microstructure.

The MOOSE simulations were run again with the updated phase fractions and thermal conductivity inputs and compared to the experimental values (Figure 5.9). Now, there is high agreement between the modeled and experimental results for the 20 - 40 vol% U_3Si_2 specimens. A discrepancy on the order of 10% is observed between the MOOSE model and the experimentally determined values for the 10 vol% specimen, which is not understood.

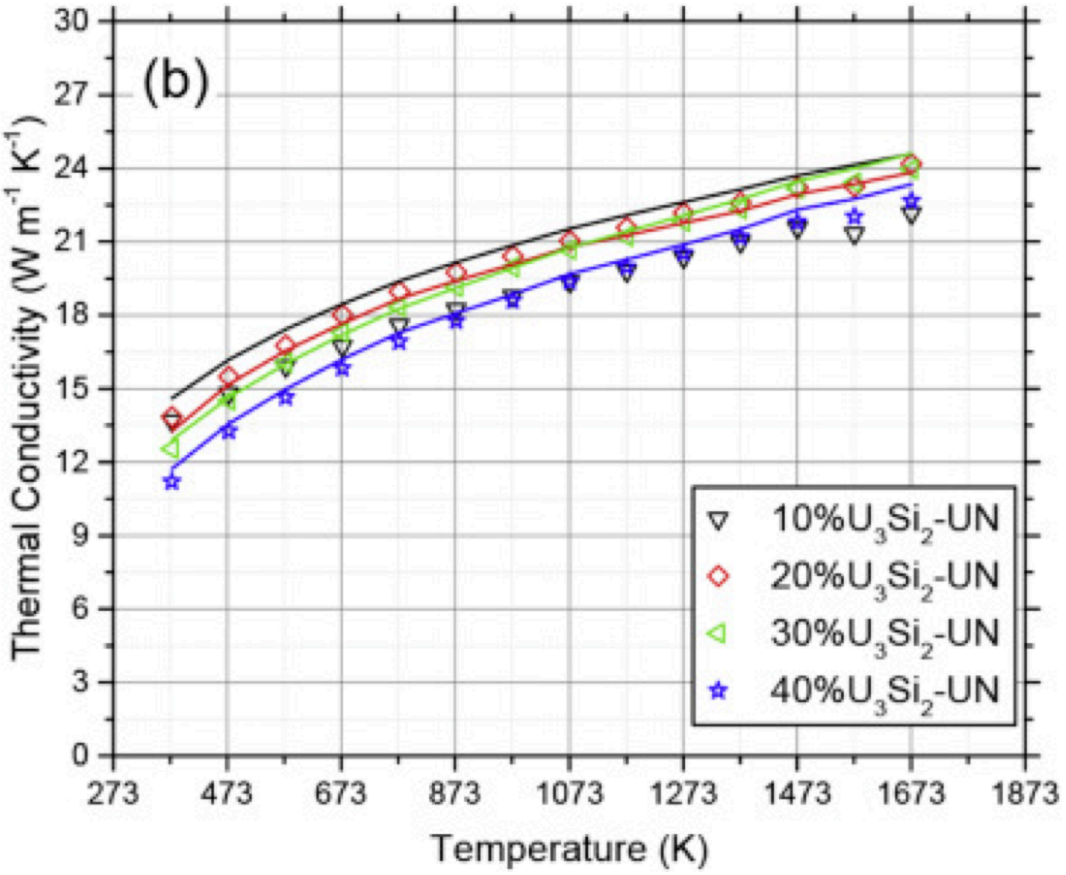

Figure 5.9 Modeled thermal conductivity results now have high agreement with the experimental results (within the error of experimental measurements), except the 10 vol % samples which for an unknown reason has much higher deviation than the 20, 30, and 40 vol% samples.

5.4.3 Estimation of Irradiation Effects on Composite Thermal Conductivity

The impact of irradiation and burnup on the composite fuel properties is difficult to predict given the large uncertainties in irradiation behavior for both UN and U_3Si_2 under typical LWR conditions. Thermal conductivity measurements have been conducted on irradiated UN in a BREST-OD fast reactor up to a burnup of 150 GWd/ton [114]. The irradiated thermal conductivity values are 20-25% lower when compared against the unirradiated values from Hayes et al. [115]. Thermal conductivity data for irradiated U_3Si_2 is not available in the literature, but limited studies of the impact of radiation damage on thermal conductivity of intermetallics have shown an impact [116].

Despite the lack of experimental data for these systems, the MOOSE model developed in this study can be used to explore possible effects of irradiation on the UN - U_3Si_2 composite. The MOOSE simulation was repeated where the thermal conductivity of the U-Si phases was fractionally reduced from 100% theoretical thermal conductivity down to 25% theoretical thermal conductivity. At present only a single example evolution is explored to demonstrate the utility of this approach, but more involved investigations (e.g. microstructural evolution, addition of fission product phases, etc.) could be incorporated in more sophisticated models to aid interpretation and focus post irradiation examination of novel fuel forms. The results of this analysis are shown in Figure 5.10, where 100% represents the thermal conductivity of unirradiated U_3Si_2. It is known under high burnup conditions that U_3Si_2 forms uniformly distributed voids within the microstructure. At lower dose rates, more representative of an LWR, U_3Si_2 amorphizes at temperatures below 523 K but recrystallizes at higher temperatures [117,118]. The data plotted in Fig. 10 provides an approximation for the thermal conductivity of a UN - U_3Si_2 composite following degradation in the thermal conductivity of the U_3Si_2 phase. These results, although

speculative given the qualifiers above, illustrate the ability of a high thermal conductivity phase such as UN to limit the effect of thermal conductivity degradation that may occur in a secondary phase within a composite fuel architecture.

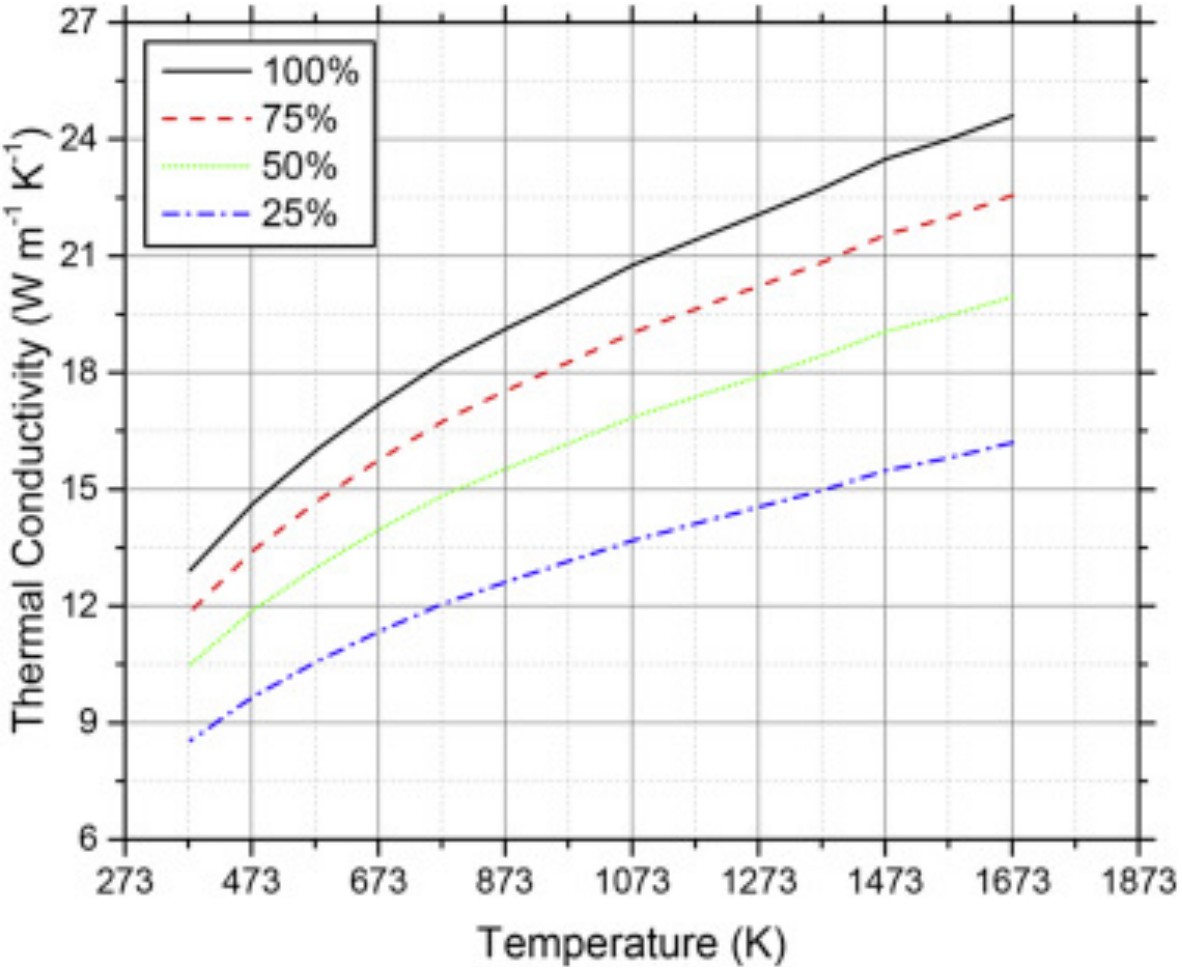

Figure 5.10 Modeled thermal conductivity values showing the potential degradation of the thermal conductivity in the silicide phase. The predictive nature of MOOSE makes these models possible. Even if there is 100% degradation of thermal conductivity in the U_3Si_2 phase, the thermal conductivity is still higher than UO_2 from room temperature to elevated temperatures.

5.5 Conclusions

Composite UN-U_3Si_2 samples were fabricated and the temperature dependent thermal conductivity was calculated for compositions ranging from 10 to 40% U_3Si_2. During this process, an unknown U-Si-N ternary phase formed. The thermal conductivity of this unknown U-Si-N phase was estimated using the Rule of Mixtures. With the inclusion of the ternary phase, modeling of the complex microstructure within the MOOSE framework provided a good fit to the experimental thermal conductivity values. The thermal conductivity of the irradiated composite was also estimated within the MOOSE framework by assuming fractional degradation of U_3Si_2 phase in accordance with previous literature studies.

5.6 Acknowledgements

Co-authors of this work include: Joshua T. White and Andrew T. Nelson of Los Alamos National Laboratory. This research was also partially supported using funding received from the DOE Office of Nuclear Energy's Nuclear University Programs under contract DE-NE0000711.

Chapter 6: Continuum Scale Modeling of Hyperstoichiometric UO_{2+x}

6.1 Abstract

In this chapter, various microstructures of UO_{2+x} and U_4O_9 were evolved using the phase field model by supplying initial temperatures and oxygen concentrations to the simulation field. By minimizing the free energy within the phase field model, various microstructures with differing phase fractions and compositions were evolved to equilibrium. Anisotropy within the U_4O_9 domains was considered during the evolutions. Microstructures were evolved correctly according to the phase field diagram for uranium and oxygen for degrees of stoichiometry ranging from x=0 to x=0.25 (where x=0 represents UO_2 and x=0.25 represents U_4O_9) and temperatures from 25 to 1400 °C. The thermal conductivity of the microstructures was then simulated and analyzed for both single-phase systems or binary-phase composites depending on the location prescribed by the phase diagram. Thermal conductivity in UO_{2+x} decreases with increasing hyperstoichiometry and increasing amount of U_4O_9. Correctly modeling the anisotropy of U_4O_9 domains increased the accuracy of the model when comparing the results to data available in the literature.

6.2 Introduction

Nuclear energy is an important source of electricity accounting for approximately 20% of this country's total electricity [119]. Conventional UO_2 nuclear fuel is susceptible to oxidation via the formation of hyperstoichiometric uranium dioxide (UO_{2+x}) when exposed to air or high temperature water vapor in the event of a cladding breach during operation or storage [85]. Below 1130°C intermediate oxides U_4O_9 and U_3O_7 form; which degrades the thermal conductivity of the fuel. Understanding how the thermal conductivity degrades as a function of oxygen content and phase fractions is an important engineering problem for future fuel performance codes for safe and efficient reactor operation.

Previous studies, have focused on understanding the uranium – oxygen phase field (given below in Figure 6.1) [120]. The modeling in this chapter focused on the region in Fig. 1 from O/U ratio 2.00 to 2.25 from room temperature to elevated temperatures above 1200°C. Previous studies have experimentally investigated the temperature dependent thermal conductivity of this system and will be used to validate the models [85, 121, 122]. As the degree of hyperstoichiometry increases (increasing O/U ratio), the thermal conductivity of the fuel decreases towards a minimum value which is representative of the U_4O_9 phase. Above O/U > 2.15 or x > 0.15, the thermal conductivity reaches this plateau. The thermal conductivity as a function of hyperstoichiometry showing this phenomenon is shown in Figure 6.2 [121].

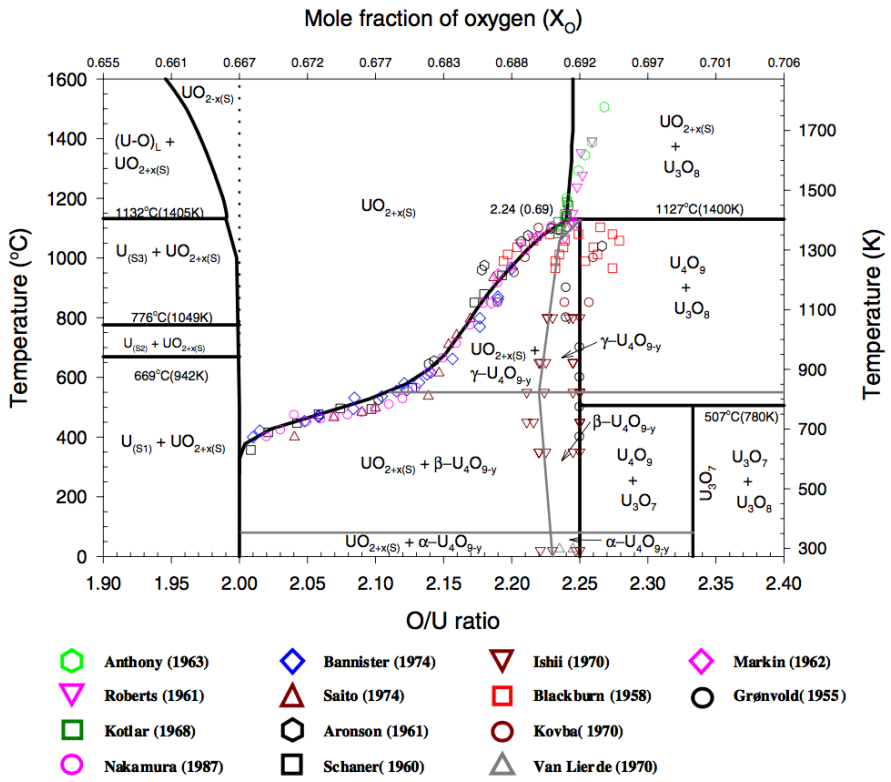

Figure 6.1 Uranium – Oxygen phase field diagram showing the various oxides that can form as a function of temperature and oxygen stoichiometry [120].

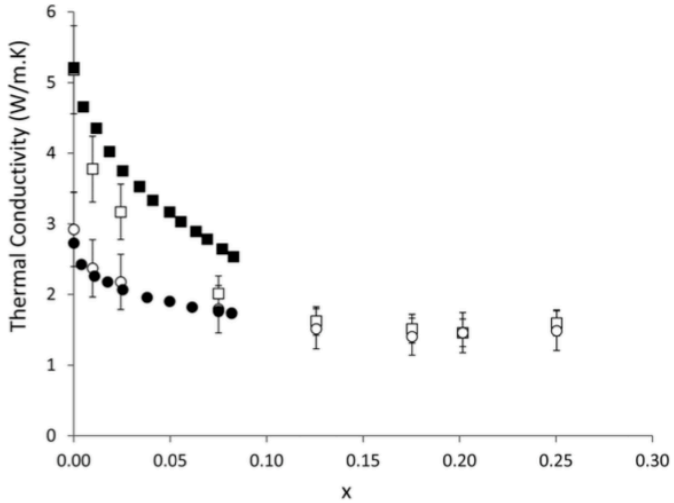

Figure 6.2 Thermal conductivity as a function of increasing oxygen hyperstoichiometry from Watanabe *et al.* [121].

In this study, the phase field model was utilized to evolve binary-phase microstructures of UO_{2+x} and U_4O_9 at various oxygen concentrations and temperatures. Depending on the concentration and temperature, either a single-phase UO_{2+x} region was evolved or a dual phase region of UO_{2+x} and U_4O_9 was evolved in agreement with the phase diagram. The thermal conductivity of each microstructure was simulated using as a function of temperature of the two-phase regions. The thermal conductivity as a function of temperature will be modeled across these temperatures using data from experimental measurements.

The following sections will review phase field modeling and the necessary equations for evolving a microstructure. Then, the procedure for importing the evolved microstructure into the solver, refining the mesh, and applying boundary conditions and initial conditions will be discussed. Then, the resulting microstructures and thermal conductivity simulation results will be analyzed and compared to current experimental measurements for various oxygen concentration and temperatures.

6.3 Experimental Procedures

A phase field model was developed to evolve dual phase microstructures of UO_{2+x} and U_4O_9 at various oxygen/uranium ratios (degree of hyperstoichiometry) and temperatures. At equilibrium, the thermal conductivity of the binary phase field will be simulated as a function of temperature using data from experiment and molecular dynamics (MD) simulations as inputs. Detailed steps to develop the model are outlined.

6.3.1 Phase Field Modeling in MOOSE

The phase field model was used to evolve a dual phase field of UO_{2+x} and U_4O_{9-y} in the MOOSE (Multiphysics Object Oriented Simulation Environment) framework distributed by Idaho National Laboratory [70]. The phase field approach is a powerful method for modeling microstructure evolution. The phase field model has been comprehensively outlined and reviewed previously and has been used to solve a multitude of problems [123, 124].

Within phase field modeling, microstructural features are described using continuous variables. The evolution of these continuous variables is a function of the Gibbs free energy and can be defined as a system of PDEs (and can therefore be solved using the finite element model). Phase field modeling captures microstructure evolution through two sets of continuous variables: conserved and non-conserved. For this model, the evolution of the oxygen concentration (c), which is the conserved parameter, was defined using the Cahn-Hilliard equation:

$$\frac{dc}{dt} = \nabla \cdot \mathrm{M} \nabla \frac{dF}{dc} \tag{6-1}$$

The evolution of the phase field variable (η), which is the non-conserved variable, was given by the Allen-Cahn Equation:

$$\frac{\delta \eta_j}{\delta t} = -L \frac{\delta F}{\delta \eta_j} \tag{6-2}$$

Where, M and L were the conserved mobility and order parameter mobility respectively. The Cahn-Hilliard and Allen-Cahn were used as inputs for the overall Gibbs Free Energy (F) equation, given below:

$$F = \int_V [f_0(c,\eta,T^*) + \frac{\epsilon}{2}(\nabla c)^2 + \frac{\kappa}{2}(\nabla \eta)^2]dr \tag{6-3}$$

The major components of the Gibbs Free Energy functional are f_0 (homogeneous free energy density), ∇c (concentration gradient as given by the Cahn-Hilliard Equation), and $\nabla \eta$ (phase field gradient as given by the Allen-Cahn Equation). The other variables, ε and κ, represent the gradient interfacial energy term and the gradient energy term respectively.

The homogeneous free energy density was given by the equation:

$$f_0(c,\eta,T^*) = f_p(c,\eta,T^*) + wg(\eta) \tag{6-4}$$

Where $f_p(c,\eta,t)$ is the interpolation function at describes the transition between multiple phases and $wg(\eta)$ is the double well potential describing the energy minima in each phase with w being a constant representing the energy barrier height.

The double well potential was given by the equation:

$$g(\eta) = \eta^2(1-\eta^2) \tag{6-5}$$

Here, as well as in subsequent equations, $\eta = 0$ represented the UO_2 domains and $\eta = 1$ specified the U_4O_9 domains. Any value of η between 0 and 1 represented an interface between the two specific phases.

The interpolation function allowed for the combining of the homogenous free energy expressions for the coexisting phases via the following equation:

$$f_p(c,\eta,T^*) = \big(1 - p(\eta)\big) f^{\alpha}(c,T^*) + p(\eta) f^{\beta}(c,T^*) \tag{6-6}$$

The free energy functionals of the two phases ($\alpha = UO_2$ and $\beta = U_4O_9$) were discreetly described by their oxygen concentrations and a certain temperature range. From the uranium-oxygen phase diagram, U_4O_9 is assigned a degree of hyperstoichiometry (x) of 0.25 with UO_{2+x} assigned a degree of hyperstoichiometry between 0 and 0.25 depending on the temperature used to evolve the microstructure. The two phases were each given a free energy expression to guide the evolution. The U_4O_9 phase had a constant equation at all temperatures where the free energy function for UO_{2+x} was assigned various functions depending on the temperature, as shown in Table 6.1. The phase diagram in Figure 1 was simplified to accurately capture the two phases using an approximation. CALPHAD equations are difficult to implement in phase field models and were not considered in this derivation [125].

Table 6.1 Free energy functions for the dual phase field. These functions are derived from the uranium-oxygen phase diagram and are expressed as oxygen concentration as a function of temperature.

Phase	Free Energy Function	Concentration as a Function of Temperature	Temperature Range
UO_{2+x}	$F(UO_{2+x}) = [c - c(T)]^2$	$c(T) = 0$ $c(T) = (T-600)/(2188.8)$ $c(T) = (T-195.05)/(5020.6)$	< 600 K 600 – 913 K 913 - 1400 K
U_4O_9	$F(U_4O_9) = [c - c(T)]^2$	$c(T) = 0.25$	< 1400 K

From the interpolation function, there was also a weighting function p(η) that explicitly describes the minima for when η = 0 corresponding to UO_2 and η = 1 corresponding to U_4O_9:

$$p(\eta) = \eta^3(6\eta^2 - 15\eta + 10) \tag{6-7}$$

With these equations specified for a specific temperature and the corresponding free energy functional describing the oxygen concentration in each phase, the partial differential equations were solved in the weak form in preparation for Finite Element Analysis discretization and were then solved using the MOOSE framework. The weak form solution to the Cahn-Hilliard equation was expressed as:

$$\left(\frac{dc_i}{dt}, \phi_m\right) = -\left(\kappa_i \nabla^2 c_i, \nabla \cdot (M_i \nabla \phi_m)\right) - \left(M_i \nabla \left(\frac{df_{loc}}{dc_i} + \frac{dE_d}{dc_i}\right), \nabla \phi_m\right) + \langle M_i \nabla(\kappa_i \nabla^2 c_i) \cdot \vec{n}, \phi_m \rangle -$$

$$\langle M_i \nabla \left(\frac{df_{loc}}{dc_i} + \frac{dE_d}{dc_i}\right) \cdot \vec{n}, \phi_m \rangle + \langle \kappa_i \nabla^2 c_i, M_i \nabla \cdot \vec{n} \rangle \tag{6-8}$$

And the weak form solution of the Allen-Cahn equation was given as:

$$\left(\frac{d\eta_j}{dt}, \phi_m\right) = -L\left(\kappa_j \nabla \eta_j, \nabla \phi_m\right) - L\left(\frac{df_{loc}}{d\eta_j} + \frac{dE_d}{d\eta_j}, \nabla \phi_m\right) + L\langle \kappa_j \nabla \eta_j \cdot \vec{n}, \phi_m \rangle \tag{6-9}$$

The outlined equations above were necessary to begin modeling phase field evolution within the MOOSE framework.

6.3.2 Implementing anisotropy in phase field models

Scanning electron microscopy (SEM) images revealed U_4O_9 to have an anisotropic shape which was replicated in the phase field model [126, 127]. An example of the anisotropy in the U_4O_9 phase is shown in Figure 6.3. Anisotropy was introduced based on the equations from Loginova *et al.* [128] for a Widmanstatten microstructure, which was modified from the work of Kobayashi [129]. This was accomplished within the two-dimensional Allen-Cahn equation by modifying the interfacial energy term, ε.

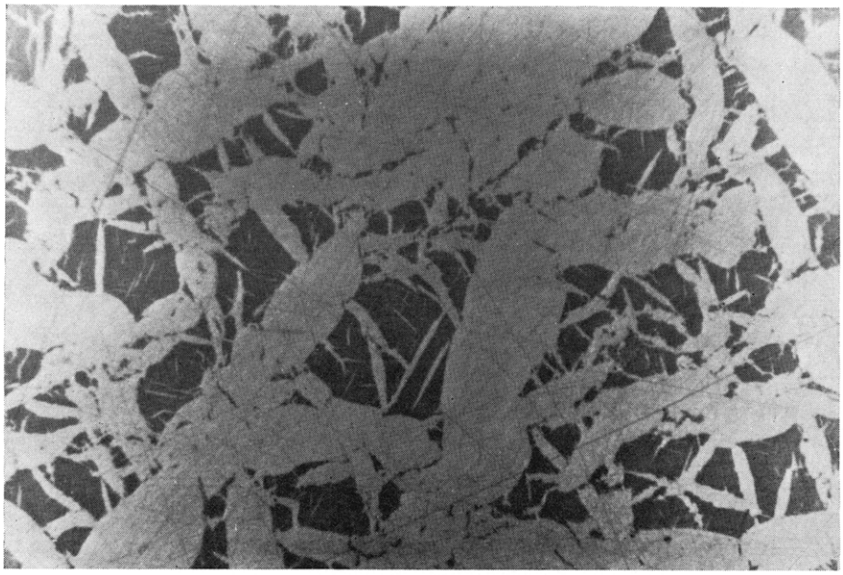

Figure 6.3 SEM micrograph showing UO_2 (dark) and U_4O_9 light [126].

The traditional Allen-Cahn equation (Equation 6-2) was modified to include the interfacial energy term in two-dimensions by the equation:

$$\frac{\delta \eta_j}{\delta t} = -L\left[\left(\frac{\delta f_{loc}(\eta,c)}{\delta \eta}\right) - \frac{\delta}{\delta x}\left(\varepsilon \frac{\delta \varepsilon}{\delta \eta}\frac{\delta \eta}{\delta y}\right) + \frac{\delta}{\delta y}\left(\varepsilon \frac{\delta \varepsilon}{\delta \eta}\frac{\delta \eta}{\delta x}\right) + \nabla \cdot (\varepsilon^2 \nabla \eta)\right] \quad (6\text{-}10)$$

Where ε was expressed as a function of surface energy by the equation:

$$\varepsilon = \bar{\varepsilon}\sigma(\theta) \quad (6\text{-}11)$$

Where:

$$\sigma(\theta) = \frac{1}{1+\delta}(1 + \delta|\cos(\theta - \theta_0)|) \quad (6\text{-}12)$$

This extended formulation allowed for the evolution of Widmanstatten microstructures that accurately captured the anisotropic morphology of the U_4O_9 domains.

6.3.3 Thermal Conductivity Simulations on Evolved Microstructures in MOOSE

Thermal conductivity data from experimental measurements used as inputs for the individual phases in the dual phase field. In both cases, the data for U_4O_9 was assumed constant for all temperatures [85, 130]. The thermal conductivity for the UO_{2+x} phase was input as a function of temperature and oxygen concentration based on the equilibrium oxygen concentration during the phase field evolution.

To determine the thermal conductivity input for the UO_{2+x} phase, the following equation was solved for both experimental laser flash analysis values.

$$\lambda = \frac{1}{A+(B\cdot T)+\left(C\cdot c(T)\right)} \tag{6-13}$$

where the variables *A*, *B*, and *C* depend on the experimental data, *T* represents temperature in Kelvin and *c(T)* represents the concentration of interstitial oxygen in UO_{2+x} as a function of temperature (Table 6.2)

Table 6.2 Parameters for solving the thermal conductivity of UO_{2+x}

	A	B	C
Experimental	0.0311	0.000265123	2.911372

Within the MOOSE framework, evolved microstructures at equilibrium were meshed and assigned thermal conductivity values based on the phase designated at the specific node (given by oxygen concentration). The effective thermal conductivity across the bulk was calculated as a function of oxygen concentration and the phase field variable. A constant temperature was applied to the left-hand side of the microstructure, with a heat flux assigned to the right-hand side of the microstructure to yield a temperature difference of approximately 10 K across the microstructure. The top and bottom boundaries were held adiabatic.

The thermal conductivity at each quadrature point on the mesh was calculated using the following equation:

$$k = ((1-\eta)*k_{UO2})+((\eta)*k_{U4O9} \quad (6\text{-}14)$$

The effective conductivity of the bulk was then calculated using the equation:

$$k_{eff} = -\frac{q_t}{\frac{T_l - T_r}{l}} \quad (6\text{-}15)$$

The effective thermal conductivities of the simulations were then compared to the experimental values to validate the phase field model.

6.4 Results and Discussion

Microstructures were evolved as a function of interstitial oxygen concentration at various temperatures to plot out the phase diagram space. Depending on the concentration and temperature, either a single-phase UO_{2+x} region was evolved or a dual-phase region of UO_{2+x} and U_4O_9 was evolved in agreement with the phase diagram. The thermal conductivity of each microstructure was simulated using as a function of temperature of the two-phase regions.

6.4.1 Thermal Conductivity Results of UO_{2+x} as a Function of Hyperstoichiometry and Temperature

At various temperatures and interstitial oxygen concentrations between 0 and 0.25, a dual-phase region of UO_2 and U_4O_9 exists and can be described using the free energy functions in Table 6.1. Various temperatures and oxygen concentrations varying from x = 0 and x = 0.25 (with UO_2 represented as x = 0 and U_4O_9 represented as x = 0.25) were evolved within the MOOSE framework to equilibrium. An example microstructure from 400 K with an oxygen concentration of x = 0.2 is shown in Fig. 6.4, with the blue region corresponding the UO_{2+x} matrix and the red region corresponding to the U_4O_9 domains with an oxygen concentration of 0.25.

Fig 6.4 Phase field model for a UO_2 – U_4O_9 microstructure evolved at 400 K and an initial concentration of oxygen of 0.20. (b) Meshed microstructures showing refinement of the quadrature points on the mesh with a high concentration of points capturing the interface between the two phases.

Increasing nonstoichiometry in the UO_{2+x} phase leads to decreased thermal conductivity, which agrees with experimental data (Fig 6.5). This trend validates experimental measurements found in the literature and shows the ability of the phase field model to develop accurate microstructures based on oxygen concentration and composition [85].

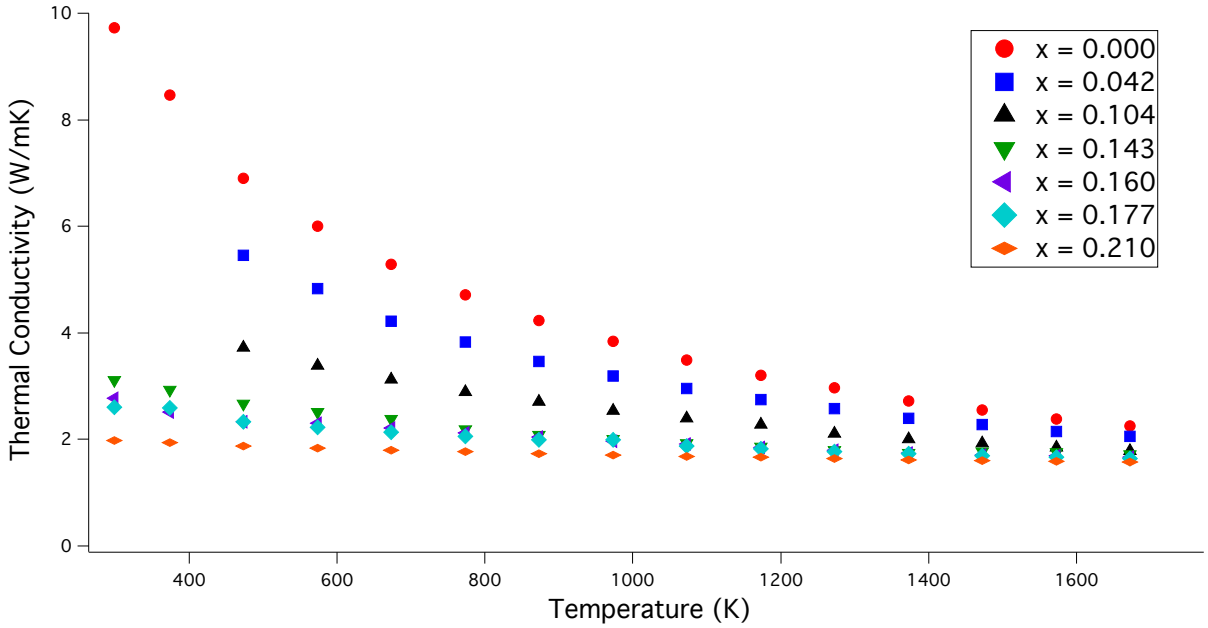

Figure 6.5 Thermal conductivity as a function of temperature and oxygen concentration.

Another important aspect of the phase field model is the ability to modify the shape of the U_4O_9 domains. The anisotropy of the U_4O_9 domains has a direct effect on the thermal conductivity of the bulk and therefore, needs to be coupled with accurate phase fractions. An example of this phenomenon is given in Figure 6.6 where two temperature dependent thermal conductivity data sets from simulated microstructures are compared to experimental measurements at the same oxygen composition (x= 0.143) and temperatures. One simulated set has isotropic U_4O_9 domains and the other has anisotropic U_4O_9 domains. The anisotropic data set has much better agreement with the experimental data. Understanding the relationship between shape and thermal

conductivity is important for describing more complex systems with multiple cations (e.g. mixed oxide fuels of relevance to faster reactor applications) in the phase field.

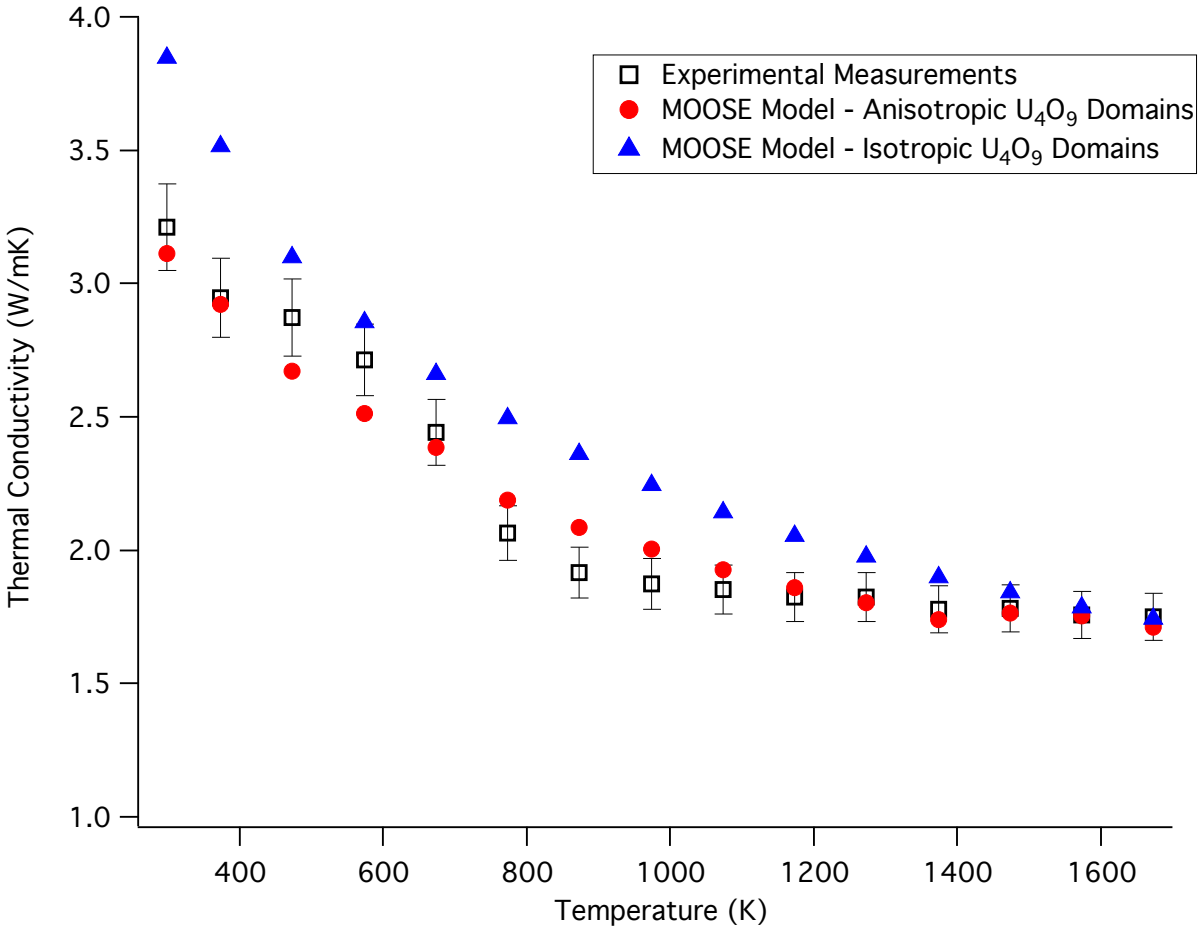

Figure 6.6 Simulated and experimental thermal conductivity values as a function of temperature in a binary phase UO_{2+x} and U_4O_9 composition when x = 0.143. Simulated microstructures with anisotropic U_4O_9 domains yield higher agreement with experimental measurements [85].

6.5 Conclusions

The phase field model was used to evolve microstructures of UO_{2+x} and U_4O_9 composites at various temperatures and oxygen concentrations. The microstructures follow the compositions that were expected from the uranium – oxygen phase diagram and were evolved to equilibrium. The thermal conductivity across the phase field microstructures was also simulated as a function of temperature and hyperstoichiometry. Increasing hyperstoichiometry in the UO_{2+x} phase lead to a reduction in thermal conductivity when compared to UO_2. Also, the shape of the domains influenced the effective thermal conductivity. Microstructures with anisotropic U_4O_9 domains (as seen in the limited micrographs in the literature) agreed more favorably with experimental measurements than domains with isotropic domains. The phase field model is an appropriate methodology for generating microstructures for thermal conductivity simulations in the uranium – oxygen system.

6.6 Acknowledgements

Co-authors of this work include: David A. Andersson and Andrew T. Nelson of Los Alamos National Laboratory. This research was supported using funding received from the DOE Office of Nuclear Energy's Nuclear University Programs under contract DE-NE0000711.

Chapter 7: Conclusions and Future Work

7.1 Summary and Conclusions

The objective of this research was to explore the temperature dependent thermal conductivity and grain size dependent of ceramic composites for potential nuclear fuels. By combining experimental and computational techniques, the thermal conductivity of several ceramic composites for nuclear fuel applications was determined and analyzed. A brief summary of the significant results of each study are presented below.

In Chapter 3, three-phase composites of Al_2O_3, $MgAl_2O_4$, and 8YSZ with two distinct grain sizes were fabricated and characterized by their thermal conductivity. The fine grain composite had a 10% reduction in thermal conductivity at 25 °C when compared to the large grain composite with similar composition. This difference was attributed to the Kapitza resistance and calculated to be 8.4×10^{-9} - 9.8×10^{-9} m^2K/W. These values represent averages, however, there seems to be a strong temperature dependence in the Kapitza resistance with the highest Kapitza resistance for both composites at 25 °C. These Kapitza resistance values are also higher than single phase YSZ as reported in literature. With the calculated Kapitza resistance, thermal conductivity as a function of grain size was modeled. The thermal conductivity of the composite begins to reduce due to the Kapitza resistance at grain sizes below 1 μm, whereas in single-phase materials, this phenomenon is usually not seen until nanocrystalline grain sizes (< 500 nm).

In Chapter 4, thermal conductivity results from the 3ω method were compared to thermal conductivity measurements done by laser flash analysis, a more traditional technique. Initially, the thermal conductivity of 8YSZ and $MgAl_2O_4$ samples were measured and found to have high agreement between the two techniques. From there, three-phase composites were measured by both 3ω method and laser flash analysis. The results from 3ω method fall within the associated

errors of the laser flash analysis technique. For the first time, the 3ω method was validated as a suitable technique for measuring the thermal conductivity of bulk ceramic samples with varying thermal conductivities and microstructures at low temperatures. This technique can be used as a low temperature screening technique before higher temperature measurements with laser flash analysis.

In Chapter 5, accident tolerant fuel forms of various compositions of UN/U_3Si_2 were synthesized and characterized by their thermal properties. After initial discrepancies between experimental measurements and finite element modeling, it was discovered that a third phase was present within the composite with unknown stoichiometry and thermal properties. The thermal conductivity of this third phase, designated U-Si-N, was estimated using the Rule of Mixtures and then incorporated into a more sophisticated, three-phase finite element model. The 20 – 40 vol% U_3Si_2 composites have high agreement with experimental measurements and were able to validate the laser flash analysis results. The 10 vol% U_3Si_2 still had deviations between experiment and model; the reason is unknown. Finally, the irradiated thermal conductivity of the composite was estimated. It was shown that even under assumed extreme thermal conductivity degradations, the effective thermal conductivity of the UN/U_3Si_2 composites was higher than irradiated UO_2 at temperatures from 25 °C to 1500 °C.

In Chapter 6, phase field modeling was utilized to evolve microstructures of UO_{2+x} and U_4O_9 in accordance with the uranium-oxygen phase diagram. The phase field models accurately described the microstructure based on oxygen concentration, temperature, and anisotropy within the discreet domains. Once microstructures of various degrees of hyperstoichiometry were evolved to equilibrium, they were measured and assigned thermal conductivity values based on the oxygen concentration. The evolved microstructures accurately followed what was expected based on the

phase diagram for various oxygen concentrations and temperatures. The thermal conductivity of each microstructure was simulated as a function of hyperstoichiometry and temperature. Increasing oxygen hyperstoichiometry resulted in decreased thermal conductivity compared to stoichiometric UO_2. Also, the shape of the U_4O_9 domains effected the overall thermal conductivity. Anisotropic domains more accurately modeled the thermal conductivity of the composite compared to isotropic domains, indicating that the shape of grains is critical when modeling the thermal conductivity of microstructures.

7.2 Future Work

Recommended future work to continue the discussed research:

Chapter 3

- Determine the Kapitza resistance of the constituent two-phase components of the three-phase composites.
- Using the Kapitza resistances of the single-, two-, and three-phase composites, create a model to accurately calculate the Kapitza resistance of a composite with three or more phases.

Chapter 4

- Continue benchmarking the thermal conductivity of ceramic materials using the 3ω method.
- Utilize the heater line/electrode geometry to measure the thermal conductivity across a boundary in a bicrystal or material with very large grains for a "direct" measurement of the Kapitza resistance.

Chapter 5

- Fabricate microstructures so the U_3Si_2 phase coats or encapsulates the UN phase instead of percolating throughout to better protect against oxidizing environments.
- Analyze how the thermal conductivity will change with the adjusted microstructure and then perform radial thermal conductivity models instead of models in Cartesian coordinates.

Chapter 6

- Add plutonium to the phase field model and evolve microstructures to see how the model behaves
- Use the ternary phase field models to simulate the thermal conductivity as various compositions of uranium and plutonium oxides, oxygen concentrations, and temperatures for application towards mixed-oxide (MOX) fuels.

References

[1] W. D. Kingery, "Introduction to ceramics," pp. 781 p. Wiley: New York, (1960).

[2] W.E. Lee, M. Gilbert, S.T. Murphy, and R.W. Grimes, "Opportunities for Advanced Ceramics and Composites in the Nuclear Sector," *J. Am. Ceram. Soc.*, **96** [7] 2005–2030 (2013).

[3] S.J. Zinkle and G.S. Was, "Materials challenges in nuclear energy," *Acta Materialia*, **61** [3] 735–758 (2013).

[4] D. Olander, "Nuclear fuels – Present and future," *Journal of Nuclear Materials*, **389** [1] 1–22 (2009).

[5] D. Men, M.K. Patel, I.O. Usov, M. Toiammou, I. Monnet, J.C. Pivin, J.R. Porter, and M.L. Mecartney, "Radiation damage in multiphase ceramics," *Journal of Nuclear Materials*, **443** [1] 120–127 (2013).

[6] J.P. Angle, A.T. Nelson, D. Men, and M.L. Mecartney, "Thermal measurements and computational simulations of three-phase (CeO2–MgAl2O4–CeMgAl11O19) and four-phase (3Y-TZP–Al2O3–MgAl2O4–LaPO4) composites as surrogate inert matrix nuclear fuel," *Journal of Nuclear Materials*, **454** [1–3] 69–76 (2014).

[7] J.T. White, A.W. Travis, J.T. Dunwoody, and A.T. Nelson, "Fabrication and thermophysical property characterization of UN/U3Si2 composite fuel forms," *Journal of Nuclear Materials*, **495** 463–474 (2017).

[8] M.R. Winter and D.R. Clarke, "Oxide Materials with Low Thermal Conductivity," *Journal of the American Ceramic Society*, **90** [2] 533–540 (2007).

[9] A.M. Limarga, S. Shian, R.M. Leckie, C.G. Levi, and D.R. Clarke, "Thermal conductivity of single- and multi-phase compositions in the ZrO2–Y2O3–Ta2O5 system," *Journal of the European Ceramic Society*, **34** [12] 3085–3094 (2014).

[10] I.W. Donald and P.W. McMillan, "Ceramic-matrix composites," *J Mater Sci*, **11** [5] 949–972 (1976).

[11] E. Antolini and E.R. Gonzalez, "Ceramic materials as supports for low-temperature fuel cell catalysts," *Solid State Ion.*, **180** [9–10] 746–763 (2009).

[12] Y. Wei, W. Yang, J. Caro, and H. Wang, "Dense ceramic oxygen permeable membranes and catalytic membrane reactors," *Chem. Eng. J.*, **220** 185–203 (2013).

[13] C. Sun, J. Liu, Y. Gong, D.P. Wilkinson, and J. Zhang, "Recent advances in all-solid-state rechargeable lithium batteries," *Nano Energy*, **33** 363–386 (2017).

[14] N.V. Long, Y. Yang, C.M. Thi, N.V. Minh, Y. Cao, and M. Nogami, "The development of mixture, alloy, and core-shell nanocatalysts with nanomaterial supports for energy conversion in low-temperature fuel cells," *Nano Energy*, **2** [5] 636–676 (2013).

[15] L.S. Walker, V.R. Marotto, M.A. Rafiee, N. Koratkar, and E.L. Corral, "Toughening in Graphene Ceramic Composites," *ACS Nano*, **5** [4] 3182–3190 (2011).

[16] H. Tang and H.A. Sodano, "Ultra High Energy Density Nanocomposite Capacitors with Fast Discharge Using Ba0.2Sr0.8TiO3 Nanowires," *Nano Lett.*, **13** [4] 1373–1379 (2013).

[17] Z. Shao, W. Zhou, and Z. Zhu, "Advanced synthesis of materials for intermediate-temperature solid oxide fuel cells," *Prog. Mater. Sci.*, **57** [4] 804–874 (2012).

[18] D. Men and M.L. Mecartney, "Superplasticity and machinability in a four-phase ceramic," *Materials Research Bulletin*, **47** [8] 1925–1931 (2012).

[19] J.B. Davis, D.B. Marshall, R.M. Housley, and P.E.D. Morgan, "Machinable ceramics containing rare-earth phosphates," *J. Am. Ceram. Soc.*, **81** [8] 2169–2175 (1998).

[20] S.M. Best, A.E. Porter, E.S. Thian, and J. Huang, "Bioceramics: Past, present and for the future," *J. Eur. Ceram. Soc.*, **28** [7] 1319–1327 (2008).

[21] J. Chevalier and L. Gremillard, "Ceramics for medical applications: A picture for the next 20 years," *J. Eur. Ceram. Soc.*, **29** [7] 1245–1255 (2009).

[22] F. Bouville, E. Maire, S. Meille, B. Van de Moortele, A.J. Stevenson, and S. Deville, "Strong, tough and stiff bioinspired ceramics from brittle constituents," *Nat. Mater.*, **13** [5] 508–514 (2014).

[23] L.-B. Mao, H.-L. Gao, H.-B. Yao, L. Liu, H. Colfen, G. Liu, S.-M. Chen, S.-K. Li, *et al.*, "Synthetic nacre by predesigned matrix-directed mineralization," *Science*, **354** [6308] 107–110 (2016).

[24] D.B. Marshall, P.E.D. Morgan, and R.M. Housley, "Debonding in Multilayered Composites of Zirconia and LaPO4," *Journal of the American Ceramic Society*, **80** [7] 1677–1683 (1997).

[25] P. Morgan and D. Marshall, "Ceramic Composites of Monazite and Alumina," *J. Am. Ceram. Soc.*, **78** [6] 1553–1563 (1995).

[26] F.P. Incropera & D.P. DeWitt, (2002). *Fundamentals of heat and mass transfer*. New York: J. Wiley.

[27] D.G. Cahill, W.K. Ford, K.E. Goodson, G.D. Mahan, A. Majumdar, H.J. Maris, R. Merlin, and S.R. Phillpot, "Nanoscale thermal transport," *Journal of Applied Physics*, **93** [2] 793–818 (2003).

[28] D.G. Cahill, P.V. Braun, G. Chen, D.R. Clarke, S. Fan, K.E. Goodson, P. Keblinski, W.P. King, *et al.*, "Nanoscale thermal transport. II. 2003–2012," *Applied Physics Reviews*, **1** [1] 011305 (2014).

[29] P.L. Kapitza, "Heat Transfer and Superfluidity of Helium II," *Phys. Rev.*, **60** [4] 354–355 (1941).

[30] Y. Wang, K. Fujinami, R. Zhang, C. Wan, N. Wang, Y. Ba, and K. Koumoto, "Interfacial Thermal Resistance and Thermal Conductivity in Nanograined $SrTiO_3$," *Appl. Phys. Express*, **3** [3] 31101 (2010).

[31] E.T. Swartz and R.O. Pohl, "Thermal boundary resistance," *Rev. Mod. Phys.*, **61** [3] 605–668 (1989).

[32] D.S. Smith, S. Fayette, S. Grandjean, C. Martin, R. Telle, and T. Tonnessen, "Thermal Resistance of Grain Boundaries in Alumina Ceramics and Refractories," *Journal of the American Ceramic Society*, **86** [1] 105–111 (2003).

[33] A.M. Limarga and D.R. Clarke, "The grain size and temperature dependence of the thermal conductivity of polycrystalline, tetragonal yttria-stabilized zirconia," *Applied Physics Letters*, **98** [21] 211906 (2011).

[34] F. Yang, X. Zhao, and P. Xiao, "Thermal conductivities of YSZ/Al_2O_3 composites," *Journal of the European Ceramic Society*, **30** [15] 3111–3116 (2010).

[35] H. Wang, Y. Xu, M. Shimono, Y. Tanaka, and M. Yamazaki, "Computation of Interfacial Thermal Resistance by Phonon Diffuse Mismatch Model," *Materials Transactions*, **48** [9] 2349–2352 (2007).

[36] C.-W. Nan, R. Birringer, D.R. Clarke, and H. Gleiter, "Effective thermal conductivity of particulate composites with interfacial thermal resistance," *Journal of Applied Physics*, **81** [10] 6692–6699 (1997).

[37] P.C. Millett, M.R. Tonks, K. Chockalingam, Y. Zhang, and S.B. Biner, "Three dimensional calculations of the effective Kapitza resistance of UO2 grain boundaries containing intergranular bubbles," *Journal of Nuclear Materials*, **439** [1–3] 117–122 (2013).

[38] H.S. Yang, G.R. Bai, L.J. Thompson, and J.A. Eastman, "Interfacial thermal resistance in nanocrystalline yttria-stabilized zirconia," *Acta Materialia*, **50** [9] 2309–2317 (2002).

[39] J.-P. Crocombette and L. Gelebart, "Multiscale modeling of the thermal conductivity of polycrystalline silicon carbide," *Journal of Applied Physics*, **106** [8] 083520 (2009).

[40] D.P.H. Hasselman, K.Y. Donaldson, J. Liu, L.J. Gauckler, and P.D. Ownby, "Thermal Conductivity of a Particulate-Diamond-Reinforced Cordierite Matrix Composite," *Journal of the American Ceramic Society*, **77** [7] 1757–1760 (1994).

[41] M. Pokharel, H. Zhao, Z. Ren, and C. Opeil, "Grain boundary Kapitza resistance analysis of nanostructured FeSb2," *International Journal of Thermal Sciences*, **71** 32–35 (2013).

[42] S.F. Corbin and D.M. Turriff, "Thermal Diffusivity by The Laser Flash Technique;" pp. 1–10 in *Characterization of Materials*. American Cancer Society, 2012.

[43] L.E. Bell, "Cooling, heating, generating power, and recovering waste heat with thermoelectric systems," *Science*, **321** [5895] 1457–1461 (2008).

[44] K. Biswas, J. He, I.D. Blum, C.-I. Wu, T.P. Hogan, D.N. Seidman, V.P. Dravid, and M.G. Kanatzidis, "High-performance bulk thermoelectrics with all-scale hierarchical architectures," *Nature*, **489** [7416] 414–418 (2012).

[45] T.C. Harman, P.J. Taylor, M.P. Walsh, and B.E. LaForge, "Quantum dot superlattice thermoelectric materials and devices," *Science*, **297** [5590] 2229–2232 (2002).

[46] S.J. Zinkle, K.A. Terrani, J.C. Gehin, L.J. Ott, and L.L. Snead, "Accident tolerant fuels for LWRs: A perspective," *Journal of Nuclear Materials*, **448** [1–3] 374–379 (2014).

[47] W. Zhou and W. Zhou, "Enhanced thermal conductivity accident tolerant fuels for improved reactor safety – A comprehensive review," *Annals of Nuclear Energy*, **119** 66–86 (2018).

[48] S.L. Hayes, J.K. Thomas, and K.L. Peddicord, "Material property correlations for uranium mononitride: IV. Thermodynamic Properties," *Journal of Nuclear Materials*, **171** [2] 300–318 (1990).

[49] J.T. White, A.T. Nelson, J.T. Dunwoody, D.D. Byler, D.J. Safarik, and K.J. McClellan, "Thermophysical properties of U3Si2 to 1773 K," *Journal of Nuclear Materials*, **464** 275–280 (2015).

[50] E.S. Wood, J.T. White, C.J. Grote, and A.T. Nelson, "U3Si2 behavior in H2O: Part I, flowing steam and the effect of hydrogen," *Journal of Nuclear Materials*, **501** 404–412 (2018).

[51] A.T. Nelson, A. Migdisov, E.S. Wood, and C.J. Grote, "U3Si2 behavior in H2O environments: Part II, pressurized water with controlled redox chemistry," *Journal of Nuclear Materials*, **500** 81–91 (2018).

[52] P.G. Lucuta, H. Matzke, and I.J. Hastings, "A pragmatic approach to modelling thermal conductivity of irradiated UO2 fuel: Review and recommendations," *Journal of Nuclear Materials*, **232** [2–3] 166–180 (1996).

[53] P.G. Lucuta, H. Matzke, and R.A. Verrall, “Modelling of UO2-based SIMFUEL thermal conductivity The effect of the burnup,” *Journal of Nuclear Materials*, **217** [3] 279–286 (1994).

[54] P.G. Lucuta, H. Matzke, and R.A. Verrall, “Thermal conductivity of hyperstoichiometric SIMFUEL,” *Journal of Nuclear Materials*, **223** [1] 51–60 (1995).

[55] D.R. Gaston, C.J. Permann, J.W. Peterson, A.E. Slaughter, D. Andrš, Y. Wang, M.P. Short, D.M. Perez, *et al.*, “Physics-based multiscale coupling for full core nuclear reactor simulation,” *Annals of Nuclear Energy*, **84** 45–54 (2015).

[56] C.B. Carter and M.G. Norton, *Ceramic Materials: Science and Engineering*. Springer Science & Business Media, 2013.

[57] K.S.S. Harsha, "Principles of Physical Vapor Deposition of Thin Films", Elsevier, Great Britain (2006), p. 400.

[58] M.R. Tonks, X.-Y. Liu, D. Andersson, D. Perez, A. Chernatynskiy, G. Pastore, C.R. Stanek, and R. Williamson, “Development of a multiscale thermal conductivity model for fission gas in UO2,” *Journal of Nuclear Materials*, **469** 89–98 (2016).

[59] C. Degueldre and J.M. Paratte, “Concepts for an inert matrix fuel, an overview,” *Journal of Nuclear Materials*, **274** [1] 1–6 (1999).

[60] J.A. Valdez, I.O. Usov, J. Won, M. Tang, R.M. Dickerson, G.D. Jarvinen, and K.E. Sickafus, “10MeV Au ion irradiation effects in an MgO–HfO2 ceramic–ceramic (CERCER) composite,” *Journal of Nuclear Materials*, **393** [1] 126–133 (2009).

[61] I.O. Usov, J.A. Valdez, J. Won, M. Hawley, D.J. Devlin, R.M. Dickerson, B.P. Uberuaga, Y.Q. Wang, *et al.*, “Irradiation effects in an HfO2/MgO/HfO2 tri-layer structure induced by 10MeV Au ions,” *Nuclear Instruments and Methods in Physics Research Section B: Beam Interactions with Materials and Atoms*, **267** [11] 1918–1923 (2009).

[62] A.T. Nelson, M.M. Giachino, J.C. Nino, and K.J. McClellan, “Effect of composition on thermal conductivity of MgO–$Nd_2Zr_2O_7$ composites for inert matrix materials,” *Journal of Nuclear Materials*, **444** [1–3] 385–392 (2014).

[63] N. Nitani, T. Yamashita, T. Matsuda, S. Kobayashi, and T. Ohmichi, “Thermophysical properties of rock-like oxide fuel with spinel–yttria stabilized zirconia system,” *Journal of Nuclear Materials*, **274** [1–2] 15–22 (1999).

[64] J.K. Fink, “Thermophysical properties of uranium dioxide.” *J Nucl Mat*, **279** [1] 1–18 (2000).

[65] K.W. Schlichting, N.P. Padture, and P.G. Klemens, “Thermal conductivity of dense and porous yttria-stabilized zirconia,” *Journal of Materials Science*, **36** [12] 3003–3010 (2001).

[66] M. Munro, "Evaluated Material Properties for a Sintered alpha-Alumina," *Journal of the American Ceramic Society*, **80** [8] 1919–1928 (1997).

[67] K.R. Wilkerson, J.D. Smith, T.P. Sander, and J.G. Hemrick, "Solid Solution Effects on the Thermal Properties in the $MgAl_2O_4$–$MgGa_2O_4$ System," *J. Am. Ceram. Soc.*, **96** [3] 859–866 (2013).

[68] A.T. Nelson, D.R. Rittman, J.T. White, J.T. Dunwoody, M. Kato, and K.J. McClellan, "An Evaluation of the Thermophysical Properties of Stoichiometric CeO2 in Comparison to UO2 and PuO2," *J. Am. Ceram. Soc.*, **97** [11] 3652–3659 (2014).

[69] A.C.E. Reid, R.C. Lua, R.E. Garcia, V.R. Coffman, and S.A. Langer, "Modelling Microstructures with OOF2," *Int. J. Mater. Prod. Technol.*, **35** [3–4] 361–373 (2009).

[70] M.R. Tonks, D. Gaston, P.C. Millett, D. Andrs, and P. Talbot, "An object-oriented finite element framework for multiphysics phase field simulations," *Computational Materials Science*, **51** [1] 20–29 (2012).

[71] M.C. Teague, B.S. Fromm, M.R. Tonks, and D.P. Field, "Using Coupled Mesoscale Experiments and Simulations to Investigate High Burn-Up Oxide Fuel Thermal Conductivity," *JOM*, **66** [12] 2569–2577 (2014).

[72] J.P. Angle, Z. Wang, C. Dames, and M.L. Mecartney, "Comparison of Two-Phase Thermal Conductivity Models with Experiments on Dilute Ceramic Composites," *J. Am. Ceram. Soc.*, **96** [9] 2935–2942 (2013).

[73] T. Hori, J. Shiomi, and C. Dames, "Effective phonon mean free path in polycrystalline nanostructures," *Appl. Phys. Lett.*, **106** [17] 171901 (2015).

[74] D. Kok, S.K. Jha, R. Raj, and M.L. Mecartney, "Flash sintering of a three-phase alumina, spinel, and yttria-stabilized zirconia composite," *Journal of the American Ceramic Society*, **100** [7] 3262–3268 (2017).

[75] Standard test method for thermal diffusivity by the flash method, ASTM International, West Conshohocken, PA, E1461-13, 2013.

[76] D.A.G. Bruggeman, "Calculation of various physics constants in heterogenous substances I Dielectricity constants and conductivity of mixed bodies from isotropic substances," *Ann. Phys.-Berlin*, **24** [7] 636–664 (1935).

[77] E.T. Swartz and R.O. Pohl, "Thermal boundary resistance," *Rev. Mod. Phys.*, **61** [3] 605–668 (1989).

[78] D.S. Smith, S. Fayette, S. Grandjean, C. Martin, R. Telle, and T. Tonnessen, "Thermal Resistance of Grain Boundaries in Alumina Ceramics and Refractories," *Journal of the American Ceramic Society*, **86** [1] 105–111 (2003).

[79] F. Yang, X. Zhao, and P. Xiao, "Thermal conductivities of YSZ/Al_2O_3 composites," *Journal of the European Ceramic Society*, **30** [15] 3111–3116 (2010).

[80] C.W. Nan and R. Birringer, "Determining the Kapitza resistance and the thermal conductivity of polycrystals: A simple model," *Phys. Rev. B*, **57** [14] 8264–8268 (1998).

[81] Y. Lei, Y. Ito, N.D. Browning, and T.J. Mazanec, "Segregation Effects at Grain Boundaries in Fluorite-Structured Ceramics," *Journal of the American Ceramic Society*, **85** [9] 2359–2363 (2002).

[82] A. Chernatynskiy, X.-M. Bai, and J. Gan, "Systematic investigation of the misorientation- and temperature-dependent Kapitza resistance in CeO2," *International Journal of Heat and Mass Transfer*, **99** 461–469 (2016).

[83] L. Braginsky, N. Lukzen, V. Shklover, and H. Hofmann, "High-temperature phonon thermal conductivity of nanostructures," *Phys. Rev. B*, **66** [13] 134203 (2002).

[84] A.E. Gheribi and P. Chartrand, "Effect of Grain Boundaries on the Lattice Thermal Transport Properties of Insulating Materials: A Predictive Model," *J. Am. Ceram. Soc.*, **98** [3] 888–897 (2015).

[85] J.T. White and A.T. Nelson, "Thermal conductivity of UO2+x and U4O9−y," *Journal of Nuclear Materials*, **443** [1–3] 342–350 (2013).

[86] W.J. Parker, R.J. Jenkins, C.P. Butler, and G.L. Abbott, "Flash Method of Determining Thermal Diffusivity, Heat Capacity, and Thermal Conductivity," *Journal of Applied Physics*, **32** [9] 1679–1684 (1961).

[87] D.G. Cahill, "Thermal conductivity measurement from 30 to 750 K: the 3ω method," *Review of Scientific Instruments*, **61** [2] 802–808 (1990).

[88] L. Lu, W. Yi, and D.L. Zhang, "3ω method for specific heat and thermal conductivity measurements," *Review of Scientific Instruments*, **72** [7] 2996–3003 (2001).

[89] C. Dames and G. Chen, "1ω, 2ω, and 3ω methods for measurements of thermal properties," *Review of Scientific Instruments*, **76** [12] 124902 (2005).

[90] M. Sheindlin, D. Halton, M. Musella, and C. Ronchi, "Advances in the use of laser-flash techniques for thermal diffusivity measurement," *Review of Scientific Instruments*, **69** [3] 1426–1436 (1998).

[91] C. Dames *et al*., "3 Omega Manual," Spetember 4 2015.

[92] H. Hayashi, T. Saitou, N. Maruyama, H. Inaba, K. Kawamura, and M. Mori, "Thermal expansion coefficient of yttria stabilized zirconia for various yttria contents," *Solid State Ionics*, **176** [5–6] 613–619 (2005).

[93] R. Vassen, X. Cao, F. Tietz, D. Basu, and D. Stöver, "Zirconates as New Materials for Thermal Barrier Coatings," *Journal of the American Ceramic Society*, **83** [8] 2023–2028 (2000).

[94] C. Dames "Measuring the thermal conductivity of thin films: 3 omega and related electrothermal methods," *Annual Review of Heat Transfer*, 2013.

[95] L. Shi, C. Dames, J.R. Lukes, P. Reddy, J. Duda, D.G. Cahill, J. Lee, A. Marconnet, *et al.*, "Evaluating Broader Impacts of Nanoscale Thermal Transport Research," *Nanoscale and Microscale Thermophysical Engineering*, **19** [2] 127–165 (2015).

[96] H.-G. Kim, J.-H. Yang, W.-J. Kim, and Y.-H. Koo, "Development Status of Accident-tolerant Fuel for Light Water Reactors in Korea," *Nucl. Eng. Technol.*, **48** [1] 1–15 (2016).

[97] B.A. Pint, K.A. Terrani, Y. Yamamoto, and L.L. Snead, "Material Selection for Accident Tolerant Fuel Cladding," *Metall. Mater. Trans. E-Mater. Energy Syst.*, **2** [3] 190–196 (2015).

[98] L.J. Ott, K.R. Robb, and D. Wang, "Preliminary assessment of accident-tolerant fuels on LWR performance during normal operation and under DB and BDB accident conditions," *J. Nucl. Mater.*, **448** [1–3] 520–533 (2014).

[99] Y.-H. Koo, Y.-S. Yang, and K.-W. Song, "Radioactivity release from the Fukushima accident and its consequences: A review," *Prog. Nucl. Energy*, **74** 61–70 (2014).

[100] M. Ben-Belgacem, V. Richet, K.A. Terrani, Y. Katoh, and L.L. Snead, "Thermo-mechanical analysis of LWR SiC/SiC composite cladding," *J. Nucl. Mater.*, **447** [1–3] 125–142 (2014).

[101] T. Cheng, J.R. Keiser, M.P. Brady, K.A. Terrani, and B.A. Pint, "Oxidation of fuel cladding candidate materials in steam environments at high temperature and pressure," *J. Nucl. Mater.*, **427** [1–3] 396–400 (2012).

[102] B.A. Pint, K.A. Terrani, M.P. Brady, T. Cheng, and J.R. Keiser, "High temperature oxidation of fuel cladding candidate materials in steam-hydrogen environments," *J. Nucl. Mater.*, **440** [1–3] 420–427 (2013).

[103] P.G. Medvedev, S.M. Frank, T.P. O'Holleran, and M.K. Meyer, "Dual phase MgO–ZrO2 ceramics for use in LWR inert matrix fuel," *Journal of Nuclear Materials*, **342** [1] 48–62 (2005).

[104] N.R. Brown, A. Aronson, M. Todosow, R. Brito, and K.J. McClellan, "Neutronic performance of uranium nitride composite fuels in a PWR," *Nuclear Engineering and Design*, **275** 393–407 (2014).

[105] N.R. Brown, A. Aronson, M. Todosow, R. Brito, and K.J. McClellan, "Neutronic performance of uranium nitride composite fuels in a PWR," *Nuclear Engineering and Design*, **275** 393–407 (2014).

[106] J.T. White, A.T. Nelson, D.D. Byler, J.A. Valdez, and K.J. McClellan, "Thermophysical properties of U3Si to 1150 K," *Journal of Nuclear Materials*, **452** [1–3] 304–310 (2014).

[107] J.T. White, A.T. Nelson, D.D. Byler, D.J. Safarik, J.T. Dunwoody, and K.J. McClellan, "Thermophysical properties of U3Si5 to 1773 K," *Journal of Nuclear Materials*, **456** 442–448 (2015).

[108] J.T. White, A.T. Nelson, J.T. Dunwoody, D.D. Byler, and K.J. McClellan, "Thermophysical properties of USi to 1673 K," *Journal of Nuclear Materials*, **471** 129–135 (2016).

[109] A.T. Nelson, J.T. White, D.D. Byler, J.T. Dunwoody, J.A. Valdez, and K.J. McClellan, "Overview of properties and performance of uranium-silicide compounds for light water reactor applications," Transactions of the American Nuclear Society, Volume 110, 2014, Pages 987-989.

[110] J.M. Harp, P.A. Lessing, and R.E. Hoggan, "Uranium silicide pellet fabrication by powder metallurgy for accident tolerant fuel evaluation and irradiation," *Journal of Nuclear Materials*, **466** 728–738 (2015).

[111] M. Teague, M. Tonks, S. Novascone, and S. Hayes, "Microstructural modeling of thermal conductivity of high burn-up mixed oxide fuel," *Journal of Nuclear Materials*, **444** [1–3] 161–169 (2014).

[112] P.C. Millett, D. Wolf, T. Desai, S. Rokkam, and A. El-Azab, "Phase-field simulation of thermal conductivity in porous polycrystalline microstructures," *Journal of Applied Physics*, **104** [3] 033512 (2008).

[113] J. Leitner, P. Voňka, D. Sedmidubský, and P. Svoboda, "Application of Neumann–Kopp rule for the estimation of heat capacity of mixed oxides," *Thermochimica Acta*, **497** [1] 7–13 (2010).

[114] I.A. Deryabin, V.S. Kharitonov, and D.Y. Lyubimov, "Effect of Fission Products and Oxygen and Carbon Impurities in (U, Pu)N on the Heat-and-Mass Transfer Coefficients and Xenon Yield," *At Energy*, **121** [2] 96–105 (2016).

[115] S.L. Hayes, J.K. Thomas, and K.L. Peddicord, "Material property correlations for uranium mononitride: III. Transport properties," *Journal of Nuclear Materials*, **171** [2] 289–299 (1990).

[116] M. Uchida, E. Ishitsuka, and H. Kawamura, "Thermal conductivity of neutron irradiated Be12Ti," *Fusion Engineering and Design*, **69** [1] 499–503 (2003).

[117] R.C. Birtcher, J.W. Richardson, and M.H. Mueller, "Amorphization of U3Si2 by ion or neutron irradiation," *Journal of Nuclear Materials*, **230** [2] 158–163 (1996).

[118] Y. Miao, J. Harp, K. Mo, S. Bhattacharya, P. Baldo, and A.M. Yacout, "Short Communication on 'In-situ TEM ion irradiation investigations on U3Si2 at LWR temperatures,'" *Journal of Nuclear Materials*, **484** 168–173 (2017).

[119] I. Hore-Lacy, "Nuclear Energy in the 21st Century," p. The World Nuclear University Primer: United Kingdom, (2012).

[120] J.D. Higgs, W.T. Thompson, B.J. Lewis, and S.C. Vogel, "Kinetics of precipitation of U4O9 from hyperstoichiometric UO2+x," *Journal of Nuclear Materials*, **366** [3] 297–305 (2007).

[121] T. Watanabe, S.G. Srivilliputhur, P.K. Schelling, J.S. Tulenko, S.B. Sinnott, and S.R. Phillpot, "Thermal Transport in Off-Stoichiometric Uranium Dioxide by Atomic Level Simulation," *Journal of the American Ceramic Society*, **92** [4] 850–856 (2009).

[122] D. Labroche, O. Dugne, and C. Chatillon, "Thermodynamic properties of the O–U system. II – Critical assessment of the stability and composition range of the oxides UO2+x, U4O9−y and U3O8−z," *Journal of Nuclear Materials*, **312** [1] 50–66 (2003).

[123] N. Moelans, B. Blanpain, and P. Wollants, "An introduction to phase-field modeling of microstructure evolution," *Calphad*, **32** [2] 268–294 (2008).

[124] L.-Q. Chen, "Phase-Field Models for Microstructure Evolution," *Annu. Rev. Mater. Res.*, **32** [1] 113–140 (2002).

[125] A.M. Jokisaari and K. Thornton, "General method for incorporating CALPHAD free energies of mixing into phase field models: Application to the α-zirconium/δ-hydride system," *Calphad*, **51** 334–343 (2015).

[126] W. Van Lierde, J. Pelsmaekers, and A. Lecocq-Robert, "On the phase limits of U4O9," *Journal of Nuclear Materials*, **37** [3] 276–285 (1970).

[127] J.H. Davies, E.V. Hoshi, and D.L. Zimmerman, "Ramp test behavior of high O/U fuel," *Journal of Nuclear Materials*, **270** [1–2] 87–95 (1999).

[128] I. Loginova, J. Ågren, and G. Amberg, "On the formation of Widmanstätten ferrite in binary Fe–C – phase-field approach," *Acta Materialia*, **52** [13] 4055–4063 (2004).

[129] R. Kobayashi, "Modeling and numerical simulations of dendritic crystal growth," *Physica D: Nonlinear Phenomena*, **63** [3] 410–423 (1993).

[130] Y. Noda and K. Naito, "The thermal conductivity and diffusivity of U4O9−y from 250 to 415 K," *Journal of Nuclear Materials*, **66** [1] 17–22 (1977).

[131] U. Ayachit, *The ParaView Guide: A Parallel Visualization Application*. Kitware, Inc., USA, 2015.

Appendices

Appendix A: Sample MOOSE Script

Sample MOOSE script for determining the temperature dependent thermal conductivity of a ternary phase composite at 298K.

```
[Mesh]
  # uniform_refine = 4
  type = FileMesh
  file = large_three_phase_1-mesh.inp
  construct_side_list_from_node_list = true
[]

[MeshModifiers] #Adds a new node set
  [./new_nodeset]
    type = AddExtraNodeset
    nodes = '0'
    new_boundary = 100
  [../]
[]

[Variables]
  [./T]
    initial_condition = 298
  [../]
  [./Tx_AEH] #Temperature used for the x-component of the AEH solve
    initial_condition = 298
    scaling = 1.0e4 #Scales residual to improve convergence
  [../]
  [./Ty_AEH] #Temperature used for the y-component of the AEH solve
    initial_condition = 298
    scaling = 1.0e4  #Scales residual to improve convergence
  [../]
[]

[Kernels]
  [./HtCond] #Kernel for direct calculation of thermal cond
    type = HeatConduction
    variable = T
  [../]
  [./heat_x] #All other kernels are for AEH approach to calculate thermal cond.
    type = HeatConduction
    variable = Tx_AEH
  [../]
  [./heat_rhs_x]
    type = HomogenizedHeatConduction
```

```
    variable = Tx_AEH
    component = 0
  [../]
  [./heat_y]
    type = HeatConduction
    variable = Ty_AEH
  [../]
  [./heat_rhs_y]
    type = HomogenizedHeatConduction
    variable = Ty_AEH
    component = 1
  [../]
[]

[BCs]
  [./left] #Fix temperature on the left side
    type = DirichletBC
    variable = T
    boundary = left
    value = 298
  [../]
  [./right_flux] #Set heat flux on the right side
    type = NeumannBC
    variable = T
    boundary = right
    value = 5e-8
  [../]
  [./Periodic]
    [./all]
      auto_direction = 'x y'
      variable = 'Tx_AEH Ty_AEH'
    [../]
  [../]
  [./fix_x] #Fix Tx_AEH at a single point
    type = DirichletBC
    variable = Tx_AEH
    value = 298
    boundary = 100
  [../]
  [./fix_y] #Fix Ty_AEH at a single point
    type = DirichletBC
    variable = Ty_AEH
    value = 298
    boundary = 100
  [../]
[]
```

```
[Materials]
  [./thcond] #The equation defining the thermal conductivity is defined here, using two ifs
    # The k in the bulk is k_b, in the precipitate k_p2, and across the interaface k_int
    type = ParsedMaterial
    block = 1
    constant_names = 'length_scale k_al2o3'
    constant_expressions = '1e-6 33.3830705'
    function = '(k_al2o3*length_scale)'
    outputs = exodus
    f_name = thermal_conductivity
  [../]
  [./thcond_2] #The equation defining the thermal conductivity is defined here, using two ifs
    # The k in the bulk is k_b, in the precipitate k_p2, and across the interaface k_int
    type = ParsedMaterial
    block = 0
    constant_names = 'length_scale k_mgal2o4'
    constant_expressions = '1e-6 17.8496205'
    function = '(k_mgal2o4*length_scale)'
    outputs = exodus
    f_name = thermal_conductivity
  [../]
  [./thcond_3] #The equation defining the thermal conductivity is defined here, using two ifs
    # The k in the bulk is k_b, in the precipitate k_p2, and across the interaface k_int
    type = ParsedMaterial
    block = 2
    constant_names = 'length_scale k_ysz'
    constant_expressions = '1e-6 1.75'
    function = '(k_ysz*length_scale)'
    outputs = exodus
    f_name = thermal_conductivity
  [../]
[]

  [Postprocessors]
    [./right_T]
      type = SideAverageValue
      variable = T
      boundary = right
    [../]
    [./k_x_direct] #Effective thermal conductivity from direct method
      # This value is lower than the AEH value because it is impacted by second phase
      # on the right boundary
      type = ThermalConductivity
      variable = T
      flux = 5e-8
```

```
    length_scale = 1e-6
    T_hot = 298
    dx = 2266
    boundary = right
  [../]
  [./k_x_AEH] #Effective thermal conductivity in x-direction from AEH
    type = HomogenizedThermalConductivity
    variable = Tx_AEH
    temp_x = Tx_AEH
    temp_y = Ty_AEH
    component = 0
    scale_factor = 1e6 #Scale due to length scale of problem
  [../]
  [./k_y_AEH] #Effective thermal conductivity in x-direction from AEH
    type = HomogenizedThermalConductivity
    variable = Ty_AEH
    temp_x = Tx_AEH
    temp_y = Ty_AEH
    component = 1
    scale_factor = 1e6 #Scale due to length scale of problem
  [../]
 []

 [Preconditioning]
  [./SMP]
    type = SMP
    off_diag_row = 'Tx_AEH Ty_AEH'
    off_diag_column = 'Ty_AEH Tx_AEH'
  [../]
 []

 [Executioner]
  type = Steady
  l_max_its = 20
  solve_type = NEWTON
  petsc_options_iname = '-pc_type -pc_hypre_type -ksp_gmres_restart -
pc_hypre_boomeramg_strong_threshold'
  petsc_options_value = 'hypre boomeramg 31 0.7'
  l_tol = 1e-10
 []

 [Outputs]
  execute_on = 'timestep_end'
  exodus = true
  csv = true
[]
```

Appendix B: Sample OOF2 Script

Sample OOF2 script for determining the temperature dependent thermal conductivity of a binary phase composite.

```
OOF.Microstructure.Create_From_ImageFile(filename='/Users/austinwtravis/Desktop/UN:U-Si/Images for OOF2/UN:U3Si5/30USi5UN_1um_blue_500x_5 copy.tif', microstructure_name='30USi5UN_1um_blue_500x_5 copy.tif', height=automatic, width=automatic)
OOF.PixelGroup.New(name='UN', microstructure='30USi5UN_1um_blue_500x_5 copy.tif')
OOF.PixelGroup.New(name='U3Si5', microstructure='30USi5UN_1um_blue_500x_5 copy.tif')
OOF.Windows.Graphics.New()
OOF.Graphics_1.Toolbox.Pixel_Select.Burn(source='30USi5UN_1um_blue_500x_5 copy.tif:30USi5UN_1um_blue_500x_5 copy.tif', local_flammability=0.1, global_flammability=0.2, color_space_norm='L1', next_nearest=False, points=[Point(311.372,1223.552)], shift=0, ctrl=0)
OOF.Graphics_1.Toolbox.Pixel_Select.Burn(source='30USi5UN_1um_blue_500x_5 copy.tif:30USi5UN_1um_blue_500x_5 copy.tif', local_flammability=0.1, global_flammability=0.2, color_space_norm='L1', next_nearest=False, points=[Point(1384.378,591.118)], shift=0, ctrl=0)
OOF.Graphics_1.Toolbox.Pixel_Select.Burn(source='30USi5UN_1um_blue_500x_5 copy.tif:30USi5UN_1um_blue_500x_5 copy.tif', local_flammability=0.1, global_flammability=0.2, color_space_norm='L1', next_nearest=False, points=[Point(538.764,861.146)], shift=1, ctrl=0)
OOF.Graphics_1.Toolbox.Pixel_Select.Burn(source='30USi5UN_1um_blue_500x_5 copy.tif:30USi5UN_1um_blue_500x_5 copy.tif', local_flammability=0.1, global_flammability=0.2, color_space_norm='L1', next_nearest=False, points=[Point(20.026,1720.972)], shift=1, ctrl=0)
OOF.Graphics_1.Toolbox.Pixel_Select.Burn(source='30USi5UN_1um_blue_500x_5 copy.tif:30USi5UN_1um_blue_500x_5 copy.tif', local_flammability=0.1, global_flammability=0.2, color_space_norm='L1', next_nearest=False, points=[Point(1192.516,26.191)], shift=1, ctrl=0)
OOF.Graphics_1.Toolbox.Pixel_Select.Burn(source='30USi5UN_1um_blue_500x_5 copy.tif:30USi5UN_1um_blue_500x_5 copy.tif', local_flammability=0.1, global_flammability=0.2, color_space_norm='L1', next_nearest=False, points=[Point(2425.407,264.242)], shift=1, ctrl=0)
OOF.Graphics_1.Toolbox.Pixel_Select.Burn(source='30USi5UN_1um_blue_500x_5 copy.tif:30USi5UN_1um_blue_500x_5 copy.tif', local_flammability=0.1, global_flammability=0.2, color_space_norm='L1', next_nearest=False, points=[Point(2563.974,317.537)], shift=1, ctrl=0)
OOF.Graphics_1.Toolbox.Pixel_Select.Burn(source='30USi5UN_1um_blue_500x_5 copy.tif:30USi5UN_1um_blue_500x_5 copy.tif', local_flammability=0.1, global_flammability=0.2, color_space_norm='L1', next_nearest=False, points=[Point(2563.974,26.191)], shift=1, ctrl=0)
OOF.PixelGroup.AddSelection(microstructure='30USi5UN_1um_blue_500x_5 copy.tif', group='UN')
```

```
OOF.Graphics_1.Toolbox.Pixel_Select.Invert(source='30USi5UN_1um_blue_500x_5
copy.tif:30USi5UN_1um_blue_500x_5 copy.tif')
OOF.PixelGroup.AddSelection(microstructure='30USi5UN_1um_blue_500x_5 copy.tif',
group='U3Si5')
OOF.Material.New(name='UN', material_type='bulk')
OOF.Material.New(name='U3Si5', material_type='bulk')
OOF.Property.Copy(property='Thermal:Conductivity:Isotropic', new_name='UN_Thermal')
OOF.Property.Copy(property='Thermal:Conductivity:Isotropic:UN_Thermal',
new_name='U3Si5_Thermal')
OOF.Material.Add_property(name='U3Si5',
property='Thermal:Conductivity:Isotropic:U3Si5_Thermal')
OOF.Material.Assign(material='U3Si5', microstructure='30USi5UN_1um_blue_500x_5
copy.tif', pixels='U3Si5')
OOF.Material.Add_property(name='UN',
property='Thermal:Conductivity:Isotropic:UN_Thermal')
OOF.Material.Assign(material='UN', microstructure='30USi5UN_1um_blue_500x_5 copy.tif',
pixels='UN')
OOF.Skeleton.New(name='skeleton', microstructure='30USi5UN_1um_blue_500x_5 copy.tif',
x_elements=40, y_elements=30,
skeleton_geometry=QuadSkeleton(left_right_periodicity=False,top_bottom_periodicity=False))
OOF.Skeleton.Modify(skeleton='30USi5UN_1um_blue_500x_5 copy.tif:skeleton',
modifier=Refine(targets=CheckHomogeneity(threshold=0.969999999),criterion=Unconditionall
y(),degree=Trisection(rule_set='conservative'),alpha=0.5))
OOF.Skeleton.Modify(skeleton='30USi5UN_1um_blue_500x_5 copy.tif:skeleton',
modifier=Refine(targets=CheckHomogeneity(threshold=0.93000000001),criterion=Uncondition
ally(),degree=Trisection(rule_set='conservative'),alpha=0.5))
OOF.Skeleton.Modify(skeleton='30USi5UN_1um_blue_500x_5 copy.tif:skeleton',
modifier=Refine(targets=CheckHomogeneity(threshold=0.90000001),criterion=Unconditionally(
),degree=Trisection(rule_set='conservative'),alpha=0.5))
OOF.Skeleton.Modify(skeleton='30USi5UN_1um_blue_500x_5 copy.tif:skeleton',
modifier=SnapNodes(targets=SnapHeterogenous(threshold=0.9000000001),criterion=AverageE
nergy(alpha=1.0)))
OOF.Skeleton.Modify(skeleton='30USi5UN_1um_blue_500x_5 copy.tif:skeleton',
modifier=SnapNodes(targets=SnapHeterogenous(threshold=0.9000000001),criterion=AverageE
nergy(alpha=1.0)))
OOF.Graphics_1.File.Close()
OOF.Skeleton.Modify(skeleton='30USi5UN_1um_blue_500x_5 copy.tif:skeleton',
modifier=Rationalize(targets=AllElements(),criterion=AverageEnergy(alpha=0.9000001),metho
d=AutomaticRationalization()))
OOF.ElementSelection.Select_by_Homogeneity(skeleton='30USi5UN_1um_blue_500x_5
copy.tif:skeleton', threshold=0.9000001)
OOF.Skeleton.Modify(skeleton='30USi5UN_1um_blue_500x_5 copy.tif:skeleton',
modifier=Anneal(targets=FiddleSelectedElements(),criterion=AverageEnergy(alpha=0.9000001)
,T=0.0,delta=1.0,iteration=ConditionalIteration(condition=AcceptanceRate(acceptance_rate=5),e
xtra=15,maximum=50)))
```

```
OOF.Skeleton.Modify(skeleton='30USi5UN_1um_blue_500x_5 copy.tif:skeleton',
modifier=Rationalize(targets=AllElements(),criterion=AverageEnergy(alpha=0.9000001),metho
d=AutomaticRationalization()))
OOF.ElementSelection.Clear(skeleton='30USi5UN_1um_blue_500x_5 copy.tif:skeleton')
OOF.Skeleton.PinNodes.Pin_Internal_Boundary_Nodes(skeleton='30USi5UN_1um_blue_500x_
5 copy.tif:skeleton')
OOF.Skeleton.Modify(skeleton='30USi5UN_1um_blue_500x_5 copy.tif:skeleton',
modifier=Rationalize(targets=AllElements(),criterion=AverageEnergy(alpha=0.8000001),metho
d=AutomaticRationalization()))
OOF.Skeleton.Modify(skeleton='30USi5UN_1um_blue_500x_5 copy.tif:skeleton',
modifier=MergeTriangles(targets=AllElements(),criterion=LimitedUnconditional(alpha=0.5,ho
mogeneity=0.9,shape_energy=0.5)))
OOF.Skeleton.Modify(skeleton='30USi5UN_1um_blue_500x_5 copy.tif:skeleton',
modifier=Smooth(targets=AllNodes(),criterion=AverageEnergy(alpha=0.5999996),T=0.0,iterati
on=ConditionalIteration(condition=AcceptanceRate(acceptance_rate=30),extra=15,maximum=3
0)))
OOF.Skeleton.PinNodes.UnpinAll(skeleton='30USi5UN_1um_blue_500x_5 copy.tif:skeleton')
OOF.Mesh.New(name='mesh', skeleton='30USi5UN_1um_blue_500x_5 copy.tif:skeleton',
element_types=['D2_2', 'T3_3', 'Q4_4'])
OOF.Subproblem.Field.Define(subproblem='30USi5UN_1um_blue_500x_5
copy.tif:skeleton:mesh:default', field=Temperature)
OOF.Subproblem.Field.Activate(subproblem='30USi5UN_1um_blue_500x_5
copy.tif:skeleton:mesh:default', field=Temperature)
OOF.Subproblem.Equation.Activate(subproblem='30USi5UN_1um_blue_500x_5
copy.tif:skeleton:mesh:default', equation=Heat_Eqn)
OOF.Subproblem.Equation.Activate(subproblem='30USi5UN_1um_blue_500x_5
copy.tif:skeleton:mesh:default', equation=Plane_Heat_Flux)
OOF.Mesh.Boundary_Conditions.New(name='bc', mesh='30USi5UN_1um_blue_500x_5
copy.tif:skeleton:mesh',
condition=DirichletBC(field=Temperature,field_component='',equation=Heat_Eqn,eqn_compon
ent='',profile=ConstantProfile(value=370.0),boundary='top'))
OOF.Mesh.Boundary_Conditions.New(name='bc<2>', mesh='30USi5UN_1um_blue_500x_5
copy.tif:skeleton:mesh',
condition=DirichletBC(field=Temperature,field_component='',equation=Heat_Eqn,eqn_compon
ent='',profile=ConstantProfile(value=380.0),boundary='bottom'))
OOF.Mesh.Boundary_Conditions.New(name='bc<3>', mesh='30USi5UN_1um_blue_500x_5
copy.tif:skeleton:mesh',
condition=NeumannBC(flux=Heat_Flux,profile=ConstantProfile(value=0.0),boundary='right',no
rmal=False))
OOF.Mesh.Boundary_Conditions.New(name='bc<4>', mesh='30USi5UN_1um_blue_500x_5
copy.tif:skeleton:mesh',
condition=NeumannBC(flux=Heat_Flux,profile=ConstantProfile(value=0.0),boundary='left',nor
mal=False))
OOF.Property.Parametrize.Thermal.Conductivity.Isotropic.UN_Thermal(kappa=15.7631)
OOF.Material.Assign(material='UN', microstructure='30USi5UN_1um_blue_500x_5 copy.tif',
pixels='UN')
```

OOF.Property.Parametrize.Thermal.Conductivity.Isotropic.U3Si5_Thermal(kappa=5.2051)
OOF.Material.Assign(material='U3Si5', microstructure='30USi5UN_1um_blue_500x_5
copy.tif', pixels='U3Si5')
OOF.Subproblem.Set_Solver(subproblem='30USi5UN_1um_blue_500x_5
copy.tif:skeleton:mesh:default',
solver_mode=BasicSolverMode(time_stepper=BasicStaticDriver(),matrix_method=BasicIterativ
e(tolerance=1e-10,max_iterations=100000)))
OOF.Mesh.Solve(mesh='30USi5UN_1um_blue_500x_5 copy.tif:skeleton:mesh', endtime=0.0)
OOF.Mesh.Analyze.Integral(mesh='30USi5UN_1um_blue_500x_5 copy.tif:skeleton:mesh',
time=latest, data=getOutput('Flux:Invariant',invariant=Magnitude(),flux=Heat_Flux),
domain=SkeletonEdgeBoundaryDomain(boundary='top',side='LEFT'),
sampling=StatElementSegmentSampleSet(n_points=25), destination=MessageWindowStream())
OOF.Subproblem.Remove_Solver(subproblem='30USi5UN_1um_blue_500x_5
copy.tif:skeleton:mesh:default')
OOF.Mesh.Boundary_Conditions.Edit(name='bc', mesh='30USi5UN_1um_blue_500x_5
copy.tif:skeleton:mesh',
condition=DirichletBC(field=Temperature,field_component='',equation=Heat_Eqn,eqn_compon
ent='',profile=ConstantProfile(value=470.0),boundary='top'))
OOF.Mesh.Boundary_Conditions.Edit(name='bc<2>', mesh='30USi5UN_1um_blue_500x_5
copy.tif:skeleton:mesh',
condition=DirichletBC(field=Temperature,field_component='',equation=Heat_Eqn,eqn_compon
ent='',profile=ConstantProfile(value=480.0),boundary='bottom'))
OOF.Property.Parametrize.Thermal.Conductivity.Isotropic.U3Si5_Thermal(kappa=5.5341)
OOF.Material.Assign(material='U3Si5', microstructure='30USi5UN_1um_blue_500x_5
copy.tif', pixels='U3Si5')
OOF.Property.Parametrize.Thermal.Conductivity.Isotropic.UN_Thermal(kappa=17.0524)
OOF.Material.Assign(material='UN', microstructure='30USi5UN_1um_blue_500x_5 copy.tif',
pixels='UN')
OOF.Subproblem.Set_Solver(subproblem='30USi5UN_1um_blue_500x_5
copy.tif:skeleton:mesh:default',
solver_mode=BasicSolverMode(time_stepper=BasicStaticDriver(),matrix_method=BasicIterativ
e(tolerance=1e-10,max_iterations=100000)))
OOF.Mesh.Solve(mesh='30USi5UN_1um_blue_500x_5 copy.tif:skeleton:mesh', endtime=0.0)
OOF.Mesh.Analyze.Integral(mesh='30USi5UN_1um_blue_500x_5 copy.tif:skeleton:mesh',
time=latest, data=getOutput('Flux:Invariant',invariant=Magnitude(),flux=Heat_Flux),
domain=SkeletonEdgeBoundaryDomain(boundary='top',side='LEFT'),
sampling=StatElementSegmentSampleSet(n_points=25), destination=MessageWindowStream())
OOF.Subproblem.Remove_Solver(subproblem='30USi5UN_1um_blue_500x_5
copy.tif:skeleton:mesh:default')
OOF.Mesh.Boundary_Conditions.Edit(name='bc', mesh='30USi5UN_1um_blue_500x_5
copy.tif:skeleton:mesh',
condition=DirichletBC(field=Temperature,field_component='',equation=Heat_Eqn,eqn_compon
ent='',profile=ConstantProfile(value=570.0),boundary='top'))
OOF.Mesh.Boundary_Conditions.Edit(name='bc<2>', mesh='30USi5UN_1um_blue_500x_5
copy.tif:skeleton:mesh',

condition=DirichletBC(field=Temperature,field_component='',equation=Heat_Eqn,eqn_compon
ent='',profile=ConstantProfile(value=580.0),boundary='bottom'))
OOF.Property.Parametrize.Thermal.Conductivity.Isotropic.UN_Thermal(kappa=18.2679)
OOF.Material.Assign(material='UN', microstructure='30USi5UN_1um_blue_500x_5 copy.tif',
pixels='UN')
OOF.Property.Parametrize.Thermal.Conductivity.Isotropic.U3Si5_Thermal(kappa=5.8631)
OOF.Material.Assign(material='U3Si5', microstructure='30USi5UN_1um_blue_500x_5
copy.tif', pixels='U3Si5')
OOF.Subproblem.Set_Solver(subproblem='30USi5UN_1um_blue_500x_5
copy.tif:skeleton:mesh:default',
solver_mode=BasicSolverMode(time_stepper=BasicStaticDriver(),matrix_method=BasicIterativ
e(tolerance=1e-10,max_iterations=100000)))
OOF.Mesh.Solve(mesh='30USi5UN_1um_blue_500x_5 copy.tif:skeleton:mesh', endtime=0.0)
OOF.Mesh.Analyze.Integral(mesh='30USi5UN_1um_blue_500x_5 copy.tif:skeleton:mesh',
time=latest, data=getOutput('Flux:Invariant',invariant=Magnitude(),flux=Heat_Flux),
domain=SkeletonEdgeBoundaryDomain(boundary='top',side='LEFT'),
sampling=StatElementSegmentSampleSet(n_points=25), destination=MessageWindowStream())
OOF.Subproblem.Remove_Solver(subproblem='30USi5UN_1um_blue_500x_5
copy.tif:skeleton:mesh:default')
OOF.Mesh.Boundary_Conditions.Edit(name='bc', mesh='30USi5UN_1um_blue_500x_5
copy.tif:skeleton:mesh',
condition=DirichletBC(field=Temperature,field_component='',equation=Heat_Eqn,eqn_compon
ent='',profile=ConstantProfile(value=670.0),boundary='top'))
OOF.Mesh.Boundary_Conditions.Edit(name='bc<2>', mesh='30USi5UN_1um_blue_500x_5
copy.tif:skeleton:mesh',
condition=DirichletBC(field=Temperature,field_component='',equation=Heat_Eqn,eqn_compon
ent='',profile=ConstantProfile(value=680.0),boundary='bottom'))
OOF.Property.Parametrize.Thermal.Conductivity.Isotropic.U3Si5_Thermal(kappa=6.1921)
OOF.Material.Assign(material='U3Si5', microstructure='30USi5UN_1um_blue_500x_5
copy.tif', pixels='U3Si5')
OOF.Property.Parametrize.Thermal.Conductivity.Isotropic.UN_Thermal(kappa=19.4096)
OOF.Material.Assign(material='UN', microstructure='30USi5UN_1um_blue_500x_5 copy.tif',
pixels='UN')
OOF.Subproblem.Set_Solver(subproblem='30USi5UN_1um_blue_500x_5
copy.tif:skeleton:mesh:default',
solver_mode=BasicSolverMode(time_stepper=BasicStaticDriver(),matrix_method=BasicIterativ
e(tolerance=1e-10,max_iterations=100000)))
OOF.Mesh.Solve(mesh='30USi5UN_1um_blue_500x_5 copy.tif:skeleton:mesh', endtime=0.0)
OOF.Mesh.Analyze.Integral(mesh='30USi5UN_1um_blue_500x_5 copy.tif:skeleton:mesh',
time=latest, data=getOutput('Flux:Invariant',invariant=Magnitude(),flux=Heat_Flux),
domain=SkeletonEdgeBoundaryDomain(boundary='top',side='LEFT'),
sampling=StatElementSegmentSampleSet(n_points=25), destination=MessageWindowStream())
OOF.Subproblem.Remove_Solver(subproblem='30USi5UN_1um_blue_500x_5
copy.tif:skeleton:mesh:default')
OOF.Mesh.Boundary_Conditions.Edit(name='bc', mesh='30USi5UN_1um_blue_500x_5
copy.tif:skeleton:mesh',

condition=DirichletBC(field=Temperature,field_component='',equation=Heat_Eqn,eqn_compon
ent='',profile=ConstantProfile(value=770.0),boundary='top'))
OOF.Mesh.Boundary_Conditions.Edit(name='bc<2>', mesh='30USi5UN_1um_blue_500x_5
copy.tif:skeleton:mesh',
condition=DirichletBC(field=Temperature,field_component='',equation=Heat_Eqn,eqn_compon
ent='',profile=ConstantProfile(value=780.0),boundary='bottom'))
OOF.Property.Parametrize.Thermal.Conductivity.Isotropic.UN_Thermal(kappa=20.4775)
OOF.Material.Assign(material='UN', microstructure='30USi5UN_1um_blue_500x_5 copy.tif',
pixels='UN')
OOF.Property.Parametrize.Thermal.Conductivity.Isotropic.U3Si5_Thermal(kappa=9.82008)
OOF.Material.Assign(material='U3Si5', microstructure='30USi5UN_1um_blue_500x_5
copy.tif', pixels='U3Si5')
OOF.Subproblem.Set_Solver(subproblem='30USi5UN_1um_blue_500x_5
copy.tif:skeleton:mesh:default',
solver_mode=BasicSolverMode(time_stepper=BasicStaticDriver(),matrix_method=BasicIterativ
e(tolerance=1e-10,max_iterations=100000)))
OOF.Mesh.Solve(mesh='30USi5UN_1um_blue_500x_5 copy.tif:skeleton:mesh', endtime=0.0)
OOF.Mesh.Analyze.Integral(mesh='30USi5UN_1um_blue_500x_5 copy.tif:skeleton:mesh',
time=latest, data=getOutput('Flux:Invariant',invariant=Magnitude(),flux=Heat_Flux),
domain=SkeletonEdgeBoundaryDomain(boundary='top',side='LEFT'),
sampling=StatElementSegmentSampleSet(n_points=25), destination=MessageWindowStream())
OOF.Subproblem.Remove_Solver(subproblem='30USi5UN_1um_blue_500x_5
copy.tif:skeleton:mesh:default')
OOF.Mesh.Boundary_Conditions.Edit(name='bc<2>', mesh='30USi5UN_1um_blue_500x_5
copy.tif:skeleton:mesh',
condition=DirichletBC(field=Temperature,field_component='',equation=Heat_Eqn,eqn_compon
ent='',profile=ConstantProfile(value=880.0),boundary='bottom'))
OOF.Mesh.Boundary_Conditions.Edit(name='bc', mesh='30USi5UN_1um_blue_500x_5
copy.tif:skeleton:mesh',
condition=DirichletBC(field=Temperature,field_component='',equation=Heat_Eqn,eqn_compon
ent='',profile=ConstantProfile(value=870.0),boundary='top'))
OOF.Property.Parametrize.Thermal.Conductivity.Isotropic.U3Si5_Thermal(kappa=10.71408)
OOF.Material.Assign(material='U3Si5', microstructure='30USi5UN_1um_blue_500x_5
copy.tif', pixels='U3Si5')
OOF.Property.Parametrize.Thermal.Conductivity.Isotropic.UN_Thermal(kappa=21.4716)
OOF.Material.Assign(material='UN', microstructure='30USi5UN_1um_blue_500x_5 copy.tif',
pixels='UN')
OOF.Subproblem.Set_Solver(subproblem='30USi5UN_1um_blue_500x_5
copy.tif:skeleton:mesh:default',
solver_mode=BasicSolverMode(time_stepper=BasicStaticDriver(),matrix_method=BasicIterativ
e(tolerance=1e-10,max_iterations=100000)))